

Gas/Surface reactions probed by reflection absorption infrared spectroscopy

Présentée le 24 mars 2023

Faculté des sciences de base
Laboratoire de chimie physique moléculaire
Programme doctoral en chimie et génie chimique

pour l'obtention du grade de Docteur ès Sciences

par

Harmina VEJAYAN

Acceptée sur proposition du jury

Prof. K. Sivula, président du jury
Prof. R. Beck, directeur de thèse
Prof. L. Juurlink, rapporteur
Prof. H. Guo, rapporteur
Dr A. Caracciolo, rapporteuse

Abstract

In my thesis, I present an investigation of the dissociation reactions of gas phase molecules on single crystal metal surfaces studied by a molecular beam in combination with Reflection Absorption Infrared Spectroscopy (RAIRS). Two gas/surface systems were investigated namely water (D_2O) dissociation on a flat Cu(111) surface and methane dissociation on a stepped Pt(211) surface.

The dissociation of water molecules on an oxygen covered Cu(111) surface is presented first. In this study, I explain how I confirmed the reaction mechanism which leads to facile water dissociation on a Cu(111) surface pre-covered with oxygen atoms using isotopic labeling of the oxygen atoms coupled with RAIRS detection. Direct observation of the two different hydroxyl isotopologues on the surface showed that the water molecules dissociate on the surface by transferring an H-atom onto the oxygen adsorbate. At a surface temperature of 180 K, the reverse disproportionation reaction was observed to occur simultaneously with the dissociative adsorption of water molecules which resulted in the removal of the pre-covered oxygen isotope on the surface with continuous surface exposure to water molecules.

The study of water dissociation is continued but for a clean Cu(111) surface *i.e.* no pre-adsorbed oxygen atoms. The sticking probabilities of the dissociated water molecules were investigated by controlling the translational energy and the vibrational energy introduced into the incident water molecules. This experiment showed that the translational energy is better in promoting the dissociative chemisorption of D_2O on Cu(111) surface than vibrational energy.

The interaction between methylidyne-CH(ads) co-adsorbed with H(ads) atoms on a Pt(211) surface was investigated. Three distinct RAIRS absorption peaks were observed for the CH(ads) on the surface where the intensity of the peaks could be transferred from one to the other by changing the H atoms coverage on the surface. These peaks were then assigned to the methylidyne with 0, 1 or 2 neighbouring hydrogen atoms. The three hydrogen environments arose as a result of the limited one-dimensional diffusion of hydrogen atoms on the steps of the Pt(211) surface.

I conclude by summarizing the results from the studies presented in this thesis and showing future experiments that one could perform to understand the water molecules reaction on Cu surfaces better.

Résumé

Dans ma thèse, je présente une analyse des réactions de dissociation de molécules en phase gazeuse sur des surfaces métalliques monocristallines étudiées par un faisceau moléculaire en combinaison avec la spectroscopie infrarouge d'absorption par réflexion (RAIRS). Deux systèmes gaz/surface sont étudiés : la dissociation de l'eau (D_2O) sur une surface plane de Cu(111) et la dissociation du méthane sur une surface étagée de Pt(211).

La dissociation des molécules d'eau sur une surface Cu(111) couverte d'oxygène est présentée en premier. Dans cette étude, j'explique comment j'ai confirmé le mécanisme de réaction qui conduit à la dissociation facile de l'eau sur une surface Cu(111) pré-couvert d'atomes d'oxygène en utilisant le marquage isotopique des atomes d'oxygène couplé à la détection RAIRS. L'observation directe des deux isotopologues hydroxyles différents sur la surface a montré que les molécules d'eau se dissocient sur la surface en transférant un atome H sur l'adsorbat d'oxygène. À une température de surface de 180 K, j'ai pu observer que la réaction de disproportionnement inverse se produisait simultanément avec l'adsorption dissociative des molécules d'eau, ce qui a entraîné l'élimination de l'isotope d'oxygène pré-couvert sur la surface lors d'une exposition continue de la surface aux molécules d'eau.

L'étude de la dissociation de l'eau est poursuivie, mais pour une surface Cu(111) propre, c'est-à-dire sans atomes d'oxygène pré-adsorbés. Les probabilités d'adhésion des molécules d'eau dissociées ont été étudiées en contrôlant l'énergie translationnelle et l'énergie vibrationnelle introduites dans les molécules d'eau incidentes. Cette expérience a montré que l'énergie translationnelle est plus efficace pour promouvoir la chimisorption dissociative de D_2O sur la surface de Cu(111) que l'énergie vibrationnelle.

L'interaction entre le méthylidyne- CH(ads) co-adsorbé avec des atomes H(ads) sur une surface Pt(211) a été étudiée. Trois pics d'absorption RAIRS distincts ont été observés pour le CH(ads) sur la surface où l'intensité des pics pouvait être transférée de l'un à l'autre en changeant la couverture des atomes H sur la surface. Ces pics ont ensuite été attribués au méthylidyne avec 0, 1 ou 2 atomes d'hydrogène voisins. Les trois environnements d'hydrogène sont le résultat de la diffusion unidimensionnelle limitée des atomes d'hydrogène sur les marches de la surface de Pt(211).

En conclusion, j'expose des perspectives d'expériences futures que l'on pourrait réaliser pour mieux comprendre la réaction des molécules d'eau sur les surfaces de Cu.

Contents

LIST OF ABBREVIATIONS.....	8
ACKNOWLEDGEMENT	9
CHAPTER 1. INTRODUCTION	11
1.2 Gas-surface dynamics studies	13
1.2.1 Surface chemistry of H ₂ O	13
1.2.2 Quantum state resolved studies	15
1.2.3 Surface chemistry of CH ₄	17
1.3 Theoretical modelling of water/surface reactions	19
1.4 Thesis outline	21
CHAPTER 2. EXPERIMENTAL.....	23
2.1 Overview	23
2.2 Molecular beam/surface apparatus	24
2.2.1 Supersonic expansion and molecular beam velocity	25
2.2.2 Preparation of molecular beams of water and methane in helium.....	28
2.2.3 Sample preparation	31
2.2.4 Molecular beam flux	34
2.2.5 Gas-surface detection techniques	37
2.3 Quantum-state preparation of the molecular beam	46
2.3.1 Optical Parametric Oscillator (OPO).....	46
2.3.2 Frequency stabilization with Lamb Dip locking.....	48
2.3.3 Rapid Adiabatic Passage (RAP) for population inversion	51
2.3.4 Excited state population in the molecular beam	51
CHAPTER 3: CONFIRMING THE MECHANISM FOR WATER DISSOCIATION ON O-CU(111) USING ISOTOPE LABELING.....	55

3.1 Overview	55
3.2 D₂O interaction with ¹⁶O(ads) or ¹⁸O(ads) pre-covered Cu(111) surface	61
3.2.1 RAIRS detection of OH(ads) isotopologues	62
3.2.2 Saturation depends on the pre-dosed O(ads) coverage	68
3.3 Mechanism of water dissociation	70
3.3.1 Finding H atoms with RAIRS	70
3.3.2 Using HABS to identify the products of water dissociation	72
3.3.3 Reducing incoming water flux.....	78
3.4 Summary	81
CHAPTER 4: QUANTUM STATE RESOLVED D₂O REACTIVITY ON A CLEAN CU(111) SURFACE	83
4.1 Overview	83
4.2.1 RAIRS absorption to absolute coverage	85
4.2.2 S ₀ obtained from OD(ads) coverage vs dose of water molecules	89
4.3 Laser-off results.....	92
4.4 Laser-on results	95
4.5 Summary	104
CHAPTER 5: CH(ADS) CO-ADSORBED WITH HYDROGEN ATOMS ON A PT(211) SURFACE	105
5.1 Overview	105
5.2 RAIRS measurements of CH(ads) peaks	108
5.2.1 Three distinct CH(ads) absorption peaks	108
5.2.2 Why three discrete CH(ads) peaks?	112
5.2.3 H-D isotope exchange on the surface	115
5.3 Origin of the CH(ads): steps and/or terraces?.....	116
5.4 Conclusion	120

CHAPTER 6: CONCLUSIONS AND FUTURE WORK	122
6.1 Summary	122
6.1.1. Dissociation of water molecules on Cu(111)	122
6.1.2 Methylidyne co-adsorbed with hydrogen atoms on a Pt(211)	122
6.2 Future work	123
6.2.1 Facile OD(ads) to OH(ads) exchange	123
6.2.2 Site-selective water dissociation study on stepped surfaces using RAIRS	125
6.2.3 Vibrational mode specific water dissociation on Cu(111).....	126
6.2.4 Bond selectivity study of HOD	127
6.2.5 Quantum state resolved study of CO ₂ dissociation on a Cu(111)	128
 REFERENCES.....	 130
 LIST OF FIGURES.....	 138
 LIST OF TABLES.....	 146
 CURRICULUM VITAE.....	 147

List of abbreviations

AES	Auger Electron Spectroscopy
DFT	Density Functional Theory
FTIR	Fourier Transform Infrared Spectroscopy
HABS	Hydrogen Atom Beam Source
IR	Infrared Spectroscopy
IVR	Intramolecular Vibrational Redistribution
K&W	King and Wells
MB	Molecular Beam
ML	monolayer
OPO	Optical Parametric Oscillator
PES	Potential Energy Surface
QMS	Quadrupole Mass Spectrometer
RAIRS	Reflection Absorption Infrared Spectroscopy
RAP	Rapid Adiabatic Passage
RPH	Reaction Path Hamiltonian
SEM	Secondary Electron Multiplier
STM	Scanning Tunnelling Microscopy
SVP	Sudden Vector Projection
TOF	Time-of-flight
TPD	Temperature Programmed Desorption
UHV	Ultra-high Vacuum
WGSR	Water-Gas Shift Reaction
XPS	X-ray Photoelectron Spectroscopy
ZPE	Zero Point Energy

Acknowledgement

During my Ph.D., I have gained a lot of beautiful experiences and most of all I learned to not give up when a problem at hand becomes more challenging than expected. However, it was not always easy especially on days where I have been working on the same scientific problem for months or even years! It was during these tough times that many people were very kind and helpful to me therefore, leading me to complete my Ph.D. project successfully. I would like to take this opportunity to thank them all. First and foremost, I would like to thank my supervisor,

Prof. Rainer Beck for giving me the opportunity to work with him in his research lab. He was very supportive throughout my Ph.D. and there were times when his encouraging words of, 'Don't worry, we will figure it out' was what kept me going. I have learned a lot about thinking and solving problems systematically from him and I found it really useful not only in the lab but also outside of the lab. Rainer is always available to help all his students and I really appreciate all the assistance he provided me in order for my experiments to run more smoothly.

Next, I would like to thank **Dr. Ana Gutiérrez González**, for teaching me how to work with the RAIRS machine and demonstrating to me that one can be creative in finding solutions to problems in science. Most of all, thank you Ana for showing me that it is alright to make mistakes because we learn through mistakes. Also, I really appreciate your presence in the lab because you made it so fun to work.

Another person who was there almost throughout my entire Ph.D. is **Dr. Bo-Jung Chen**. I would like to thank him for being a caring friend especially during the time when we were the only students in our group. Thanks for explaining many different concepts to me and teaching me how to use SolidWorks because it is indeed fun, just like you said it would be!

To **Mateusz Suchodol**, thank you from the bottom of my heart for working with me, helping me to perform measurements and being a great lab partner. It was really fun working with you and I will never forget the times when we had to perform acrobatic moves to fix the machine. Also, I am very grateful for all your help with measurements towards the end of my PhD.

Thank you also to **Iwona Swiderska**, our Masters student. I really enjoyed working with you and all the laughs we had in the lab. To our post-doc, **Dr. Christopher Scott Reilly**, thank you for all the quizzes you put up on the whiteboard and above all, thank you for spending time to clear my doubts, anytime I ask. **Patrick Floss**, thank you for helping with the laser set-up and your tasty carrot cakes!

To **Angeles Alarcon** and **Odegaard Anne Lene**, I would like thank you both for being just an email away. I really appreciate all the help you provided me when I first move to Switzerland and the administrative work that you still take care for me.

Apart from the those who worked with me in the laboratory, I would also like to thank people in the mechanical workshop, electronic workshop and the IT department for always being available to fix and/or to build new parts for the RAIRS machine.

Staying away from my family especially in the times of Covid was really difficult and I must thank **Giulio de Vito** for always being by my side, making me feel at home and encouraging me whenever I needed a boost. I must also thank my parents, **Vejayan Athymulam** and **Bathmavathy Sinnapaian** for always loving, supporting and inspiring me to do science since young. I have a big family in Malaysia and I would like to thank all of them for their love and care especially my sisters, Buvana and Ratchanah as well as Poovan mama who are available whenever I call them. Thank you again to everyone who played a part in this beautiful and challenging journey.

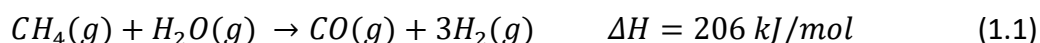
Chapter 1. Introduction

1.1 Motivation

Heterogeneous catalysis undoubtedly plays an essential role in efficiently converting raw materials into useful chemicals and fuels. One such example is the Haber-Bosch process which converts nitrogen and hydrogen into ammonia at high temperature and pressure using an iron catalyst¹. The ammonia formed is mainly used for the production of fertilizers which allows our agriculture to sustain the increasing population on our planet¹.

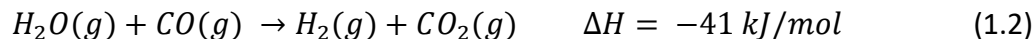
As surface scientists, we are constantly looking to develop and improve catalysts used for chemical reactions as significant improvement can be introduced into a reaction with the right catalyst. The Sabatier principle states that “an ideal catalyst must bind to the reactant at an intermediate strength which is neither too weak nor too strong”^{2,3}. This is because a weakly binding catalyst has low probability of keeping the reactants bound and converting them into products. On the other hand, a strongly bound reactant will not free up the catalyst for other reactants after being converted into products.

Currently, the rising demand for energy has placed renewable sources of energy such as H₂ in the limelight. The primary source for H₂ gas is from the steam reforming reaction between methane and water⁴:



The products obtained are the syngas, CO and H₂ which are fed into the Fischer-Tropsch synthesis to form valuable hydrocarbons⁴. In the steam reforming reaction, the dissociative adsorption of methane is the rate limiting step. Although many late transition metals (Pd, Pt and Ru) could be employed as catalysts for this reaction, a Ni-based catalyst is used in industry because it is cheaper⁴.

More hydrogen is then extracted by reacting the product obtained from the steam reforming process, CO with water molecules. This reaction is called the water gas shift reaction (WGSR):



WGSR is exothermic therefore it is thermodynamically favoured at low temperature (~ 200 °C) but kinetically favoured at high temperature (400-500 °C)⁵. At low temperature, copper-based catalysts are employed while at high temperature iron-based catalysts are used⁵. Water dissociation is the rate-limiting step in WGSR hence there is a lot of interest among surface scientists in understanding it in more depth. This is especially true due to the prospect of H₂ becoming an important source of energy which leads to water splitting studies to become increasingly attractive.

To understand these heterogeneous catalyses reactions better, we employ simpler systems in our lab where single crystal metal surfaces with specific surface structures are reacted with gas molecules in an ultra-high vacuum (UHV) chamber. The conditions used in these experiments can be controlled carefully therefore allowing for better understanding of the rate-limiting steps in the reactions mentioned above. On top of that, we also perform quantum state resolved studies where the incident gas molecules are prepared in a specific ro-vibrational state before colliding with the surface.

Most of the catalysts used for the chemical reactions are currently determined through trial and error. To ensure that in future, we no longer need to proceed by testing every metal or metal alloy to find the best catalyst for a reaction, advanced theoretical modelling of gas/surface reactions is needed. Since our experiments are performed with well-defined metal surfaces and gas molecules prepared in specific ro-vibrational states, we obtain detailed data which are ideal for testing theoretical models.

1.2 Gas-surface dynamics studies

1.2.1 Surface chemistry of H₂O

Water is important in many studies such as catalysis, electrochemistry, and material science ⁶. The variety of chemical reactions in which water molecule is involved together with its rich molecular properties makes it a very interesting molecule to be studied. One such fascinating property may be observed in surface adsorbed water molecules. On different substrates, water was observed to exist in various forms for instance as monomer, dimer, 2D layer or 3D clusters ⁶. Water can also convert from one structure to another depending on its surface coverage and surface temperature ⁷. Another intriguing property of water is the strong hydrogen bonding that dictates the outcome of many surface reactions. For instance, if the intermolecular hydrogen bonding is stronger than the water/surface bonding then, water would typically exist as clusters but when the water binds more strongly to the surface, water will dissociate on the surface ⁶.

Over the past decades, extensive research has been conducted on water molecules which have been compiled into two reviews by Thiel and Madey in 1987 and by Henderson in 2002 ^{6,8}. One important theme of discussion in both the reviews is the fate of water molecules arriving on a surface. Do they adsorb molecularly or dissociate?

In order to identify if a reaction between water molecules and a metal surface resulted in breaking of one O-H bond or not, one needs to be able to identify the products. The challenge arises when the dissociated water molecules undergo either reversible or irreversible reaction, *i.e. product is not stable* ⁶. In reversible water dissociation reaction, the nascent products are thermodynamically driven to recombinatively desorb as water molecules, $\text{H}_2\text{O}(\text{a}) \rightarrow \text{OH}(\text{ads}) + \text{H}(\text{ads}) \rightarrow \text{H}_2\text{O}(\text{g})$ while in the irreversible reaction, water dissociates but the products do not recombine instead dehydrogenate further resulting in surface oxidation, $\text{H}_2\text{O}(\text{a}) \rightarrow \text{OH}(\text{ads}) + \text{H}(\text{ads}) \rightarrow \text{O}(\text{ads}) + \text{H}_2(\text{g})$. In general, metal and semiconductor surfaces favour irreversible dissociation whereas oxide surfaces undergo reversible water dissociation ⁶. The irreversible water dissociation is easier to be identified due to the H₂(g) liberation from the surface unlike the reversible reaction.

On metal surfaces, a 2D amorphous structure of water was reported to appear below $T_s < 120$ K⁹. Above $T_s = 135$ K, water molecules on hydrophilic surfaces diffuse and coalesce into an extended and ordered 2D film with hydrogen bond network,¹⁰⁻¹². Whereas, on hydrophobic surfaces nucleation of ice clusters occurs instead⁷. Continuous surface exposure to water molecules at $T_s = 120$ K was observed to produce ice multilayers on metals such as Ni, Pt and Rh¹³. The 2D film (monolayer) and the 3D clusters (multilayer) were distinguished through their desorption temperatures as the 2D film on a wetting surface is more stable than the water molecules in the 3D structure¹⁴. Thus, water from the 2D layer desorbs at a higher temperature than the clusters.

Dubois *et al.* reported that a clean Cu(111) surface is non-wetting therefore only a single peak was observed in the temperature programmed desorption measurement for a Cu(111) surface covered with ice layers⁷. The peak was assigned to the desorption of multilayer clusters. This observation is in contrast to wetting surfaces such as Pd(111) and Rh(111) which showed two desorption peaks corresponding to the monolayer and multilayer water desorption from the surface^{7,13}.

As mentioned previously, hydrogen bonding in water molecules plays a major role in its reaction with surfaces. Yamamoto *et al.*, showed that the wetting properties of a surface can be tuned with surface hydroxyls¹⁵. The authors studied water interaction with Cu(110) and Cu(111) surfaces at near ambient conditions (1 Torr, 295 K) and demonstrated that the Cu(110) is hydrophilic but a clean Cu(111) is hydrophobic. The wetting layer on the Cu(110) was composed of a mixture of OH(ads) + H₂O(ads), where the adsorbed OH stabilised the trapped water molecules through hydrogen bonding. Interestingly, when the Cu(111) surface was covered with O(ads) followed by water exposure, a mixture of OH(ads) + H₂O(ads) was observed. The hydrophobic Cu(111) became hydrophilic due to the hydrogen bonding between the surface hydroxyls and the water molecules.

Although there are many studies performed to understand the reaction between water molecules and metal surfaces, quantum state resolved experiments for water dissociation are still limited. In the following section, I will present examples of experiments conducted with ro-vibrationally excited CH₄ gas molecules which could act as benchmarks for quantum state resolved study of water dissociation.

1.2.2 Quantum state resolved studies

In order for reactants to overcome an activation barrier and convert into products, one needs to provide energy to the reactants. A model proposed by Polanyi relates the location of the barrier on the potential energy surface (PES) to the energy required for the chemical reaction and the energy disposed in the products¹⁶. Using the reaction between an atom and diatomic molecule ($A + BC \rightarrow AB + C$), he explained that when the transition state of the reaction is closer to the entrance channel as shown in Figure 1.1- plots on the left, the reaction is considered as an “early barrier” reaction. In this case, at the transition state the BC bond length is in equilibrium hence adding translational energy is more efficient in promoting reaction compared to vibrational energy.

On the other hand, for the “late barrier” reactions presented in Figure 1.1- plots on the right, the BC bond is stretched at the transition state. Therefore, adding vibrational energy to the reactants will enhance the reaction more efficiently than adding the same amount of translational energy.

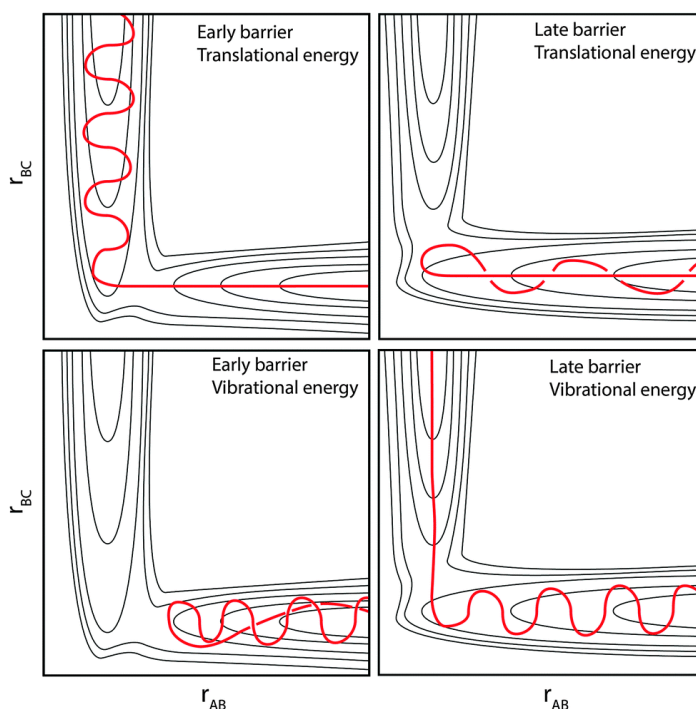


Fig. 1.1: Schematic of the PES for the reaction between $A + BC$ to form $AB + C$, where r_{BC} and r_{AB} represent the interatomic distance between BC reactant and AB product, respectively. In the left plots, the transition state is closer to the entrance channel, in contrary to the plots on the right where the transition state is closer to the exit channel. The effect of adding either translational or vibrational energy can be observed from the red line. Reproduced with permission from¹⁷

Polanyi's model was developed to explain simple gas phase reaction involving an atom and a diatomic molecule. Therefore, it may not be sufficient to describe inherently complicated systems which include polyatomic molecules and surfaces. For instance, a study performed by colliding vibrationally excited methane molecules on a Ni(100) surface resulted in the dissociative chemisorption of the methane on the surface¹⁸. The authors reported that when the incident methane molecules were excited to ν_3 -antisymmetric stretch, the reaction was promoted less compared to addition of translational energy. However, if the methane molecules were excited to the ν_1 -symmetric stretch mode, the reaction efficacy was found to be 1.4¹⁹. These observations show that different vibrational modes enhance reactions differently.

1.2.2.1 Mode specificity

When different vibrational modes of a molecule with the same energy (isoenergetic) cause a reaction to be enhanced differently, we call this 'mode specificity'. The first demonstration of mode specificity in a molecule/surface reaction was with deuterated methane, CH₂D₂ excited to two different overtone vibrations, $2\nu_6$ and $\nu_1 + \nu_6$ and a Ni(100) surface²⁰. In the local mode basis, the two states can be described as |20> denoting 2 quanta of CH stretch in a single bond and |11> indicating one quantum of CH stretch in each of the C-H bonds of the CH₂D₂. Although both states have same amount of vibrational energy, the methane molecules in the $2\nu_6$ state was found to be 5 times more reactive than $\nu_1 + \nu_6$ demonstrating mode specificity in this reaction.

A second study uncovered mode specificity by comparing the dissociation probability of ν_1 and ν_3 excited CH₄ on Ni(100) performed by Maroni *et al.* in 2003 with CH₄ molecules and a Ni(100) surface in our group¹⁹. The incident methane molecules were vibrationally excited to the ν_1 -symmetric stretch by stimulated Raman pumping. Its reactivity was found to be an order of magnitude larger than the reported dissociative adsorption of methane with ν_3 -antisymmetric stretching^{18,19}. This indicates that the symmetric stretch of the methane molecules are along the reaction coordinate hence it caused higher reactivity.

As for water molecules, the first state-resolved experimental study of dissociative adsorption of water molecules, D₂O on a metal surface was performed in our lab²¹.

Deuterated water molecules were collided with a Ni(111) surface and the dissociation was found to be promoted by both translational and vibrational energies. The impinging water molecules were excited into ν_3 or $2\nu_3$ vibrational levels and the dissociation probabilities for the vibrational excitation was found to be higher than for adding equal amount of translation energy.

1.2.2.2 Bond selectivity

The first bond selective chemical reaction was demonstrated by Sinha et al. in 1990 for a bimolecular reaction between singly deuterated water, HOD(g), and H atoms²². They excited the third overtone of the O-H stretch in the HOD molecules ($4\nu_{\text{O-H}}$) and then reacted them with H atoms. This was followed by measurement of the products using partially saturated laser induced fluorescence. The authors reported that the excited bond was preferentially dissociated and produced more than 100:1 ratio of OD:OH.

The ability to manipulate the outcome of a chemical reaction by exciting a specific bond in a molecule is truly a large step forward in chemistry. The first evidence for bond selective dissociation of a gas/surface system was presented by Killelea *et al.*²³. They performed the experiment by colliding CHD₃(g) on a Ni(111) surface. Prior to the collision, the Ni surface was titrated with D atoms. The dissociation products were identified through recombinative desorption measurements, which showed that for the CHD₃(g) incident gas molecules prepared in the ν_1 C-H stretch resulted in a product ratio of >30:1 for CD₃:CHD₂. This is in contrast to the statistical outcome expected, 1:3 proving bond selective dissociation.

Although water was initially used to prove bond selectivity in a chemical reaction, water/metal surface reactions are yet to be explored with bond selective studies. In my research, I was interested in exploring dissociative adsorption of ro-vibrationally excited water molecules on a clean Cu(111) surface which I present in more details in Chapter 4.

1.2.3 Surface chemistry of CH₄

Studies of methane dissociation on catalytically active transition metal surfaces such as Pt(111), Pt(211) and Ni(100) have been performed in our group^{19,24,25}. The investigations showed that methane dissociation is a direct dissociation which occurs immediately on

impact, that is activated both by incident translational and vibrational energy and that the dissociation is mode specific and bond selective. Apart from understanding the reaction of a single molecule on a surface, it is also very important for surface chemists to study the interaction between co-adsorbed molecules as they can either promote, hinder or change a reaction.

Fisher-Tropsch synthesis converts the syngas, CO and H₂ into hydrocarbons over a catalyst. The CH_x(ads) fragments (where x= 1, 2 or 3) are the typical intermediates and they undergo complex surface reaction consisting of hydrogenation, dehydrogenation and coupling during the synthesis. In a study performed by Xu *et al.* the reaction path of the alkyl formation was found to depend on the co-adsorbed species on the surface²⁶. In their study, CH₃I(g) was reacted with a Co(0001) surface at T_s = 100 K which mostly produced CH₃(ads) and CH(ads). Upon surface heating, the CH(ads) fragments were observed to hydrogenate into CH₄(g) or longer hydrocarbon chains depending on the co-adsorbed species. Co-adsorption with H(ads) converted the CH(ads) into CH₄(g) whereas CO(ads) stabilised the CH₂(ads) species and converted it into C₂H₆(g) or C₂H₄(g) as shown in Fig. 1.2. In my study, I studied the interaction between the simplest hydrocarbon adsorbate, CH(ads) on a stepped Pt(211) surface co-adsorbed with H atoms. The study is presented in Chapter 5.

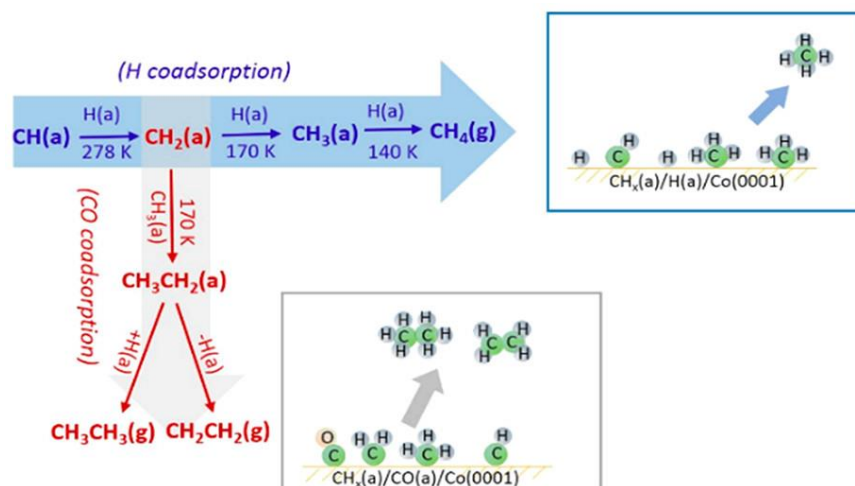


Fig. 1.2: The reaction pathway of CH(ads) species on the surface with co-adsorbed hydrogen atoms or CO(ads) on a Co(0001) surface. Reproduced with permission from²⁶.

1.3 Theoretical modelling of water/surface reactions

Developing theoretical models for gas/surface reaction dynamics has become a highly active field of study as it is relevant for heterogeneous catalysis. Due to the involvement of a surface, theoretical simulation for this reaction is more complex as it requires modelling of high-dimensional PES unlike chemical reactions involving only gas molecules. One main goal of modelling the gas/surface dynamics accurately is to understand and predict dissociative chemisorption of gas molecules on transition metal surfaces as this is often the rate-limiting step for many heterogeneous catalysis processes such as steam-reforming and WGS^R ⁴.

A chemical reaction between gas molecules and surface is easier to be modelled if it involves diatomic gas molecules rather than polyatomic molecules. Diatomic molecules are small enough for performing full-dimensional, i.e. six-dimensional, quantum dynamics calculations with, such as the dissociative adsorption of H₂ on metal surfaces ^{27,28}. This is in contrast with polyatomic molecules which have many more degrees of freedom and therefore are complex and difficult to be studied at full-dimensional quantum mechanical level as they require high-dimensional PES. It is challenging for both DFT and *ab initio* calculations to provide accurate description of the surface and the polyatomic molecules at the same time ^{29,30}.

In constructing an accurate global PES for the reaction of water on a metal surface, one needs to consider the nine degrees of freedom of the water molecules on a rigid surface. This challenging task becomes even more difficult when one requires quantum dynamical calculations of the fully coupled 9D model. Therefore, most theoretical studies of water reaction on metal surfaces have been performed with reduced-dimensional or approximate quantum models. For instance, Mondal and co-workers used reduced dimensionality (3D) for water dissociation on Cu(111) investigation using the simplest pseudo diatomic molecule, HO-H model ³¹.

In 2015, Farjamnia and Jackson reported the study of water dissociation on the Ni(111) surface using an approximate approach based on a reaction path Hamiltonian (RPH) ³². In this method, all the internal motions of the water molecules were treated using a vibrationally adiabatic basis set. Effects of lattice motion was included in their investigation using sudden models and they demonstrated that with increasing surface temperature, the sticking

probabilities changes as a result of lattice motion, similar to the observation for methane dissociation on metal surfaces^{33,34}.

Jiang *et al.* employed the reduced-dimensional quantum approach to investigate dissociative water chemisorption on a flat Cu(111) surface^{35,36}. In their studies, Jiang and co-workers explored the mode specificity of H₂O and bond selectivity of HOD on Cu(111) by using 6D quantum dynamical approach where the 6D model (3 vibrational degrees of freedom, 2 rotational degrees of freedom and molecule-surface distance) excluded any effects from impact site and corrugation on the surface. A sudden vector projection (SVP) model was used to explain the strong mode specificity of water dissociation on the Cu(111)³⁷. The SVP model is based on the premise that the gas/surface collision is faster than the intramolecular vibrational redistribution (IVR) rendering a strong influence of how the reactant mode is coupled to the reaction coordinate at the transition state³⁸.

When the first quantum state resolved molecular beam experiment for water dissociation was reported on Ni(111), the asymmetric O-D stretch mode of D₂O was found to strongly promote the reaction²¹. A reduced-dimensional (6D) quantum approach was used to understand the mode specificity in this reaction, where an approximation for the lattice motion and impact site effects were included. The authors rationalised the vibrational enhancement of water dissociation on the Ni(111) using the SVP model.

In 2016, Zhang and co-workers presented their study of water dissociation on a rigid Cu(111) surface using full-dimensional quantum dynamics method³⁹. All the nine degrees of freedom of water molecules were allowed to be fully coupled. The authors reported vibrational energy to promote the reaction better than translational energy as predicted for a late barrier reaction however, their calculations predicted the asymmetric stretch mode of H₂O to promote its dissociative chemisorption on the surface more strongly than the symmetric stretch at high energies. On the other hand, Jiang *et al.* performed similar experiment with H₂O/Cu(111) using a reduced- dimensional approach with a 6D model resulting in a prediction that the symmetric stretch have higher reactivity than the asymmetric stretch for the dissociative chemisorption of H₂O on Cu(111)³⁵. The discrepancy in the predictions stem from the different models used for their calculations. As we are able to perform quantum state resolved experiments in our lab, it will be really interesting to test

these predictions and provide more insight into the mode specific reactivity of water on the Cu(111).

1.4 Thesis outline

The studies in this thesis can be divided into two main parts based on the gas/surface systems used, H₂O/Cu(111) and CH₄/Pt(211). The former will be presented first with results from water interaction on both a clean and partially oxygen covered Cu(111) surface. After that, I will present experiments performed on a Pt(211) surface where methane molecules dehydrogenate to form methylidyne, CH(ads) followed by discussion on its interaction with co-adsorbed H(ads).

The goals of my studies are to use RAIRS and oxygen isotopes to confirm that water dissociation on a partially oxygen covered surface proceeds through the breaking one O-H bond in the water molecule via H atom abstraction by the surface oxygen. This became a study of interest when we observed facile water dissociation on clean Cu(111) surface with RAIRS. Water dissociation on a clean Cu(111) surface is predicted to have a large activation barrier therefore, it was really surprising to observe water dissociating when the incident molecules had only 0.28 eV of translational energy. With more research, it became clear that there were traces of O₂ in the molecular beam which arrived on the surface resulting in partial surface coverage with oxygen atoms. The surface oxygen atoms were found to facilitate water dissociation. Based on this, I decided to investigate the water dissociation mechanism on a partially oxygen covered Cu(111) surface.

Another goal is to measure the sticking coefficients for dissociative adsorption of rotationally excited water molecules on a clean Cu(111) surface. These measurements are intended to test calculations which predict vibrational energy to be more efficient in promoting water dissociation compared to translational energy. Finally, I aim to investigate the interaction of CH(ads) co-adsorbed with H(ads) on a stepped Pt(211) surface.

The thesis is arranged in the following manner:

In Chapter 2, I describe the apparatus and the techniques used to probe the gas/surface interactions.

In Chapter 3, I show how RAIRS coupled with isotope labeling can be a powerful tool in understanding surface reaction mechanism. I present RAIRS spectra confirming the water dissociation mechanism on a partially oxygen covered Cu(111) surface using oxygen isotopes, $^{16}\text{O}_2$ and $^{18}\text{O}_2$. The hypotheses tested for understanding the reaction of water on the oxygen covered surface are presented and discussed in detail.

In Chapter 4, I describe the quantum state resolved sticking coefficients measured for water molecules on a clean Cu(111) surface. The measurements are obtained with RAIRS spectra showing another useful way of employing RAIRS to study the reactivity of gas molecules on a metal surface.

In Chapter 5, I describe a surprising observation in RAIR spectra exhibited by methylidyne co-adsorbed with hydrogen atoms on a Pt(211) surface. The role played by the surface hydrogen atoms are explained with RAIRS measurements and DFT calculations.

In Chapter 6, I summarize the important findings from my work on the two gas/surface systems and describe other experiments which can be performed in the future.

Chapter 2. Experimental

2.1 Overview

All the experiments in this thesis were performed using the molecular beam/surface apparatus shown in Fig. 2.1. The details of this apparatus are described elsewhere^{40,41}. Therefore, in my dissertation I will only focus on the modifications performed to this machine and the techniques used to perform the gas/surface studies.

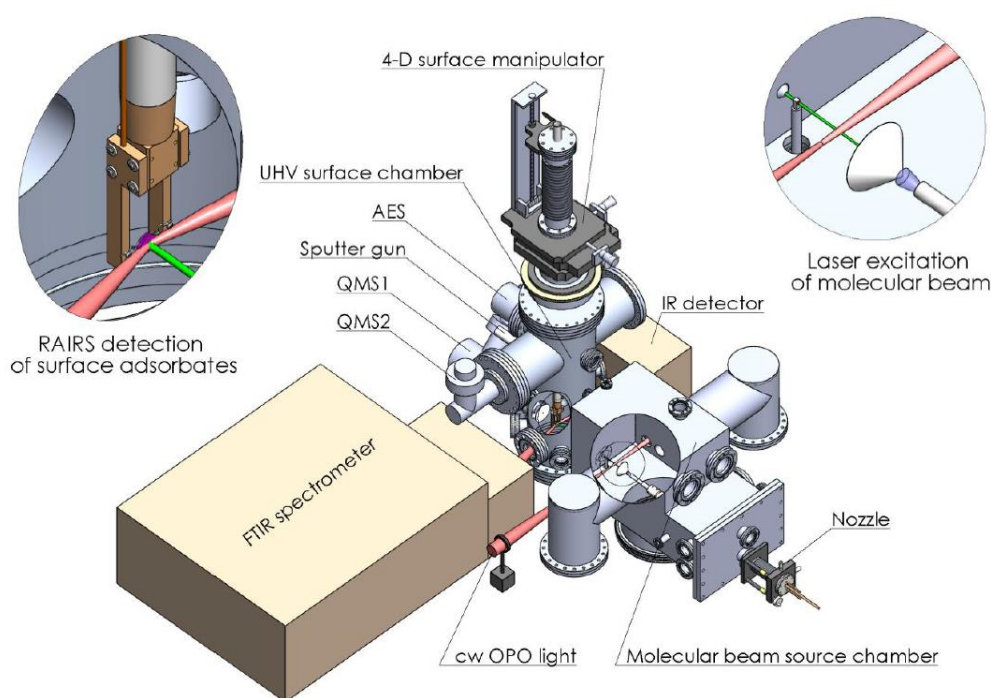


Fig. 2.1: 3D model from SolidWorks of the ultra-high vacuum set-up used in this thesis. Reproduced from Li Chen's dissertation⁴⁰.

A molecular beam (MB) is prepared in the source chamber from a supersonic jet expansion using a 2 mm electroformed nickel skimmer (Beam Dynamics). The molecular beam passes through two differential pumping stages before entering the ultra-high vacuum (UHV) chamber with a base pressure of $2 \cdot 10^{-11}$ mbar where a single crystal metal surface is located. Fig. 2.1 shows the Fourier Transform Infrared (FTIR) Spectrometer placed on the left of the machine where the IR light leaves the spectrometer and is reflected off the sample surface inside the UHV chamber and then detected by an external infrared (IR) detector on the right

of the machine. The whole IR beam path is evacuated by coupling the UHV chamber to the evacuated FTIR and detector box with flexible stainless steel bellows.

The incident molecules can be prepared by infrared excitation in specific ro-vibrationally excited states using a single mode continuous wave (cw) infrared optical parametric oscillator (OPO). The IR excitation of the molecular beam is performed in the source chamber, just before the skimmer as shown in the inset in Fig. 2.1 (top right corner, in circle). After preparation of the molecules in a specific excited state, the fraction of excited molecules can be measured using a room temperature pyroelectric detector. The detector is placed right before the UHV chamber and it can be moved into the molecular beam path.

In this thesis, I describe studies involving two different gas/surface reactions which are the dissociation of water molecules with a Cu(111) surface and the dissociation of methane molecules on a Pt(211) surface. The surface analysis techniques used are Reflection Absorption Infrared Spectroscopy (RAIRS), Auger electron spectroscopy (AES), King and Wells (K&W) beam reflectivity measurements, and Temperature Programmed Desorption (TPD). In the following sections, I will explain in detail the techniques used to analyse the gas/surface interactions as well as the cleaning procedures used for the Cu(111) and Pt(211) surface samples.

2.2 Molecular beam/surface apparatus

This sub-chapter can be divided into three main parts, (i) generation of a molecular beam and its characterisation, (ii) surface sample preparation and (iii) adsorbate detection techniques.

Briefly, a molecular beam is formed in the source chamber (P1) by skimming a supersonic expansion with a 2 mm diameter skimmer as shown in Fig. 2.2. The molecular beam then travels through a chopper wheel with two 2 mm slits and a separation valve in the second chamber before entering the third chamber. A pyroelectric detector which can be translated vertically into the molecular beam for the detection and the measurement of the excited fraction of the state prepared molecules in the molecular beam for the state-resolved experiments. When the pyroelectric detector is retracted, the molecular beam enters the

UHV chamber where it collides with either a mica flag (10 mm x 10 mm) or the target surface (\varnothing 10 mm). The mica flag can be moved in and out of the molecular beam path and is used to perform K&W measurement of the sticking coefficient.

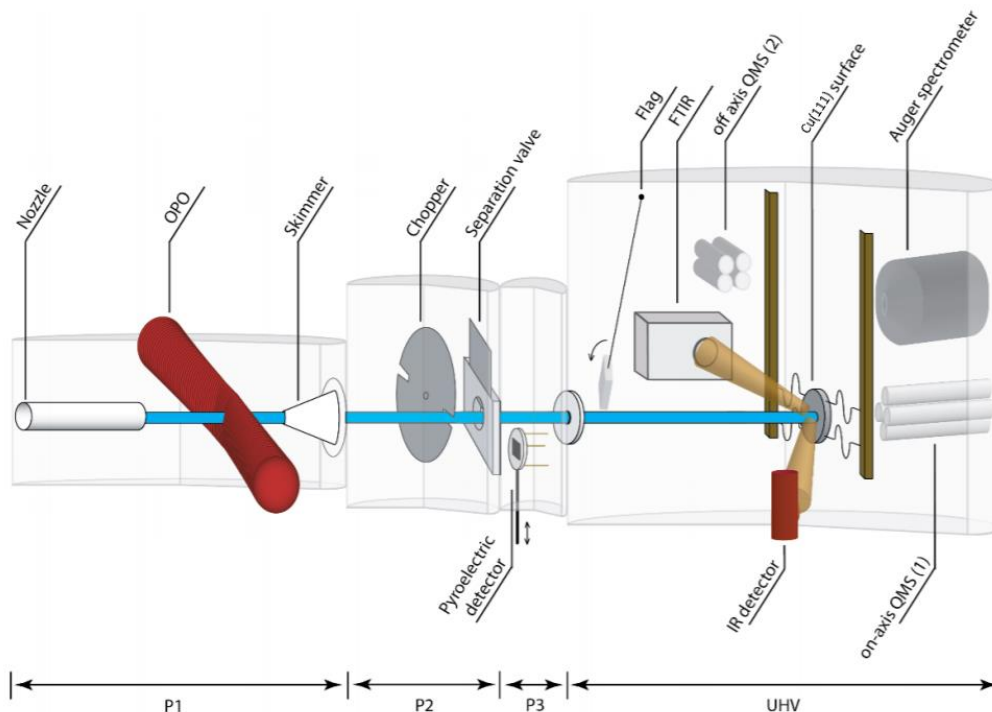


Fig. 2.2: A schematic diagram showing the path of the molecular beam (blue) and the position of the different surface probing apparatus in the machine. P1- refers to the first chamber where the supersonic expansion of the molecular beam takes place. P2- refers to the second chamber where the chopper and the separation valve reside. P3- refers to the third chamber, the smallest chamber in the machine which has a pyroelectric detector that can be translated in and out of the molecular beam path. P4- refers to the ultra-high vacuum chamber where the gas/surface reaction takes place. Diagram taken from Ana Gutiérrez-González's thesis ⁴².

2.2.1 Supersonic expansion and molecular beam velocity

A supersonic expansion is a very useful tool for the preparation of molecular beams for atomic and molecular physics studies as it allows a sample of molecules to be prepared under collision free conditions and with a well-defined kinetic energy as well as with efficient internal energy cooling. The molecular beams used in this thesis are prepared by expanding gas mixtures through a 50-100 micron nozzle from a stagnation pressure of 1-3 bar into the first chamber, typically with 10^{-7} mbar pressure. By placing a skimmer downstream from the

nozzle, in the *zone of silence* of the expansion, only the molecules in the centre region of the supersonic expanded jet are passed to the next stages of the set-up, Fig. 2.3.

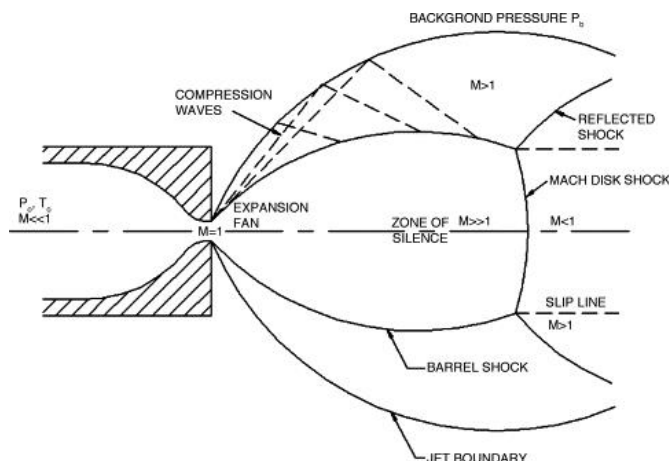


Fig. 2.3: Supersonic jet expansion in the nozzle. Reproduced with permission from ⁴³.

When the molecules flow from a region with high pressure into a region with very low pressure through a small orifice in the nozzle (in this case, \varnothing 100 μm), a supersonic expansion occurs. During the expansion, the molecules experience a high number of collisions which cause the random thermal motion of the molecules to be converted into a directed motion with narrow beam velocity distribution. This adiabatic process also results in efficient cooling of the rotational degrees of freedom of the molecules which is really helpful in the study of molecular structure where spectral congestion is reduced thus allowing interpretable spectra to be measured ⁴⁴.

The maximum or terminal velocity achieved by the gas molecules after expansion depends on the temperature of the gas before expansion, the heat capacity of the gas and the average molecular mass of the gas mixture. The terminal velocity of an adiabatic expansion is given by,

$$v_{\infty} = \sqrt{\frac{2k_B}{\langle m \rangle} \frac{\langle \gamma \rangle}{\langle \gamma \rangle - 1} T_N} \quad (2.1)$$

Where k_B is the Boltzmann constant, $\langle m \rangle$ is the average molecular mass of the gas mixture with X molar fraction of i constituents, $\langle m \rangle = \sum_i X_i m_i$ and $\langle \gamma \rangle$ is the molar average ratio of the heat capacity, $\langle \gamma \rangle = \sum_i X_i \gamma_i$, where $\gamma = \frac{c_p}{c_v}$. There are two ways to control the translational energy of the gas molecules namely, (i) seeding the heavier gas molecules in a lighter carrier gas such as He or H₂ and variation of the seed ratio and (ii) changing the nozzle temperature.

The velocity distribution of the molecular beam is characterized by time-of-flight (TOF) measurements using a quadrupole-mass-spectrometer (QMS) in combination with a chopper wheel. The QMS on-axis (Pfeiffer, QMA 400, QMH 400-5, QMG 421) is installed in the line-of-sight of the molecular beam in the UHV chamber and the chopper is located in the second differential pumping stage. The chopper wheel has two slits of 2 mm width. A continuous molecular beam travelling into the second chamber is chopped by the chopper wheel (typically at 200 Hz) into packets of molecules. The EPOS2 software is used to control the DC chopper motor from Maxon. An opto-coupler placed at 180° to the molecular beam path senses the passing of the opposite slit and serves as the start trigger of multichannel analyser (MCA-3/P7882). Following the start pulse, the MCA counts the ion-pulses from the secondary electron multiplier (SEM) and records their time of arrival. A MATLAB script is used to fit a flux weighted Boltzmann velocity distribution convoluted with a chopper function to the measured TOF distribution. The resulting velocity distribution is then converted to the kinetic energy distributions of the molecular beam.

The measured arrival time of the molecules includes the travel time of the neutral molecules ($t_{neutral}$), ion flight time (t_{ions}) and the chopper delay ($t_{chopper}$).

$$t_{TOF} = t_{neutral} + t_{ions} + t_{chopper} \quad (2.2)$$

By removing the chopper delay and ion flight time from the total time-of-flight, one can determine the neutral molecules' travel time. Further details of TOF calibrations can be found in Li Chen's thesis⁴⁰. The following table 1 shows the translation energy of the D₂O molecules seeded in He, at different nozzle temperatures used in this thesis, measured by the TOF method. The velocities of the CH₄ molecules used for the study of methylidyne on Pt(211) surface are also included.

Table 1: Average speed and translational energy of the D₂O molecules and CH₄ molecules in the gas mixtures specified, as function of nozzle temperatures.

Gas mixtures	T _n (K)	E _{kin} (kJ/ mol)	ΔE = FWHM/ E _{kin}
2% D₂O in He	300	27	0.22
	400	34	0.21
	500	42	0.21
	600	50	0.22
	700	58	0.24
	800	65	0.25
	900	72	0.26
	1000	79	0.28
	1050	83	0.28
3% CH₄ in He	500	41	0.25
	800	64	0.40

2.2.2 Preparation of molecular beams of water and methane in helium

During my thesis research, a new set-up for the molecular beam source was built and installed with help from Dr. Daniel Auerbach. The following 3D SolidWorks image in Fig. 2.4 shows the new nozzle assembly. This new design is based on the molecular beam source previously developed by Dr. Daniel Auerbach and co-worker in 1992⁴⁵. The stainless steel nozzle is held by two water cooled copper clamps which can bend to allow for thermal expansion of the nozzle without imposing bending stress on the copper tubes. The nozzle is heated resistively by passing current along its length from one copper clamp to the other. A hole of ~50-100 μm size is laser drilled in the centre of the nozzle tube to allow for the supersonic expansion of the molecular beam. Since this new assembly does not require the nozzle to be welded (unlike the previous nozzle design which can be found elsewhere⁴⁰), it is therefore easier to replace the nozzle of different materials such as Au and W.

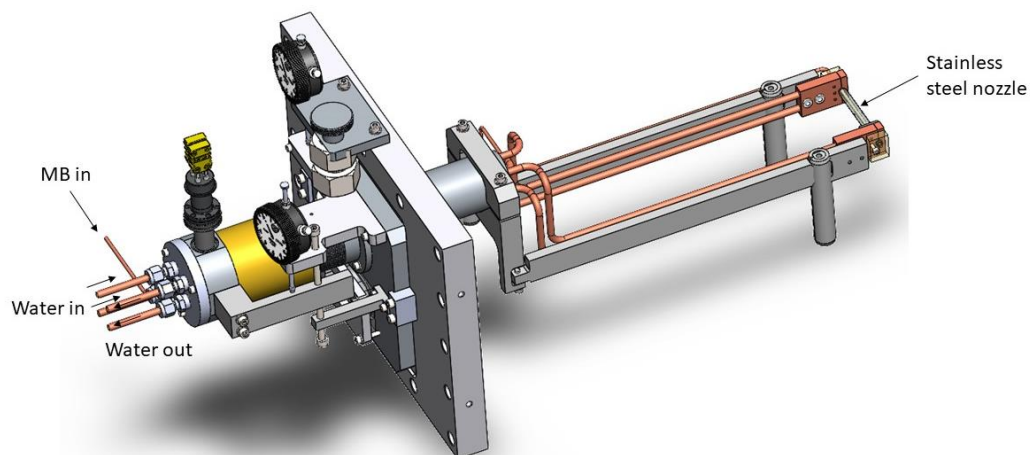


Fig. 2.4: 3D SolidWorks overview of the source and the cooling water flow direction in the copper tubes.

For the study of water dissociation on either a clean or an oxygen covered Cu(111) surface, I used a molecular beam of water molecules seeded in helium to collide with the metal surface. Since water exists as liquid at standard conditions (1 bar, 298 K), I mixed the helium carrier gas with the vapor pressure of water in a stainless steel reservoir containing typically 5 ml of D₂O (purchased from Eurisotop) to form a gas mixture of deuterated water molecules in helium. The reservoir or 'bubbler' is a stainless steel or glass container with one inlet, where the pure He gas enters and leaves through an exit, mixed with water molecules as shown in Fig. 2.5.

When the reservoir is first filled with D₂O, dissolved gases such as N₂, O₂, and CO₂ are removed through freeze-pump-thaw cycles. This process involves freezing the D₂O liquid using liquid nitrogen in polystyrene cups as shown in the photograph in Fig. 2.5, followed by pumping out any gas in the volume above the frozen liquid. The reduced pressure above the D₂O lowers the solubility the dissolved gases which leave the solution when the D₂O ice melts. These gases can then be pumped away once the water is frozen again. Typically 5 freeze-pump-thaw cycles are performed until no pressure rise is observed upon pumping on the ice indicating pure D₂O liquid.

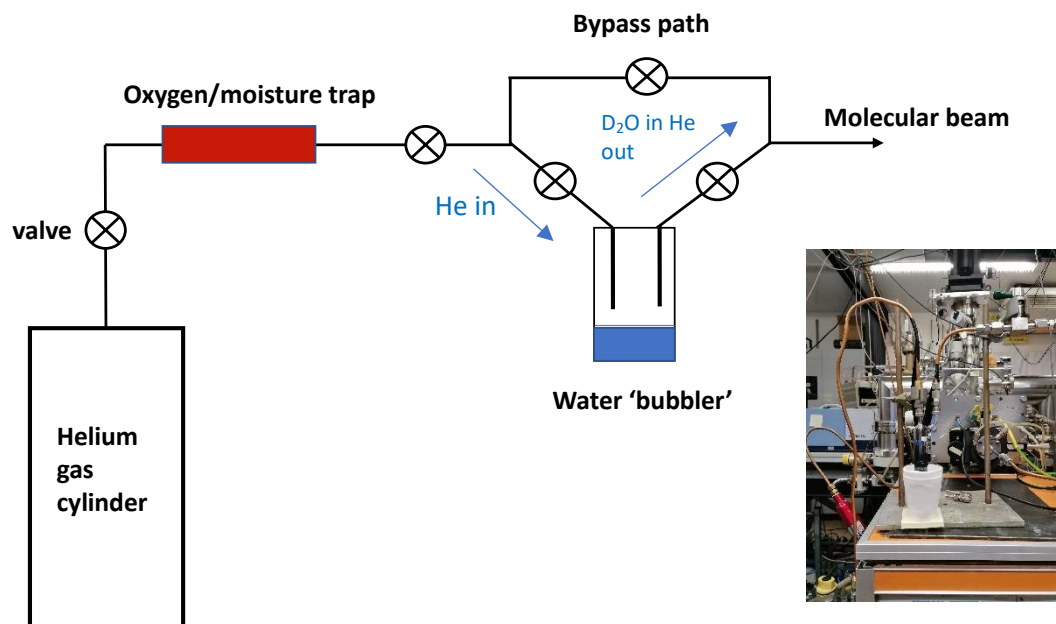


Fig. 2.5: Schematic diagram showing the paths that the molecular beam could travel in, either through the bypass or through the water 'bubbler'. Photograph showing a 'bubbler' made of glass placed in polystyrene cups during the freeze-pump-thaw cycle.

Copper undergoes oxidation very easily, therefore it is crucial to confirm the molecular beam is free of oxygen. By doing so, we prevent oxygen contamination on the copper surface which could significantly reduce the activation barrier for water dissociation and cause misinterpretation of the measurements. I used an oxygen/moisture trap (Supelco, Supelpure), installed before the 'bubbler' to remove any water molecules and/or oxygen molecules in the helium gas. The trap has catalyst coated on a molecular sieve which helps in the removal of water molecules and oxygen to less than 2ppb. Apart from using the trap, I also kept the gas line pressurized with He, above 1 bar, when no experiments were performed in order to prevent any small leaks into the gas line which could introduce oxygen contamination in the molecular beam.

The seed ratio of the D_2O molecules in He was controlled by heating the water reservoir at constant He gas pressure at 1 bar. Heating the 'bubbler' caused the vapour pressure of water in the reservoir to increase which then resulted in an increased seed ratio of deuterated water molecules in He. A plot of the seed ratio of D_2O in He at 1 bar as function of the reservoir temperature is shown in Fig. 2.6 below.

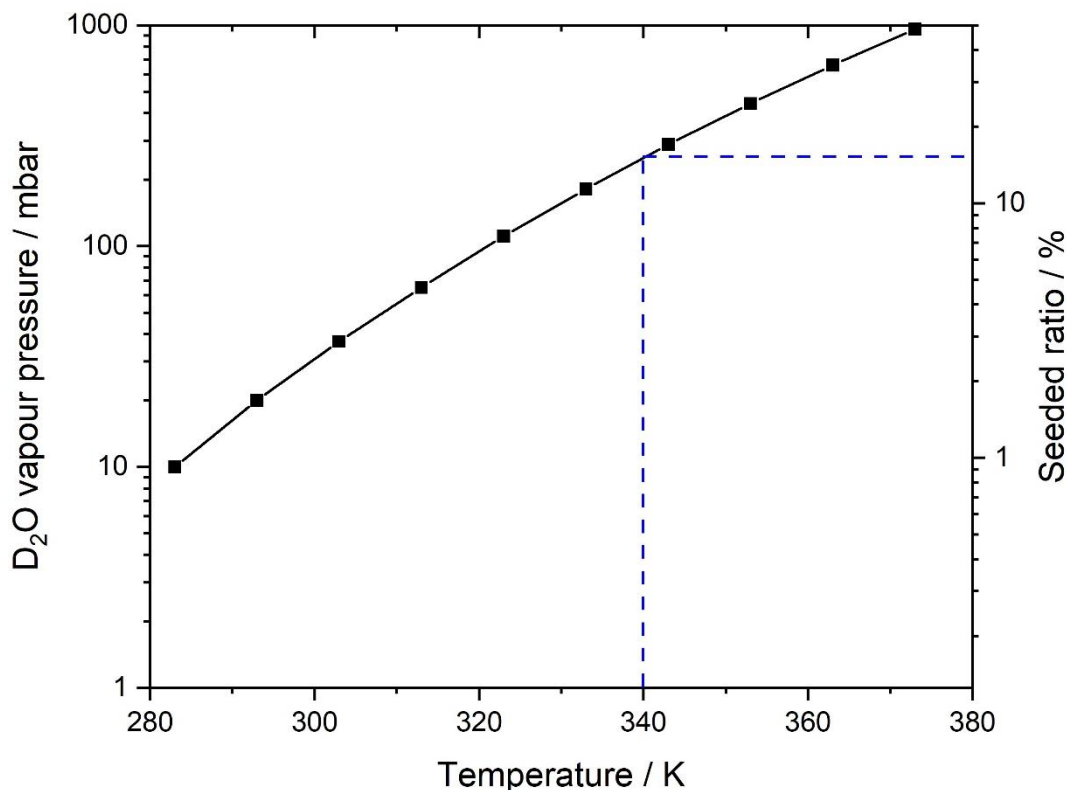


Fig. 2.6: Seed ratio of D₂O in He as a function of liquid water temperature for He pressure of 1 bar. The D₂O vapour pressure values are taken from the work of Matsunaga et al.⁴⁶

When the water reservoir was heated to increase the seed ratio, the gas line leading to the nozzle also needed heating to ensure that there are no cold spots where the deuterated water molecules could condense. A heating tape was wrapped around the copper tube leading from the reservoir to the vacuum feedthrough and the 1/8" copper tube inside the machine was heated by passing a DC current of 14 A through it.

For the preparation of the molecular beam of methane in He a commercially available 3% CH₄ in He mixture (with CH₄ purity of 99.9995%) from Carbagas was supplied to the molecular beam source via the oxygen/moisture trap.

2.2.3 Sample preparation

Two different single crystal surfaces were investigated as part of this thesis research, the flat Cu(111) surface and a stepped Pt(211) surface. The former was used for the study of D₂O dissociation whereas the latter was used to study methylidyne co-adsorbed with

hydrogen atoms on the surface. The Cu(111) surface is susceptible to oxidation therefore, it was a challenge to ensure there was no oxidation occurring when the surface was not deliberately introduced to oxygen. As explained previously in section 2.2.2, any air leaks into the gas line was prevented by keeping the copper line under helium pressure when there are no experiments running.



Fig. 2.7: A Cu(111) surface held in between two tungsten wires, used for surface heating and cooling.

The Cu(111) was cleaned by sputtering with Ar^+ at 1 kV and 2 μA with $1 \cdot 10^{-7}$ mbar argon pressure in the UHV chamber, for 15 minutes. After that, the surface was annealed at $T_s = 900$ K for 10 minutes^{47,48}. The cleanliness of the surface was then verified with Auger Electron Spectroscopy (AES) measurement, Fig. 2.8 - top.

The Pt(211) surface was cleaned by sputtering with Ar^+ at 1 kV and 2 μA with $1 \cdot 10^{-7}$ mbar argon pressure in the UHV chamber, for 10 minutes. Following that, the Pt(211) surface was annealed at $T_s = 1100$ K for 2 minutes⁴⁹. Surface cleanliness was verified by taking an AES measurement, Fig. 2.8 - bottom. In addition to sputtering and annealing, between experiments (on the same day), the Pt(211) surface was cleaned by exposing it to $5 \cdot 10^{-8}$ mbar of O_2 pressure in the UHV chamber at $T_s = 700$ K. This allowed for carbon contamination from previous surface exposure to methane molecules, to be oxidised and removed as CO and CO_2 .

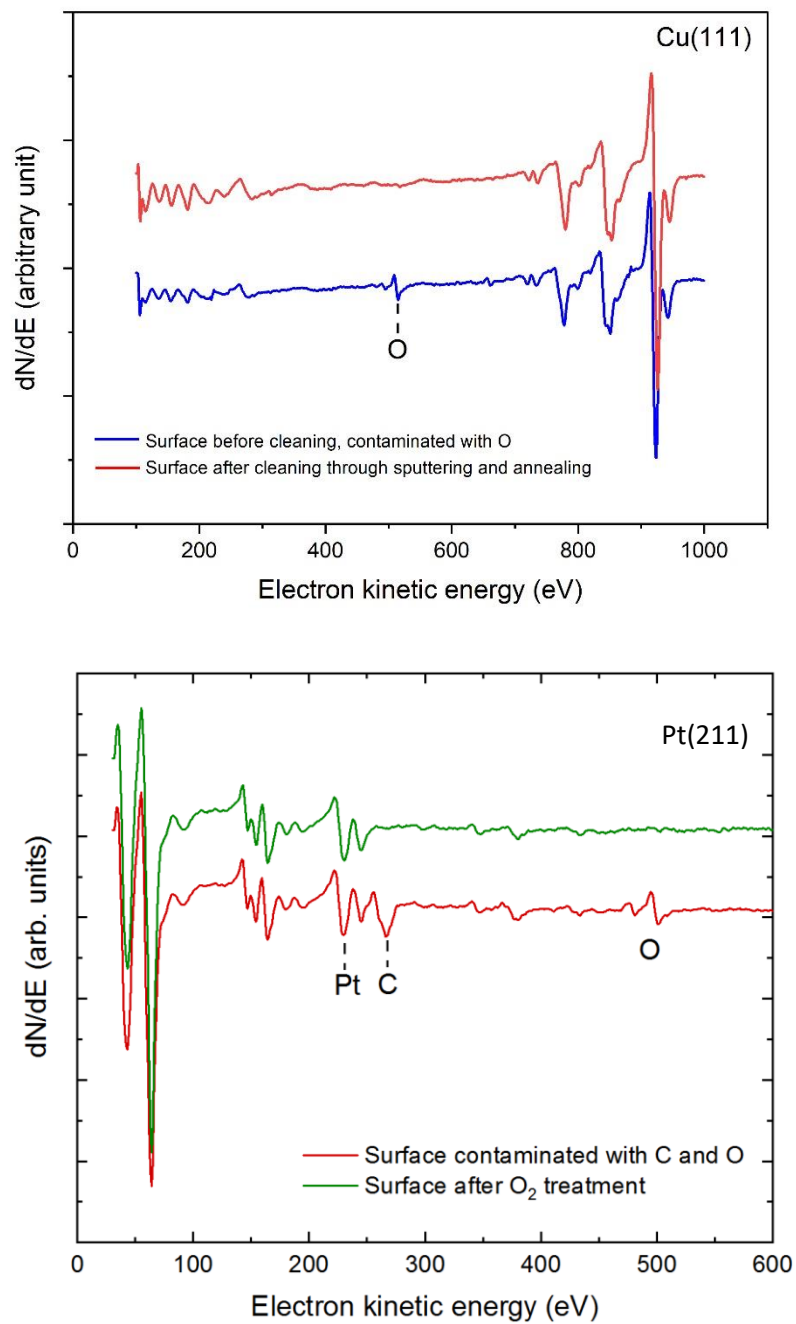


Fig. 2.8: Auger spectra showing measurements before and after cleaning the Cu(111) surface-top and Pt(211) surface- bottom. The bottom figure was reproduced from⁴².

2.2.4 Molecular beam flux

The sticking coefficients of molecules on the surface can be measured by the K&W beam reflectivity method. The sensitivity of this technique is limited by the signal/noise ratio of the QMS system used to monitor the partial pressure of the sample gas in the UHV chamber which in the RAIRS machine is of the order of 1% with a 1 sec integration time. For water dissociation on a clean Cu(111) surface, the expected sticking coefficients for our conditions of incident energy are expected to be much lower than 1% due to the high activation barrier for this reaction, predicted by DFT calculations to be 1.5 eV⁵⁰.

Therefore, a more sensitive method is needed to perform sticking coefficient measurements. Reflection Absorption Infrared Spectroscopy (RAIRS) is a highly sensitive method of infrared spectroscopy for the detection of adsorbates with dipole active vibrational modes. We used RAIRS to monitor the uptake of chemisorbed OH of the dissociative chemisorption of water. The coverage dependent sticking coefficient $S(\theta)$ can be calculated from the slope of the uptake curve of the product species which relates the coverage of the absorbed species to the incident dose of the reactant molecule.

The incident dose (in ML) is calculated from the molecular beam flux density (molecules/(sec*cm²)) incident on the target surface, given by

$$Flux\ density = \frac{\Delta P \cdot S}{k_B \cdot T_g \cdot A} \quad (2.3)$$

where the ΔP is the rise in the partial D₂O pressure in the UHV chamber upon admission of the gas molecules into the chamber, S is the pumping speed of the turbo pump in the UHV chamber for D₂O, k_B is the Boltzmann constant, T_g is the temperature of the gas in the UHV chamber (298 K) and A is the cross sectional area of the molecular beam on the surface.

The partial pressure rise of D₂O at $m/z=20$ was monitored by the off-axis QMS installed in the RAIRS machine (Pfeiffer, QMA 400, QMH 400-5 and QMG 422). The QMS signal was then converted to partial pressure of D₂O using an experimentally determined calibration factor. The QMS calibration involved leaking in a known partial pressure of water vapour (H₂O) as measured by a cold cathode gauge, into the UHV chamber from a reservoir attached to the UHV gas line while monitoring the QMS signal for m/z 18 with 1400 V SEM voltage and

1.5 μA emission current. The QMS measurements and the cold cathode gauge readings (corrected with ionization efficiency of H_2O - 1.12) were recorded for four different H_2O pressure rises in the UHV chamber as shown in Fig. 2.9. The conversion factor was obtained from a linear regression of the QMS signal (in Amperes) to H_2O partial pressure rise (in mbar) obtained from this measurement is $1.1 \text{ mbar A}^{-1} \pm 5.8\%$. (In this calibration, it was assumed that H_2O and D_2O have the same gas correction factors.)

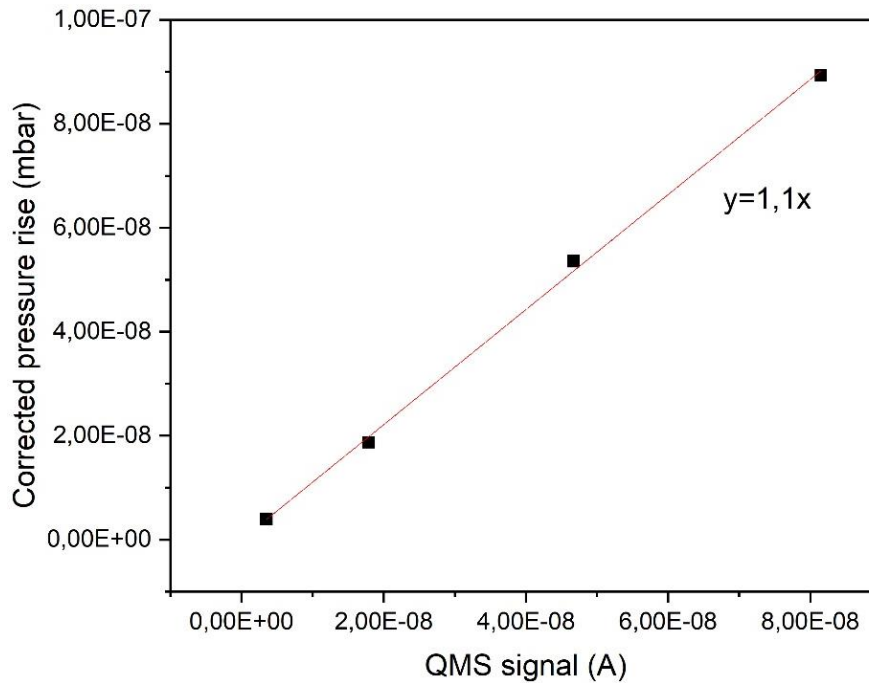


Fig. 2.9: Calibration of the QMS signal to the partial pressure of the H_2O in the UHV chamber.

During my thesis research, the turbo pump on the UHV chamber was changed from Pfeiffer TMU 1001 with 920 L/s of pumping speed to a Maglev Turbomolecular pump STP 1003 from Edwards Vacuum with pumping speed of 1000 L/s for N_2 . A protecting mesh with a conductance of 3051 L/s was installed above the STP 1003 pump resulting in a pumping speed of 753 L/s, calculated as,

$$\text{Total pumping speed of turbo in UHV} = \left(\frac{1}{S_{\text{pump}}} + \frac{1}{S_{\text{grid}}} \right)^{-1} \quad (2.4)$$

Details on the pump models and the pumping speeds of other pumps used in this gas/surface apparatus can be found in Ana Gutiérrez-González's thesis ⁴².

Since water molecules will trap on cold surfaces, we need to take into account the pumping speed of the liquid nitrogen cooled sample mount. This cryogenic pumping speed was measured by recording the D_2O QMS signal both with and without liquid nitrogen in the cryostat of the sample mount. The resulting QMS trace is shown in Fig. 2.10. Without liquid nitrogen cooling, the rise A in the QMS signal for m/z 20 was observed when the separation valve was opened. The QMS signal is seen to increase slowly due to trapping of D_2O on the inner walls of the UHV chamber. The same measurement was then repeated but with the cryostat of the sample mount halfway (B) and completely filled (C) with liquid nitrogen in order to test to see if the cryogenic pumping depends on the level of the liq. N_2 in the cryostat. Fig. 2.10 shows that there is no difference.

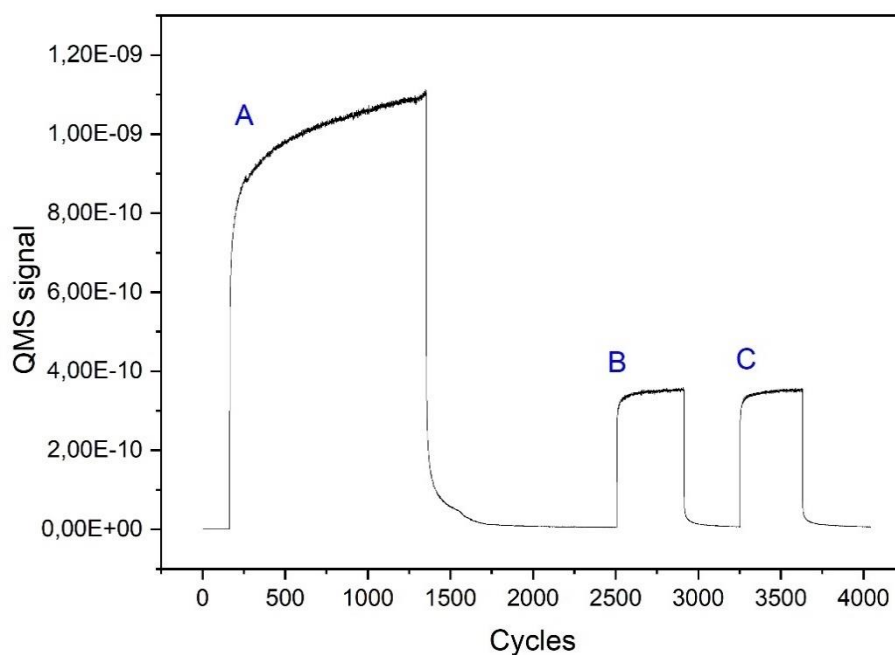


Fig. 2.10: QMS signal measured for, A – The Cu(111) surface at $T_s = 300$ K without any liquid nitrogen cooling. At $T_s = 180$ K with the sample mount B- half-filled and C- fully filled with liquid nitrogen.

Comparing the QMS signal of A to B and C, it is clear that the surface mount cooling increases the pumping of the D_2O molecules in the UHV chamber. Since the QMS signal is directly proportional to the partial pressure of D_2O in the UHV chamber, the drop in the D_2O pressure due the secondary cryogenic pump can be obtained from the ratio of the maximum

QMS signal from curve A and B shown in Fig. 2.10, calculated as 3.14. Including the cryogenic pumping speed yields a total pumping speed in the UHV chamber of 2364 L/s.

$$S_{total} = 753 \frac{L}{s} \cdot 3.14 \quad (2.5)$$

The dose of molecules arriving on the surface per unit time is then calculated by:

$$Dose = Flux \cdot Time \quad (2.6)$$

During my experiments I used a flux of 0.03 ML s^{-1} for D_2O molecules. If the sticking coefficient of D_2O on Cu(111) is assumed to be 1, then it takes about 33 seconds to form a ML of D_2O on the surface.

As mentioned above, the coverage dependent sticking coefficient for a gas/surface reaction can be obtained from the uptake curve of the product detected by RAIRS. In order to do so, we need to know the incident dose of reactant molecules and the resulting coverage of the F_{product} species. We also need to be sure that the adsorbed product species are stable on target surface and that the RAIRS signal is a linear function of the coverage. In this section, I have explained how the dose of water molecules was calculated. In the Auger Electron Spectroscopy (AES) section, I will describe the method used to calibrate the RAIRS signal in terms of coverage of a nascent product on the surface.

2.2.5 Gas-surface detection techniques

2.2.5.1 Auger Electron Spectroscopy (AES)

Auger Electron Spectroscopy is a widely used elemental analysis for metal surfaces in UHV. It involves the exposure of a surface to a stream of high energy primary electrons (in this case, 3 kV of energy was used) which causes the removal of a core electron from the atoms on the top layers of a surface. A vacancy is therefore formed in the core electron level, K which gets filled in by an electron from a higher energy level, L. The excess energy released from this phenomenon is then used to remove another electron from the outer shell, M known as the *Auger* electron. The ejected *Auger* electrons are collected by a cylindrical mirror analyser (CMA from Perkin Elmer) filtered according to their kinetic energies and detected by

an electron multiplier. The Auger electron spectrum obtained shows the characteristic Auger peaks for the different elements present on the sample. Thus, quantitative analysis of the spectra will provide information such as the surface composition and the surface coverage of a certain adsorbate.

In my study, I used AES to verify the surface cleanliness as discussed in the sample preparation section, 2.2.4 and to quantitatively analyse the Cu(111) surface after intentionally exposing it to different doses of O_2 , leaked into the UHV chamber to study the interaction of H_2O on an oxygen covered Cu(111) surface. This was done by detecting oxygen at 520 eV and copper at the strongest Auger signal at 920 eV as shown in Fig. 2.11. The feature at 283 eV is attributed to electron scattering and is not due to carbon contamination⁵¹.

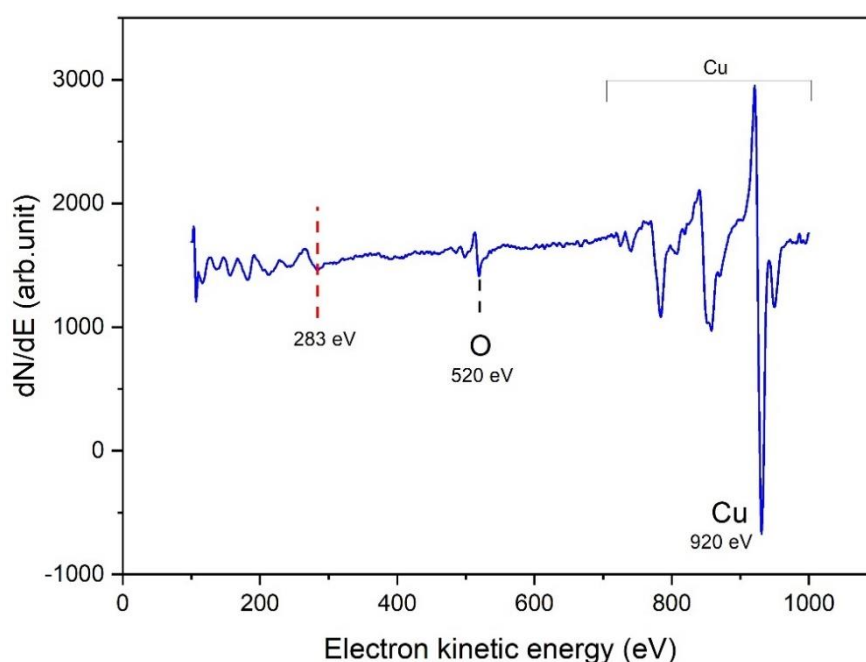


Fig. 2.11: Auger spectra showing the O and Cu peaks used for determining oxygen coverage on the surface.

One of my studies involved confirming the reaction mechanism of D_2O gas molecules on a partially oxygen covered Cu(111). In order to do this, after O_2 exposure to the surface, I moved the Cu(111) in front of the Auger electron gun and bombarded it with high energy electrons, 3 kV.

Oxygen molecules on Cu surfaces are known to be prone to electron stimulated adsorption therefore, during the AES measurements any oxygen adsorption arising from this process would cause an overestimation of the surface oxygen coverage. To overcome this problem, I adopted a method to measure the Auger spectra which accounts for this process⁵². After the Cu(111) surface was exposed to O₂(g), I measured six consecutive AES measurements with 2 sweeps each, on the same surface position and then plotted the O/Cu peak-to-peak AES signal ratio. The result is shown Fig. 2.12. It is clear that the O/Cu ratio increases with every measurement, indicating the increasing effect of electron stimulated oxygen adsorption on the surface. Here, it is also important to note that prolonged surface exposure to Auger electron gun is known to deposit significant amount of contaminants such as O on the metal under study⁵³. Assuming the rate of both these processes are constant from one measurement to another, the O/Cu Auger peak-to-peak ratio without the effects of electron induced oxygen adsorption and Auger electron gun contamination is the y-intercept of the best fit line shown in Fig. 2.12.

The Auger peak-to-peak ratios obtained following different oxygen surface coverage are then compared to a known 0.5 ML oxygen coverage for the ordered “29” superstructure of Cu₂O⁵⁴. This is explained in Chapter 4.

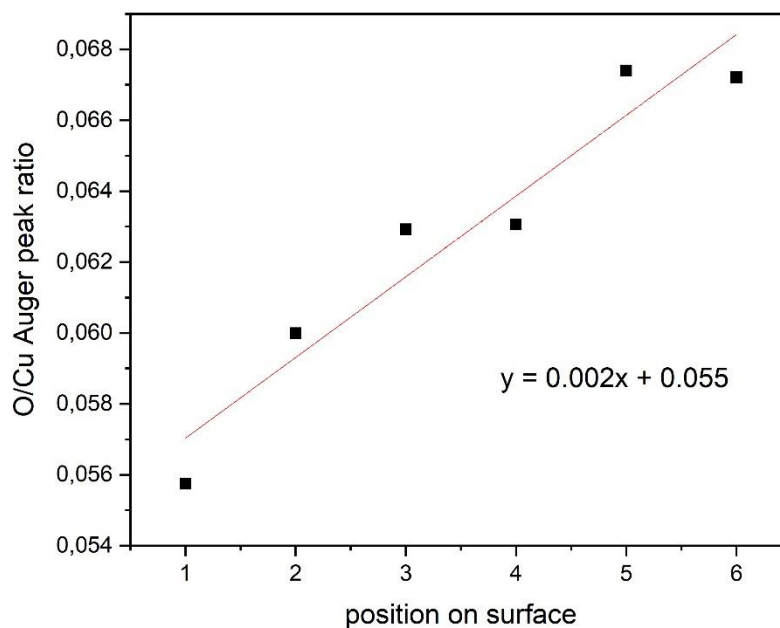


Fig. 2.12: O:Cu peak ratio following Auger measurements performed at the same position on the surface, after the Cu(111) surface was exposed to 200 L of O_2 at $T_s = 300$ K.

2.2.5.2 Temperature Programmed Desorption (TPD)

Another common technique employed in surface science studies is the temperature programmed desorption (TPD) method. TPD is performed after gas/surface reaction where the incoming MB is no longer incident on the surface. Controlled surface heating is conducted while simultaneously measuring the partial pressure of the species desorbing from the surface using a quadrupole mass spectrometer (QMS). In my studies, the off-axis QMS was used to record the signal for the different masses of molecules desorbing from the surface. Based on the desorption temperatures of the different species, one can obtain information on the binding energy of the adsorbates, different adsorption sites of a chemical species on the surface, the reaction order for a desorption process, coverage of a certain adsorbate species and even the isotopic exchange occurring on the surface⁵⁵. For my study, I used the TPD measurements to identify surface adsorbates following D_2O gas molecules reaction with the Cu(111) surface.

2.2.5.3 King and Wells (K&W)

The King and Wells molecular beam reflectivity technique is used to measure the sticking probability, S_0 of a reactant on a surface. The K&W traces are obtained by using the off-axis QMS coupled with the separation valve and the mica flag in the UHV chamber. The MB entering the UHV chamber is initially blocked by the flag in order to prevent it from directly striking the surface and the partial pressure rise due to the MB being reflected off the flag is measured, P . Upon removal of the flag, the molecular beam collides directly with the surface. Any molecules that stick to the surface will result in a drop in partial pressure and a drop in the QMS signal. The relative change in QMS signal yields a self-calibrated measurement of the sticking. The K&W method is not able to distinguish between physisorption, chemisorption or dissociative chemisorption of a reagent. Therefore, one needs to be careful of the possible misinterpretations of the sticking coefficients obtained from the K&W technique.

In this thesis, I used the King and Wells (K&W) method to identify the fraction of the molecular beam (MB) which actually strikes the 10 mm diameter Cu(111) surface. For this, a molecular beam of D_2O was sent into the UHV chamber with the K&W flag blocking the MB while recording the rise in the QMS signal (labelled as P in Fig. 2.13) for m/z 20 (2% D_2O in He mixture) at $T_s=90$ K. When the K&W flag was removed, the molecular beam impinged partially on the cold Cu(111) surface covering it with a layer of ice. It is known that the water molecules stick with unit probability on ice⁵⁶. The partial pressure drop resulting from the removal of the K&W flag from the MB is labelled as ΔP . The ratio $\Delta P/P$ corresponds to the fraction of the molecular beam striking on the cold Cu(111) surface. From Fig. 2.13 below, we determined $\Delta P/P = 0.94 \pm 3\%$. Hence, according to the data shown in Fig. 2.13, only 94 % of the water in the MB arrives on the surface as the MB size is larger than the diameter of the surface. The MB size was not reduced further as this requires the nozzle to be retracted further from the skimmer which reduces the beam intensity in the UHV chamber.

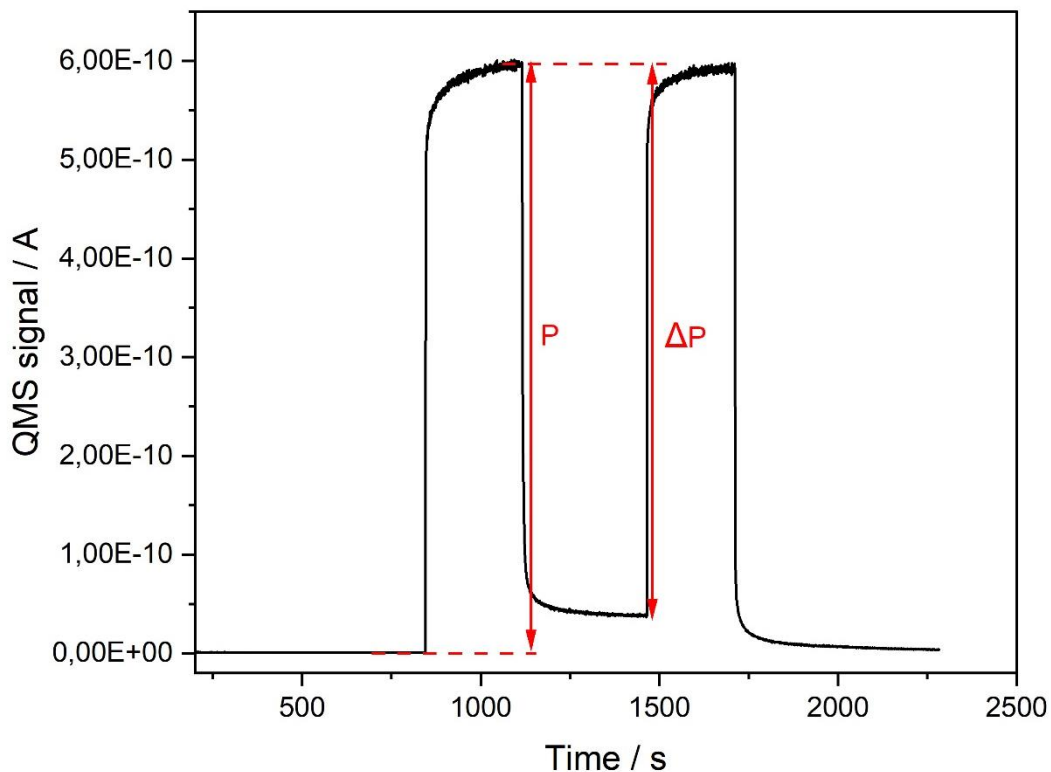


Fig. 2.13: King and Wells trace at m/z 20 to measure the flux of D_2O impinging on a cold Cu(111) surface covered with a layer of ice, $T_s = 90$ K.

2.2.5.4 Hydrogen Atom Beam Source (HABS)

During my thesis research, a hydrogen atom beam source (HABS) was installed in our UHV chamber. H-atoms are produced by flowing H_2 gas through a hot tungsten capillary which was heated using tungsten filament wrapped around it. The filament was heated using a direct current which in turn by conductance, heats up the capillary. This capillary can be heated up to 2100 °C to result in thermal cracking of the H_2 molecules in the capillary (cracking efficiency: 80 - 98%). Water cooling is used to remove heat from the copper cooling shroud which houses the heating filament and cracking capillary, shown in Fig. 2.14

For my experiments, I used HABS to create hydrogen atoms to hydrogenate the oxygen atoms on the Cu(111) surface when investigating the water reaction on an oxidised Cu(111) surface. To do so, I leaked in H_2 molecules from a reservoir attached to the HABS into the tungsten cracking capillary which was heated to 1600 °C resulting in the dissociation of H_2 molecules into H atoms.

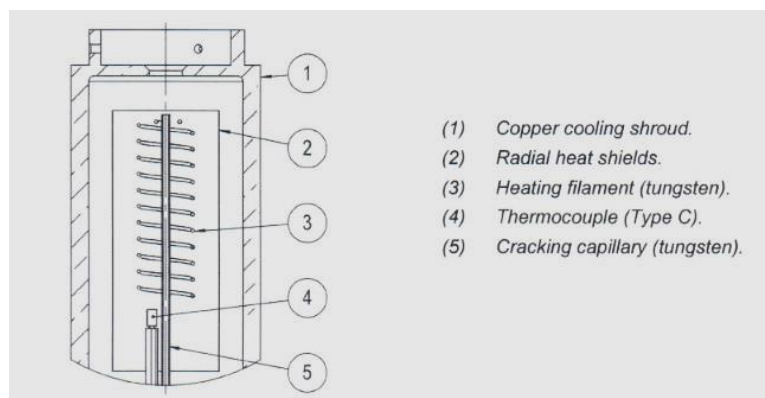


Fig. 2.14: The heating structure of the hydrogen atom beam source. Taken from the manual of HABS.

2.2.5.5 Reflection Absorption Infrared Spectroscopy (RAIRS)

During my research, I have extensively used the Reflection Absorption Infrared Spectroscopy (RAIRS), an optical technique used widely in surface science studies, to probe the adsorbates on metal surfaces. I used this technique to identify the nascent products of water molecules interacting with Cu(111) surface and methane molecules reactivity with Pt(211) surface. One main advantage of using RAIRS is that it is a non-invasive method unlike AES. The electron beam used in AES changes the reactivity of the incoming molecules by causing dissociation in the MB therefore, one cannot monitor the gas/surface reaction in real time. Instead, RAIRS enables one to measure the vibrational absorption spectra in real time without interfering with the reaction. Previously, it was also demonstrated by Ana Gutiérrez González, a Ph.D. student from our lab how RAIRS is a sensitive tool for studying site-selective dissociation of methane on Pt surfaces ⁴².

Our RAIRS apparatus, combines a commercially available FTIR spectrometer (VERTEX 70V from Bruker) with an external detector with a home built UHV chamber and a molecular beam source (purchased from Thermonics)⁴¹. Infrared light is produced by a globar source (or a tungsten lamp for NIR) which is incident on the surface at a grazing angle of $\sim 80^\circ$. The metal surface placed in the UHV chamber reflects this light to an indium antimonide (InSb) detector, placed in the detector box as shown in Fig. 2.15. A PC software control, OPUS was provided by Bruker for the parameters control and data collection.

During the scanning of the movable mirror in the interferometer, a Fourier transformed single channel IR spectrum is generated by OPUS from the interferogram measured. The RAIRS spectra shown in this thesis are calculated as the ratio between the two single channel spectra of the surface, (i) covered with adsorbates and (ii) a clean surface. More details on the FTIR VERTEX 70V spectrometer can be found in Li Chen's thesis ⁴⁰.

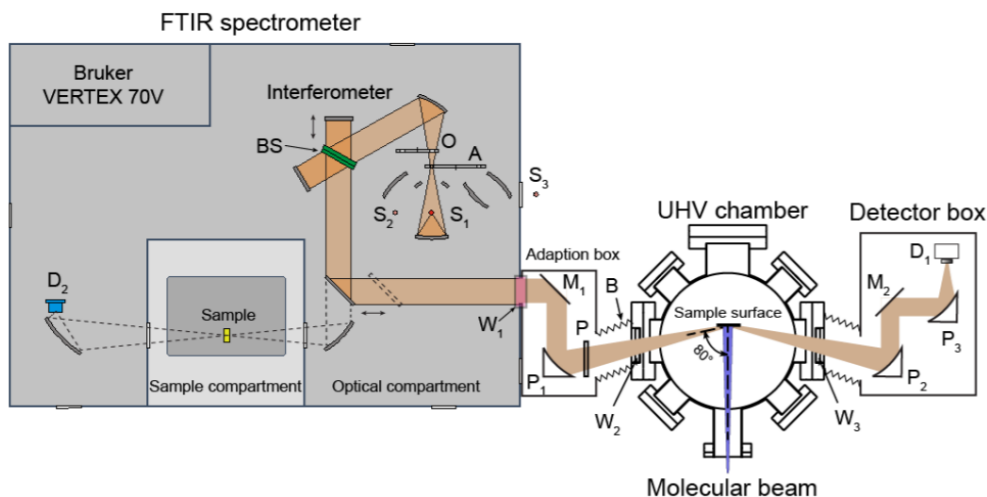


Fig. 2.15: The gas/surface apparatus highlighting the path of the IR light travelling from the source and arriving on the surface at a grazing angle followed by its reflection into a detector.

The surface selection rule for the RAIR spectroscopy requires the adsorbates to possess a component of dynamic dipole moment perpendicular to the surface. This is because when IR light is incident on a metal surface at grazing angle, the s-polarized light (electric field is perpendicular to the plane of incidence) reflects from the surface with a zero net electric field meanwhile the p-polarized light (electric field is parallel to the plane of incidence) reflects with an enhanced electric field, Fig. 2.16. As the electric vector of the s-polarized light is cancelled on the surface, only the p-polarized light interaction with the surface adsorbates is detected.

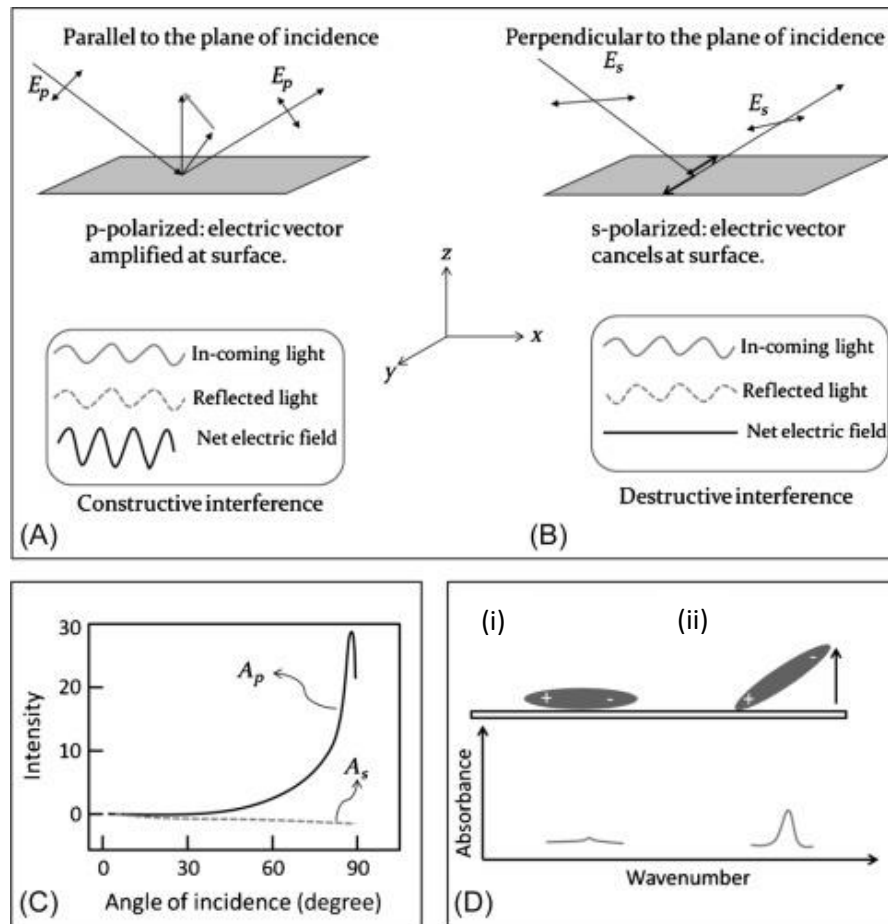


Fig. 2.16: (A)- The incident *p*-polarised electric field on the surface has a positive net electric field upon reflection meanwhile in (B)- incoming *s*-polarised electric field vector cancels out at the surface. (C)- A plot showing intensity of RAIRS signal with changing incident angle of the *p*- and *s*-polarised light. (D)- The different RAIRS peak intensity observed for the same molecule when it (i) lies flat or (ii) tilted on the surface. Reproduced with permission from ⁵⁷.

Apart from the electric field, the image dipole of the adsorbates formed on the reflective metal surface can help one to understand the RAIRS selection rule. An oppositely charged image induced in the metal substrate by an adsorbate is referred to as the image dipole. For instance, in Fig. 2.17 when an adsorbate lies flat on the surface with the axis of dipole moment parallel to the surface, the image dipole created on the surface cancels out. However, if the dipole moment of the adsorbate is perpendicular to the surface, then the image dipole helps to increase the total dipole moment. In short, to observe an absorption feature in the RAIR spectra, there must be a changing dipole moment of the adsorbates normal to the surface.

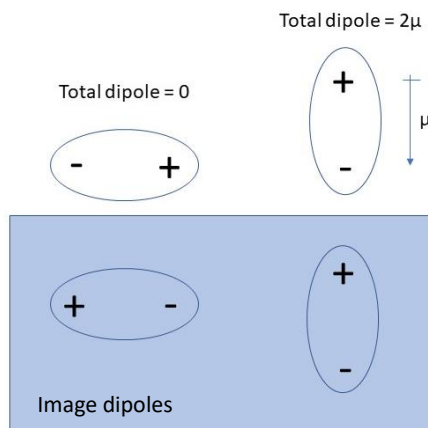


Fig. 2.17: Image dipoles formed in the metal surface based on the different orientations of the surface adsorbates.

2.3 Quantum-state preparation of the molecular beam

Another part of my study involves using a mid-infrared coherent light source to prepare the incident water molecules in a specific ro-vibrational state before their arrival on the Cu(111) surface. In order to do so, I used the commercially available tunable, single mode, continuous-wave optical parametric oscillator (OPO) purchased from the Lockheed Martin Aculight Corporation and crossed the laser beam normal to the molecular beam in the source chamber.

2.3.1 Optical Parametric Oscillator (OPO)

A non-linear crystal in the OPO converts an input ‘pump’ laser wave into two electromagnetic waves with lower frequencies called the ‘idler’ and the ‘signal’, through a second order non-linear process. The ‘signal’ is the frequency that is resonant in the OPO cavity for a singly resonant cavity and it is also the higher frequency of the two split frequencies. Based on the law of conservation of energy, the summation of the ‘idler’ and ‘signal’ frequencies should be equal to the frequency of the ‘pump’ wave. The phase match of the lower frequency waves is another requirement for the OPO operation.

$$\omega_{idler} + \omega_{signal} = \omega_{pump} \quad (2.7)$$

I used the Argos 2400 cw OPO C module for my experiments and it operates with a tuning range of 2564-3125 cm^{-1} which covers the antisymmetric, ν_3 vibrational mode of the D_2O molecules used in this thesis. The wide range frequency tuning of the OPO is a major advantage of this system on top of the high IR output power which is above 1 W across the specified tuning range.

Fig. 2.18 below shows a schematic diagram of the laser system, where the top box depicts the pump laser and the bottom box shows the OPO module. In the pump source, there is a distributed feedback (DFB) Yb-doped optical fiber laser operating at 1064 nm. It has a bandwidth of <100 kHz and seeds a 20 W fiber amplifier from IPG Photonics. The pump light arrives in the OPO cavity after travelling through the armoured fiber cable.

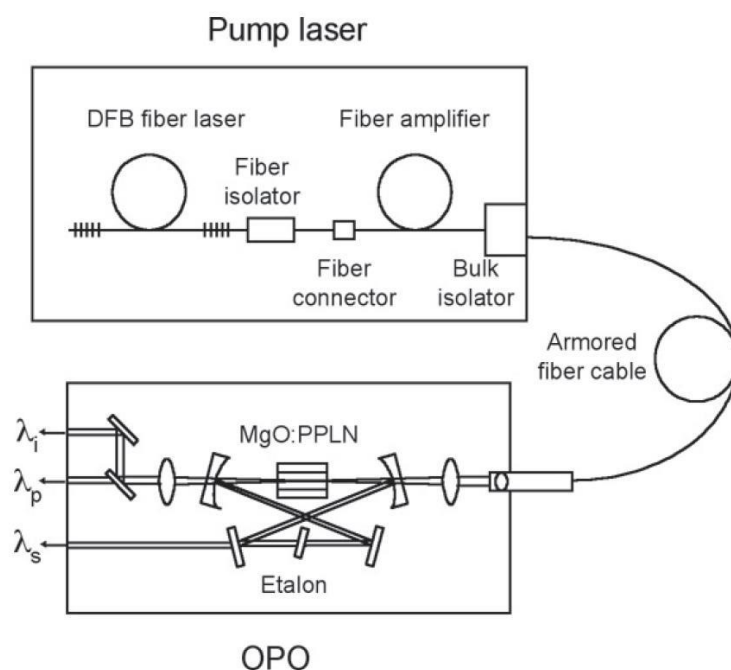


Fig. 2.18: A schematic diagram of the Aculight Argos 2400 showing the idler (λ_i), pump (λ_p), and signal (λ_s) wavelengths.

The OPO module is made of a nonlinear optical crystal which in our case is a periodically poled lithium niobate crystal (PPLN) placed in an optical resonator. As mentioned previously, only the signal wave is resonant in the OPO cavity whereas the idler wave leaves the OPO after a single pass. It is crucial that all the three electromagnetic waves, idler, signal and pump are phase matched (i.e. have fixed relative phase as they travel through the crystal)

for efficient generation of photons. If no fixed relative phase exists between the input and generated photons through the crystal, then the output photons will interfere destructively resulting in low number of photons generated following the parametric process. Fixed relative phase was achieved in our OPO through the PPLN, a crystal that allows for quasi-phase matching of the photons. This quasi-phase match is achieved as a result of periodic poling of the crystal. Furthermore, the periodic poling is designed in a 'fan-out' pattern that changes the poling period across the crystal therefore enabling one to tune the frequency of the generated photons when translating the crystal.

In my experiments, I used the idler wave to excite the water molecules to a specific ro-vibrational state. To ensure that the idler frequency matched the wavelength of the desired ro-vibrational state, I used three steps to tune the wavelength of the OPO output signal. They are the coarse ($\sim 13 \text{ cm}^{-1}$), intermediate ($\sim 1 \text{ cm}^{-1}$) and fine tuning (**continuous tuning over $\sim 3.3 \text{ cm}^{-1}$**).

- Coarse tuning: By translating the non-linear crystal one can change its poling period. As a consequence, different combinations of frequencies would achieve phase matching allowing one to move closer to the desired frequency.
- Intermediate tuning: Achieved by changing the angle of the intra-cavity Fabry-Perot etalon.
- Fine tuning: By applying a voltage (0-150 V) to the piezo electric element (PZT), the DFB seed laser experiences a strain which results in a frequency change in the pump laser. As a result of that, the idler frequency also varies over a range of **$\sim 100 \text{ GHz}$** .

2.3.2 Frequency stabilization with Lamb Dip locking

We require the IR excitation frequency to be stable (within 1 MHz) from minutes to hours during experiments. If left without any active stabilization, the OPO output was found to drift with time – a few MHz in minutes and hundreds of MHz in hours³¹. The drift arises due to the temperature or pressure variations in the laboratory. To overcome this problem, I

used the saturation technique (Lamb dip technique) to lock the laser in the desired IR transition frequency.

To use this technique, an absorption cell was filled with the gas molecules to be excited in the molecular beam. In this case, I used 80 μ bar of D₂O in the absorption cell. A fraction of the OPO output (idler) was directed into the absorption cell, \sim 130 mW. As the laser passes through the cell, it will excite the D₂O molecules in the path and result in a Doppler broadened absorption. The linewidth of a Doppler broadened signal for D₂O at room temperature is 231 MHz and stabilising the laser to the maximum of this line will not give the accurate transition frequency. Therefore, we require a Doppler-free absorption which can be reliably locked to. To do so, the laser signal was retro-reflected from a gold mirror at the end of the absorption cell. Following the double pass of the laser in the cell, a saturation hole is burned in the centre of the Doppler broadened profile. This spectral feature is called the Lamb Dip named after the American physicist Willis Eugene Lamb.

Lamb dip frequency stabilisation can be explained in simple terms. When the laser detunes from the desired transition frequency (ω_0), the oppositely travelling laser beams will excite different sub-set of the D₂O molecules. For the incoming laser beam, the molecules with a velocity component, $v_x = (\omega_L - \omega_0)c/\omega_0$ in the direction of the laser beam will be excited. Meanwhile, for the counterpropagating beam the molecules with a velocity component of $v_x = -(\omega_L - \omega_0)c/\omega_0$ in the axis of the laser beam will be excited resulting in a Doppler broadened profile shown in Fig. 2.19. When $\omega_0 = \omega_L$, the molecules travelling perpendicular to the laser beam axis ($v_x = 0$) will be excited by both the laser beams, i.e. the incoming laser beam and the reflected beam interact with the same set of molecules. If the laser power is high enough, the transition saturation gives rise to a dip in the absorption profile as a result of the lower level population bleaching shown in Fig. 2.19. This reduction in the absorption signal is termed Lamb Dip and has a linewidth of 2-3 MHz⁵⁸. This width of the Lamb dip is due to homogenous broadening for instance, transit time broadening and power broadening.

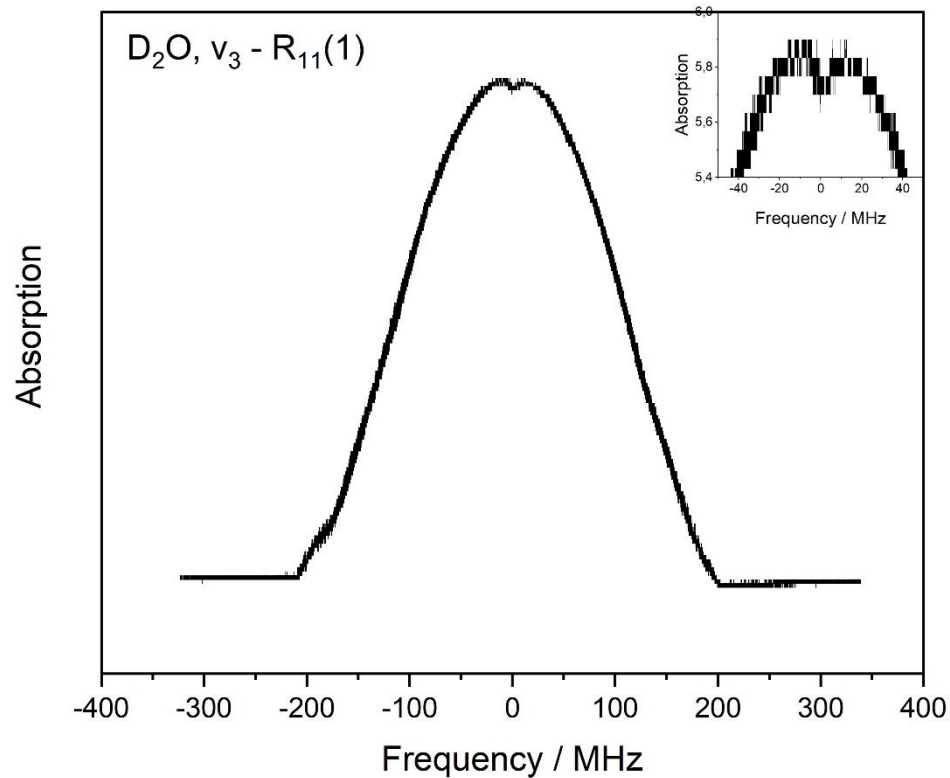


Fig. 2.19: Doppler broadened profile resulting from laser excitation and the Lamb dip formed (inset) as a consequence of laser exciting the same set of molecules twice.

In the machine, the molecular beam interacts with the laser at a normal angle. At this angle of interaction, the molecules travelling in the center of the beam have a zero-Doppler shifted absorption. Since the Lamb dip's frequency is the Doppler-free absorption frequency required to excite the molecules in the molecular beam, it is used to lock the laser at the desired transition frequency using a Laselok system.

Briefly, the OPO pump laser's frequency is modulated with a voltage sine wave sent by the Laselok to the seed piezoelectric element. Then, the photodiode measures the dithered signal on the absorption profile. The resulting lock-in signal (absorption signal \times modulated signal) is the first derivative of the Lamb dip where its zero crossing is the zero-Doppler shifted absorption frequency. When the measured frequency drifts from the zero-crossing, the Proportional-Integral-Differential (PID) controller generates a corrective signal which is sent to the seed piezoelectric element to restore the desired transition frequency hence closing the feedback loop and actively locking the OPO idler frequency.

2.3.3 Rapid Adiabatic Passage (RAP) for population inversion

To study the effect of vibrational energy for a gas/surface interaction, we prepare our molecules in a specific rovibrational state using the rapid adiabatic passage (RAP) technique coupled with a single mode, continuous wave IR laser. More details on the working principles of the RAP technique are explained in the work of Chadwick *et al.* and Bruce Yoder's dissertation^{59,58}. We are able to achieve complete population inversion for the excited molecules due to RAP. If not for this adiabatic technique, we would have only 50 % of the molecules in the excited state because of Rabi cycling, a cyclic behaviour between 2-level system. When a beam of photons interacts with the gas molecules in the molecular beam, the photons will be absorbed and the molecules will be excited to a higher energy quantum state. With more photon interaction, the molecules then re-emit the photons through stimulated emission and return to the lower energy level. This absorption and stimulated emission occur in a cyclic behaviour therefore, on average there will only be 50 % of the molecules in the higher energy level.

A more efficient population inversion can be achieved with RAP by introducing curved laser wavefronts using a cylindrical lens in the path of the laser. Due to the curved wavefronts, the molecules travelling across the laser will experience a linear sweep of frequencies (a Doppler tuning) resulting in a complete population inversion of the molecules⁵⁹.

2.3.4 Excited state population in the molecular beam

The state resolved sticking coefficient measurements of the water molecules on a Cu(111) surface requires one to know the fraction of excited of water molecules in the molecular beam prior to interaction with the surface. There are two methods to introduce vibrational energy in the incident molecules. One way is through heating the nozzle which causes the molecules to populate low-lying vibrational states and the other method involves the usage of a laser, where a resonant laser crosses the molecular beam while the molecules travel towards the surface. The percentage of excited molecules from the former method can be calculated using the partition function of water molecules explained in the following paragraph. Furthermore, fluence curve measurements are recorded to find the fraction of vibrationally excited molecules in the MB due to laser excitation. In the following paragraphs,

I will explain how both the methods were involved in the study of water dissociation on a clean Cu(111) surface.

Supersonic expansion is able to efficiently cool the rotational levels of the molecules in the molecular beam however, vibrational cooling is not as efficient⁶⁰. Thus, at higher nozzle temperatures some molecules can still remain in the excited vibrational states based on Boltzmann distribution. Using the partition function for water molecules,

$$q_{vib} = \prod (1 - e^{-\frac{h\nu_i}{kT}})^{-1} \quad (2.8)$$

I was able find the thermal population of each vibrational mode, P at different nozzle temperatures using the following formula,

$$P = \frac{e^{-n_i h\nu_i/kT}}{q_{vib}} \quad (2.9)$$

where i is the vibrational mode, n_i is the quantum number for mode i and ν_i is the frequency of mode i . Table 2 below shows the vibrational state population calculated.

Table 2: The fraction of D₂O molecules in different vibrational states for various T_n calculated using the formulae 2.8 and 2.9 above.

		Vibrational state population				ground state
		$\nu_1 = 1$	$\nu_2 = 1$	$\nu_2 = 2$	$\nu_3 = 1$	
T_n/K	E_{kin}/eV	2691.606 cm^{-1}	1190.790 cm^{-1}	2359.689 cm^{-1}	2799.758 cm^{-1}	
300	0.28	0	0.003	0	0	0.997
320	0.30	0	0.005	0	0	0.995
400	0.35	0	0.014	0	0	0.986
500	0.44	0	0.031	0.001	0	0.967
600	0.52	0.002	0.054	0.003	0.001	0.940
700	0.60	0.004	0.078	0.007	0.003	0.908
800	0.68	0.007	0.100	0.012	0.006	0.875
900	0.75	0.013	0.125	0.022	0.011	0.828
1000	0.82	0.020	0.146	0.032	0.017	0.784
1050	0.86	0.024	0.157	0.038	0.021	0.760

The excited state population can be obtained with fluence curves, plots of pyroelectric detector signal as a function of the excitation laser power. To perform fluence curve measurements, one needs to vary the laser power which was realised by rotating a $\lambda/2$ waveplate coupled with a linear polarizer. As the pyroelectric detector only measures a change in the temperature, the laser beam needs to be modulated. This was achieved by chopping the laser beam using an electromechanical shutter operating at 2 Hz and detecting the pyroelectric detector signal using a lock-in amplifier. The signal measured by the pyroelectric detector corresponds to the fraction of vibrationally excited molecules in the molecular beam. As the laser power increases, the pyroelectric signal also increases until it reaches a saturation which indicates a complete population inversion attained with RAP.

Considering the initial state population of the molecules as well as the laser excited molecules, one may determine the fraction of excited molecules in the continuous molecular beam, from the following relation.

$$f_{exc} = f_{rot} \cdot f_{vib} \cdot f_{RAP} \quad (2.10)$$

where f_{rot} refers to the fraction of molecules populating the lower rotational levels. As stated above, the rotational energy of the molecules is efficiently cooled during the supersonic expansion of the molecular beam in the nozzle therefore, it will not be accurate to take the temperature of the nozzle as the rotational temperature of the beam. The two methods outlined below are used in our lab to determine the rotational temperature of the gas molecules.

- In the first method, fluence curves for different transitions are recorded where each transition has several different initial J levels measurements. The asymptotes achieved by the different J levels are then compared for the same transition and the ratios are used to determine the relative rotational populations of the J levels. By comparing the experimentally obtained relative populations to the theoretical values at different rotational temperatures, one can identify the rotational temperature of the molecules. Further details of this method are explained by Li Chen in his thesis ⁴⁰.
- The second method uses the direct relation of the pyroelectric detector signal to the population of the excited molecules in the molecular beam (i.e. pyroelectric detector

signal \propto fraction of excited molecules in the beam). Based on this, we measure many fluence curves for transitions with different J levels from the same symmetry species. In this case, we have to record fluence curves for all the populated J levels. The sum of the asymptotes for the different J levels is equal to the theoretical fraction of molecules with this symmetry. For instance, ortho D_2O molecules have statistical weight of $2/3$ and para has $1/3$. By employing this method, we can obtain a direct calibration of the pyroelectric signal to the fraction of excited molecules.

The f_{vib} refers to the fraction of vibrationally excited molecules which was previously shown to be calculated from the partition function of water molecules. This leaves us with the f_{RAP} term which refers to the excitation efficiency using the RAP technique which can be obtained from the fluence curves measured. The ratio of the pyroelectric detector signal at a certain laser power compared to the asymptote of the pyroelectric detector signal gives the information of the fraction of molecules in an excited state, f_{RAP} .

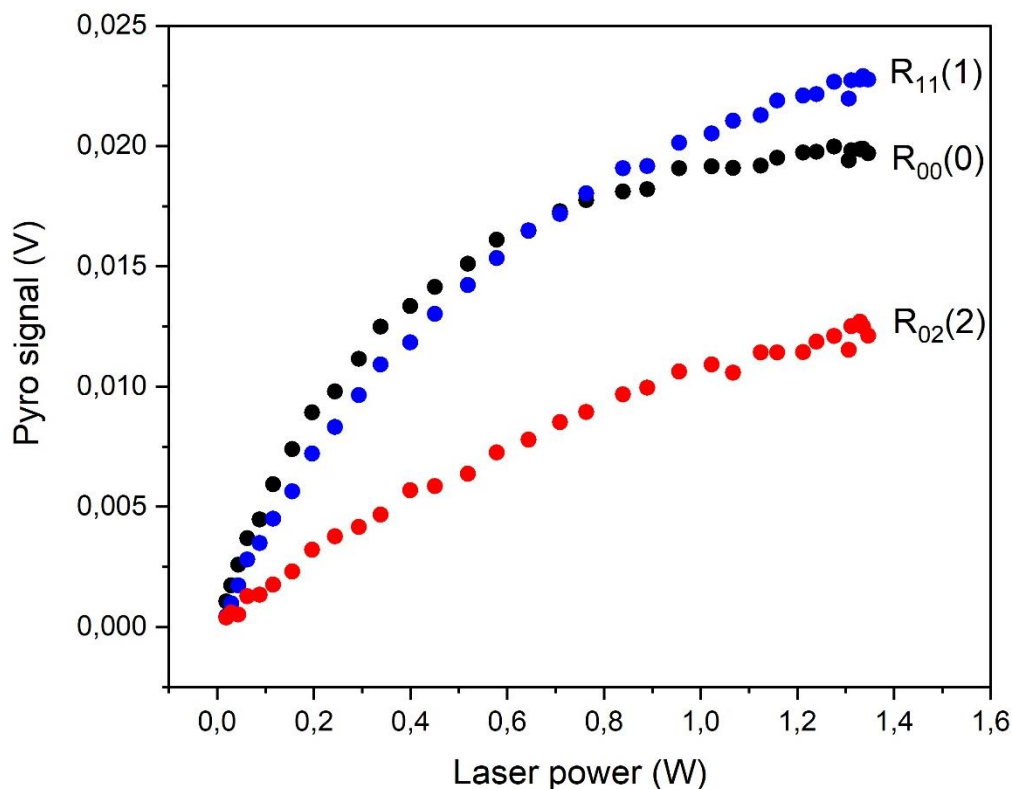


Fig. 2.20: Fluence curves measured for v_3 , R-branch transitions - $R_{00}(0)$, $R_{02}(2)$ and $R_{11}(1)$ for 2% D_2O in He mixture at $T_n = 400$ K ($E_{kin} = 34$ kJ/mol).

Chapter 3: Confirming the mechanism for water dissociation on O-Cu(111) using isotope labeling.

3.1 Overview

The presence of adsorbates on transition metal surfaces can alter some surface reactions significantly. Surface reactivity control with adsorbates that either promote or inhibit surface reactions is an interesting field of study in heterogeneous catalysis. For instance, the water dissociation process in the presence of oxygen adsorbates has been extensively studied on different transition metal surfaces as explained by Henderson in an extensive review of the reactions of water on solid surfaces⁶. It was found that in the presence of oxygen adsorbates, the water dissociation process is facilitated significantly on some metals such as Cu, Ag but only to a small extent on a flat Ni(111) surface^{6,61}.

Water dissociation has received significant attention both from experiment and theory^{6,8} as it is the rate-limiting step in the water-gas shift reaction, $\text{H}_2\text{O} + \text{CO} \rightarrow \text{H}_2 + \text{CO}_2$ used to extract H_2 following the steam-reforming process, $\text{CH}_4 + \text{H}_2\text{O} \rightarrow \text{CO} + 3\text{H}_2$ ⁶². At low temperatures, a common catalyst used for the water-gas shift reaction is based on Cu, while at high temperature a Fe based catalyst is preferred⁶². Based on this, it appears useful to probe the water dissociation reaction on a clean, flat single-crystal Cu(111) surface before proceeding to more complex systems which are used at industrial level. On a clean Cu(111) surface, the barrier for water dissociation is calculated to be 1.50 eV⁵⁰. However, as mentioned above, water dissociation is much more facile on an oxygen covered Cu(111) surface compared to a clean surface as the presence of surface oxygen atoms help to reduce the activation barrier significantly, to a calculated value of 0.56 eV⁵⁰.

Using scanning tunnelling microscopy (STM), Pérez León et al. and Matsumoto et al. found that when oxygen is dosed on clean Cu(111) surface at room temperature, triangular

oxide islands originating either at the step edges, in the vacancies of the terraces or on the terraces are formed^{63,64}. At low O₂ exposure, they observed the step edges to become triangular and form oxides in the upper terrace of the step edges⁶³. Simultaneously, triangular structures originating at the vacancy sites on the terraces also grew on the Cu(111) surface. Whereas, at higher O₂ exposure another form of oxide island formed on the top of the terrace referred to as an added oxide. The added oxide grew on the terrace unlike the step oxide and the terrace oxide - *which grew at the step edges or in the terrace, respectively*. On the other hand, heavy exposure of O₂ at elevated surface temperature resulted in the formation of complex ordered superstructures called “29” and “44” where the oxide formed have hexagonal structures with unit cells that are either 29 or 44 times bigger than the surface unit cell of the Cu^{54,63}.

Mudiyanselage et al. used X-ray photoelectron spectroscopy (XPS) and reflection absorption infrared spectroscopy (RAIRS) to elucidate the water dissociation mechanism on an oxygen covered Cu(111) surface⁶⁵. They reported that background dosing of H₂O on either a clean Cu(111) surface or on a fully oxidized Cu₂O surface, did not result in water dissociation. However, on a partially oxidised Cu(111) surface with 0.1 ML of O(ads), water dissociated readily. In their experiment, the Cu(111) surface was first exposed to O₂ at room temperature to form oxygen adsorbates on the surface. The surface was then exposed to a background dose of H₂O molecules at T_s=90 K which resulted in the formation of H₂O ice. After that, the surface was annealed in steps to T_s=300 K and during this annealing process, they observed a shift in the binding energy of the O 1s in their XPS measurements. They attributed the shift in the binding energy from 533.9 eV (H₂O ice) to 531.4 eV (OH adsorbed) to the water dissociation process. They also observed another shift in the O binding energy from 531.4 eV (OH adsorbed) to 529.5 eV (chemisorbed O) which was explained as the water desorption from the surface. Mudiyanselage et al. found that the pre-dosed oxygen on the surface was recovered following water desorption from the Cu(111) surface. Their experimental observation are consistent with the water dissociation mechanism, H₂O(g) + O(ads) → 2OH(ads).

Jiang and Fang performed density functional theory (DFT) calculations to understand the water dissociation process on a Cu(111) surface⁵⁰. They reported an activation barrier of 1.50 eV for water dissociation on a clean Cu(111) surface but for a surface with O, the

activation barrier was reported to be as low as 0.56 eV⁵⁰. Jiang and Fang also showed that, after the OH formation on either the clean or the oxygen covered Cu(111) from water dissociation, further decomposition of OH has an activation barrier of 2.69 eV and 1.68 eV for the clean and oxygen covered Cu(111), respectively⁵⁰. Thus, in the water dissociation process, the dehydrogenation of the second hydrogen is the rate limiting step⁵⁰. The mechanism proposed by Jiang and Fang for water dissociation on an O covered Cu(111) is the same as Mudiyansele *et al.*, $\text{H}_2\text{O}(\text{g}) + \text{O}(\text{ads}) \rightarrow 2\text{OH}(\text{ads})$ ^{50,65}.

Wang *et al.* investigated the dissociation of water on several transition metal surfaces both bare and with adsorbed oxygen using DFT calculations⁶¹. They proposed that the water dissociation reactivity improves in the following order, $\text{Au} < \text{Ag} < \text{Cu} < \text{Pd} < \text{Rh} < \text{Ru} < \text{Ni}$ ⁶¹. The reactivity reverses on metals with pre-adsorbed oxygen where Ag and Cu highly promote O-H bond scission but Ru and Ni have almost no effect on the water dissociation process⁶¹. Wang *et al.* suggested that the metal surface reactivity to water dissociation is dependent on how strongly oxygen is bound to the surface⁶¹. When the oxygen atoms are adsorbed strongly on a metal surface, the water dissociation process is promoted less and vice versa⁶¹.

Based on the studies above as well as the facile water dissociation observed on the Cu(111) (see section, 1.4 in Chapter 1), I decided to study the dissociation of water on oxygen covered Cu(111) using RAIRS in combination with isotope labeling. Direct detection of two different hydroxyl groups can serve as a direct proof for the hydrogen transfer mechanism ($\text{H}_2\text{O}(\text{g}) + \text{O}(\text{ads}) \rightarrow 2\text{OH}(\text{ads})$). Using different oxygen isotopes for the surface oxide and the incident water species, RAIRS detection is able to distinguish the two hydroxyls, one from the incoming water molecule and the other, as a result of pre-dosed oxygen extracting one hydrogen atom from the incoming water molecule. To date, no RAIRS measurements with isotope labeling have been published for water dissociation on an oxygen covered Cu(111) surface. Most of the experiments that used the $\text{H}_2\text{O}(\text{g}) + \text{O}(\text{ads}) \rightarrow 2\text{OH}(\text{ads})$ mechanism to explain water dissociation on an oxygen covered Cu(111) surface have indirect evidence for the formation of the 2OH(ads) on the surface⁶⁵. Therefore, in this chapter I will present a study of water dissociation on an oxygen covered Cu(111) surface, using isotope labeling for the oxygen atoms (¹⁶O or ¹⁸O) pre-adsorbed on the surface and for the water molecules (H_2^{18}O or H_2^{16}O) that interact with the surface. The products of this reaction were monitored in real

time with RAIRS and AES was employed to quantify the coverage of the pre-dosed O(ads) on the surface and the OH(ads) formed on the surface following water dissociation.

3.2 Molecular or dissociative adsorption of water molecules

Finding out if water adsorption is dissociative or molecular is often not straightforward. Although there are many experimental techniques available to perform this study, there are still disadvantages as highlighted by Henderson⁶. This is due to the H₂O(ads) and OH(ads) having similar properties⁶.

To test if RAIRS can discern between the molecular H₂O(ads) and OH(ads) from the dissociated water molecules on a Cu(111) surface, I performed an experiment where a Cu(111) surface was covered with ice followed by RAIRS measurement Fig. 3.1- black spectrum. The surface was then cleaned by Ar⁺ sputtering followed by annealing as outlined in Chapter 2 (section 2.2.3) followed by a H₂O(g) exposure to yield OH(ads) on an oxygen pre-covered Cu(111) surface. The RAIRS peak corresponding to the hydroxyl adsorbates was identified by performing another RAIRS measurement, Fig. 3.1- red trace.

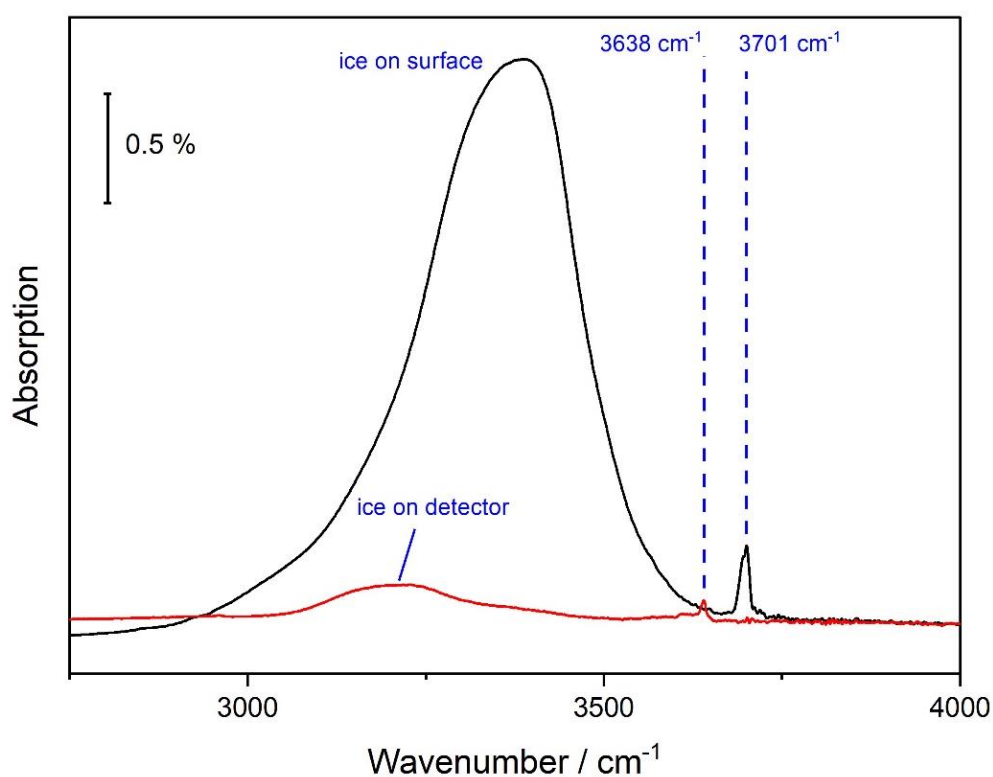


Fig. 3.1: RAIR spectra showing absorption in the O-H stretch region corresponding to ice, OH on ice (3701 cm⁻¹) and OH from dissociated water molecules (3638 cm⁻¹).

The black spectrum was taken after water reaction with Cu(111) surface at $T_s = 90$ K with $E_{kin} = 0.28$ eV which resulted in the formation of ice on the surface. The broadband absorption signal observed around 3480 cm^{-1} is due to the hydrogen bonded O-H stretch vibrations in the ice layers formed on the surface. This band shows a very broad absorption because of the extensive hydrogen bonding between the water molecules in the bulk ice crystal structure resulting in broad absorption frequencies for the O-H stretch⁶⁶. The narrow absorption peak at 3701 cm^{-1} is due to so-called 'free' O-H bonds exposed on the ice surface which are not hydrogen bonded to the neighbouring water molecules⁶⁷.

Repeating the experiment at higher surface temperature, $T_s = 180$ K where no ice layer is formed on the Cu(111) surface resulted on the red spectrum. The sharp RAIRS peak observed at 3638 cm^{-1} is assigned to the OH(ads) formed from the dissociation of the water molecules and chemisorbed directly on the Cu(111) surface. This peak lies in between the broadband ice peak and the free OH on ice. Another broad absorption signal observed in the red trace labelled as 'ice on detector' refers to the IR absorption by the ice formed on the detector element of the liquid nitrogen cooled InSb detector. The water molecules present inside the detector dewar form an ice layer when the detector is cooled by adding liquid nitrogen. To minimize this ice build-up during the RAIRS measurements, I tried to keep the detector continuously cold with liquid N_2 . Alternatively, the dewar has to be evacuated every 3-4 weeks.

The TPD traces in Fig. 3.2 show the desorption temperatures for m/z 18 - H_2O molecules. When a Cu(111) surface covered with ice, Fig. 3.1 – black trace, was heated from $T_s = 90$ -500 K, a sharp desorption peak is observed at temperature $T_s = 177$ K⁷. However, when a TPD measurement was performed for a surface covered with OH(ads), there was a broad desorption peak observed from $T_s = 200$ -300 K as shown in Fig. 3.2 -red trace. It was surprising to observe a sharp desorption peak for ice layers from the surface as it consist of network of water molecules with differing O-H strengths which rendered a broad RAIRS peak in Fig. 3.1. Although the OH(ads) RAIRS peak was sharp Fig. 3.1, it produced a broad desorption signal following recombinative desorption of the hydroxyl adsorbates on the surface.

Since the water molecules from the ice layers desorb with peak desorption temperature at $T_s = 177$ K and the OH recombinatively desorbs ($OH(ads) + OH(ads) \rightarrow H_2O(g) + O(ads)$) as water molecules >150 K with the maximum desorption around 200-320 K, there

is a narrow window in which the water dissociation products are relatively stable without ice formation on the surface. Therefore, I decided to perform my studies of water dissociation on Cu(111) at $T_s = 180$ K in order to adsorb OH on the surface with minimal molecular water adsorption.

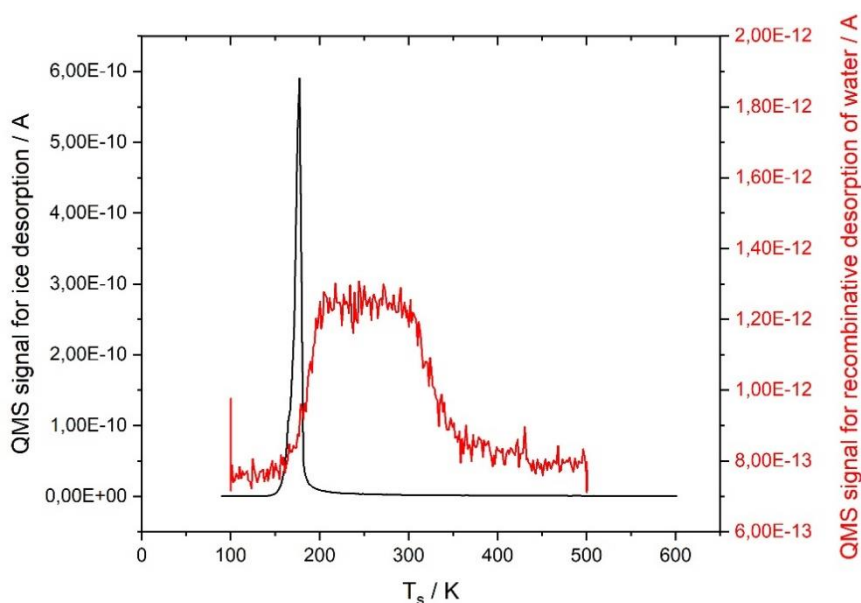


Fig. 3.2: TPD measurements performed with 2 K/s temperature ramp rate, shows ice desorption (black trace- peak desorption at $T_s = 177$ K) and recombinative desorption of water (red trace- highest desorption rate in the range $T_s = 200$ -320 K) from a Cu(111) surface.

At surface temperature, $T_s = 160$ K water can exist either in the metastable or the stable state on the Cu(111) depending on the surface coverage of water ⁷. The metastable state is defined as the near-surface amorphous phase whereas the stable species is the three-dimensional polycrystalline structure on the surface. Although it was demonstrated that the three-dimensional ice and OH adsorbates could be distinguished with RAIRS absorption signals, the metastable phase of water reported by Hinch and Dubois was not observed with this technique ⁷.

By reducing the exposure of D₂O to 0.04 ML on the surface at $T_s = 135$ K, I was able to form the metastable species on the surface which was not observable with RAIRS but was identified from the TPD measurement shown in the blue trace of Fig. 3.3 below. The peak

desorption temperature is observed at $T_s = 155$ K, lower than the stable state, $T_s = 175$ K - black TPD trace, and they agree with the measurements from Hinch and Dubois ⁷. The TPD traces shown below were taken with a ramp rate of 1 K/s.

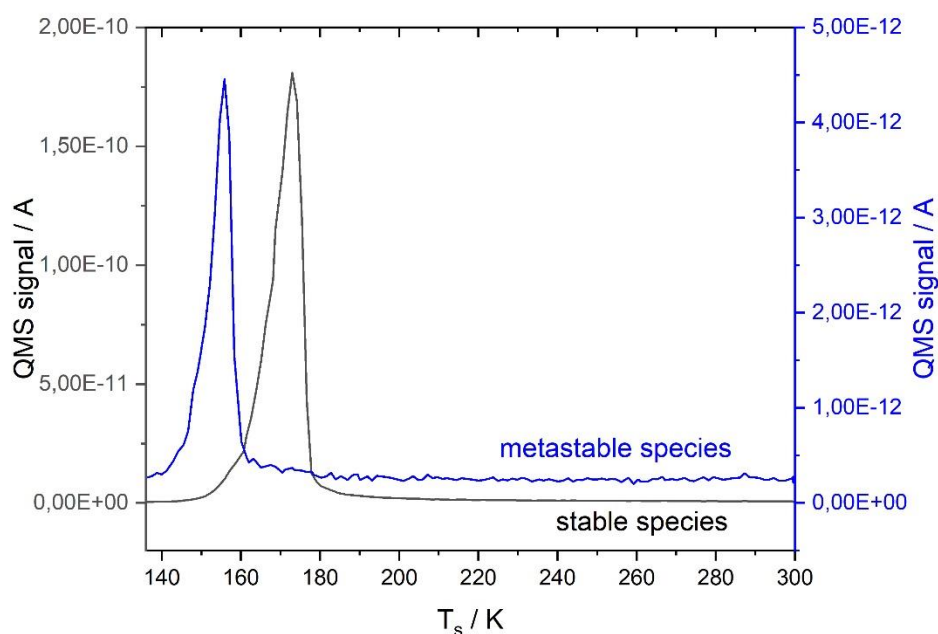


Fig. 3.3: TPD traces of the stable and metastable species of D_2O (0.04 ML -blue and 2 ML- black) formed on a clean Cu(111) surface at $T_s = 135$ K. Temperature ramp rate used was 1 K/s.

3.2 D_2O interaction with $^{16}O(ads)$ or $^{18}O(ads)$ pre-covered Cu(111) surface

In the following sections, I will present experimental data to confirm the water dissociation mechanism, $H_2O(g) + O(ads) \rightarrow 2OH(ads)$ on an oxygen covered Cu(111) surface. I found that the H_2O molecules dissociate on the partially oxygen covered Cu(111) to form $2OH(ads)$ through the transfer of one hydrogen atom from the water molecule onto the surface oxygen atom. Further research revealed that the reverse reaction (disproportionation) occurs simultaneously with water dissociation resulting in the removal of the water molecules from the surface leaving behind oxygen atoms, $OH(ads) + OH(ads) \rightarrow H_2O(g) + O(ads)$. The disproportionation reaction caused the surface oxygen atoms to be replaced by the oxygen atoms from the water molecules. In the next sections, I will discuss the different hypotheses tested to confirm the water dissociation mechanism on a partially oxygen covered Cu(111) surface.

3.2.1 RAIRS detection of OH(ads) isotopologues

Water dissociation on a clean Cu(111) surface was reported to be a highly activated process^{50,68}. Fig. 3.4 (i) shows the RAIRS spectrum of a clean Cu(111) surface at $T_s=180$ K exposed to a molecular beam of $H_2^{16}O$ (37 ML) with $E_{kin}=0.28$ eV. No OH(ads) RAIRS peak is observed in the spectrum indicating the translational energy provided was not sufficient to overcome the activation barrier for water to break its O-H bond on a clean surface. Mudiyansele and co-workers also showed similar observations using XPS⁶⁵.

However, if the Cu surface contained adsorbed oxygen atoms, the water dissociation process proceeds easily without the need for incident translational energy^{65,69}. I detected this facile water dissociation process while studying D_2O dissociation on a clean Cu(111) surface with $E_{kin}=0.28$ eV. At that time, this was a surprising observation as water dissociation has a high activation barrier, calculated to be 1.5 eV⁵⁰. By carefully inspecting the composition of the molecular beam, I found out that there was oxygen in the MB which adsorbed on the Cu(111) and enabled facile water dissociation.

The facile reaction between water molecules and oxygen atoms on the surface was rationalized by a H atom transfer from the incoming water molecule to the adsorbed O atom on the surface, resulting in the formation of 2 hydroxyl adsorbates^{6,65}. This reaction mechanism for water dissociation can be written as $H_2O(g) + O(ads) \rightarrow 2OH(ads)$ and I investigated this mechanism on an oxygen covered single crystal Cu(111) surface with oxygen isotopes, ^{16}O and ^{18}O .

Initially, the Cu(111) surface was cleaned by sputtering and annealing as explained in the surface cleaning procedure in the experimental set-up section. Then, the surface was pre-dosed with $^{18}O(ads)$ by depositing $^{18}O_2$ at $T_s=300$ K (0.07 ML) followed by a molecular beam exposure to $H_2^{16}O(g)$ (58 ML) at $T_s=180$ K with $E_{kin}=0.28$ eV. The pre-adsorbed $^{18}O(ads)$ coverage was measured by using AES. During the surface collision of the $H_2^{16}O$ molecules, RAIR spectra were measured and a single peak was observed to grow at 3637 cm^{-1} , assigned to the $^{16}OH(ads)$ as shown in Fig. 3.4(ii). Interestingly, no RAIRS peak for the $^{18}OH(ads)$ from the pre-dosed oxygen was observed. Based on the water dissociation model, we should have observed two OH(ads) RAIRS peak in Fig. 3.4(ii), one for $^{16}OH(ads)$ and another for $^{18}OH(ads)$. However, our experimental data shows disagreement with the model.

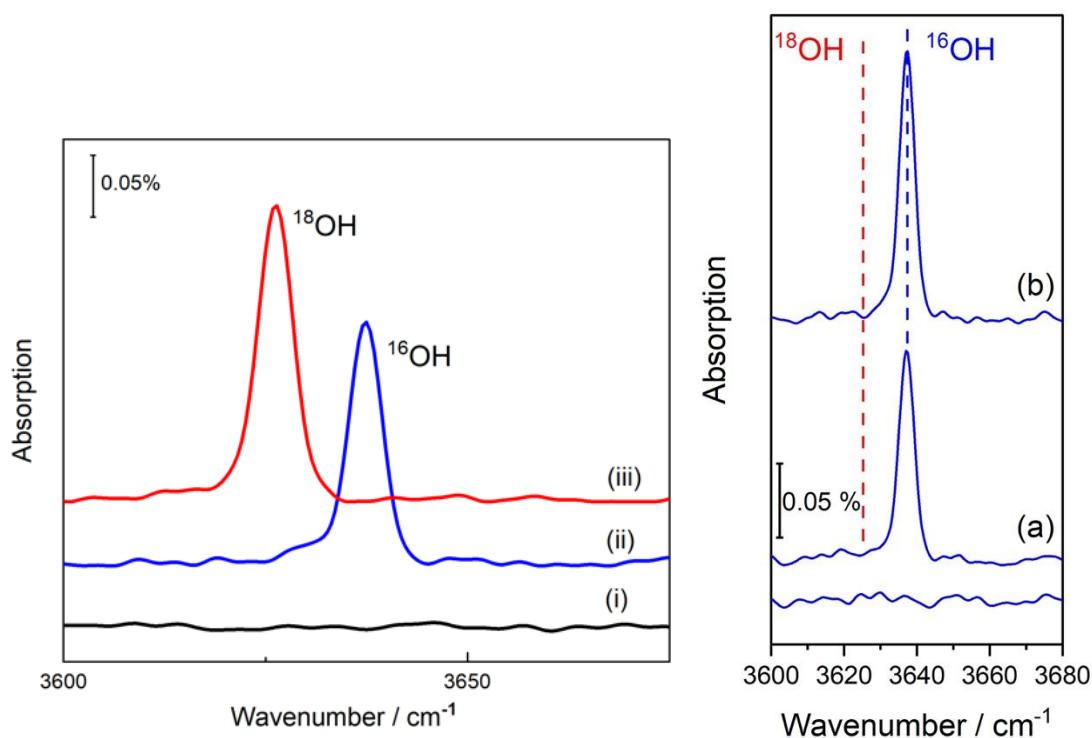


Fig. 3.4: Left- (i) RAIRS spectra for $\text{H}_2^{16}\text{O}(\text{g})$ exposure (37 ML) on a clean Cu(111) surface at $T_s = 180$ K with $E_{\text{kin}} = 0.28$ eV (ii) $\text{H}_2^{16}\text{O}(\text{g})$ dissociation on a $^{18}\text{O}(\text{ads})$ covered Cu(111) surface resulting in a $^{16}\text{OH}(\text{ads})$ RAIRS peak at 3637 cm^{-1} (iii) $\text{H}_2^{18}\text{O}(\text{g})$ dissociation on a $^{16}\text{O}(\text{ads})$ covered Cu(111) surface resulting in a $^{18}\text{OH}(\text{ads})$ RAIRS peak at 3626 cm^{-1} . Right- The uptake for the experiment in the left with $^{16}\text{OH}(\text{ads})$ peak after (a) 3.6 ML and (b) 7.2 ML of H_2^{16}O exposure on a surface with 0.07 ML of $^{18}\text{O}(\text{ads})$.

Table 3: RAIRS frequencies corresponding to the $\text{OH}(\text{ads})$ isotopologues.

Adsorbate	Frequency (cm^{-1})
^{16}OH	3637
^{18}OH	3626

The effect of reversing the O isotopes in the water molecules and the pre-dosed oxygen was then tested by re-cleaning the Cu surface with sputtering and annealing followed by surface exposure to $^{16}\text{O}_2$ at $T_s=300$ K (0.07 ML). After that, a molecular beam of H_2^{18}O (~ 58 ML) was incident at $T_s = 180$ K with $E_{\text{kin}} = 0.28$ eV on the ^{16}O pre-dosed surface. Again, RAIRS measurements were made during the water molecules exposure and this time, a single RAIRS peak assigned to the $^{18}\text{OH}(\text{ads})$ was observed at 3626 cm^{-1} . Fig. 3.4(iii) shows that the $^{18}\text{OH}(\text{ads})$ is 11 cm^{-1} red shifted to the $^{16}\text{OH}(\text{ads})$ stretch in the RAIR spectra. In both the

isotope labelling experiments, the OH(ads) RAIRS peak was observed to solely originate from the dissociation of the incoming water molecules. This is clearly in disagreement with the proposed water dissociation model on a partially oxygen covered Cu(111) surface.

The selection rule of RAIRS states that the surface adsorbates must have a dipole moment component perpendicular to the surface to be 'seen' by RAIRS. Therefore, there is a possibility that the OH from the O isotope pre-dosed on the surface was not observed in RAIRS because this OH adsorbate lies flat on the surface hence rendering no dipole moment component perpendicular to the surface. A study performed by Kumagai *et al.* using the scanning tunnelling microscopy (STM) coupled with DFT calculations on the structure of the hydroxyl adsorbates on a Cu(110) surface demonstrated that an isolated OH(ads) is tilted on a Cu(110) surface ⁷⁰. They also found that the single hydroxyl can undergo a flip in its orientation through electron tunnelling process ⁷⁰. Apart from the isolated OH(ads), Kumagai *et al.* also studied the interaction of the OH(ads) groups in dimers by first depositing O₂ on the surface at T_s=40 K followed by dragging a water molecule into the vicinity of an adsorbed O atom on the surface ⁷⁰. This resulted in the formation of a hydroxyl dimer which no longer did the switch motion because of the strong hydrogen bonding between the hydroxyl groups in the dimer as shown in schematic diagram below ⁷⁰. Based on Kumagai and co-workers' study, the 'missing' OH(ads) peak in Fig. 3.4(ii) and (iii) could perhaps be explained as a result of this hydroxyl adsorbate lying flat on the surface as shown in the schematic below, Fig. 3.5.

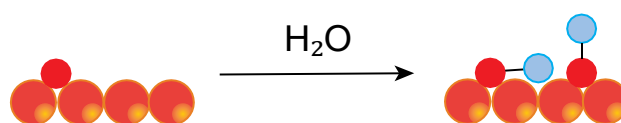


Fig. 3.5: Schematic diagram showing H transfer from the water molecule to the O atom on the surface forming two OH(ads) on the surface where one hydroxyl lies flat and other sits upright. Oxygen atom (red), copper atom (orange) and hydrogen atom (blue).

Based on the RAIRS selection rule, another possible explanation for the 'missing' OH(ads) RAIRS peak is that the hydroxyl adsorbate from the pre-adsorbed oxygen atoms selectively tilt with increasing OH(ads) coverage on the surface. Assuming this hydroxyl first sits upright in the fcc hollow side of the Cu(111) surface and then tilts with increasing OH coverage on the surface, one can measure this process with RAIRS by reducing the incoming

water molecules flux and measuring any reduction in the RAIRS intensity for the OH(ads) formed from the pre-adsorbed O atom on the surface.

To study this, a reduced flux of H_2^{18}O ($3 \cdot 10^{-5}$ ML s^{-1}) was introduced into the UHV chamber where a Cu(111) surface pre-dosed with 0.04 ML of $^{16}\text{O}(\text{ads})$ resides. This was achieved by chopping the molecular beam using a chopper installed in the second chamber with 1 % duty cycle. Fig. 3.6 below shows the RAIRS absorption signal measured in the O-H stretch region during this experiment. Again, there is only a single peak corresponding to the hydroxyl from the incoming water molecules, $^{18}\text{OH}(\text{ads})$ at 3627 cm^{-1} which confirms that there was no continuous tilting of the $^{16}\text{OH}(\text{ads})$ with increasing OH coverage on the surface. Also, it is important to note that with increasing $^{18}\text{OH}(\text{ads})$ coverage on the surface, there is a small blue-shift in its frequency from 3625 cm^{-1} to 3627 cm^{-1} . The frequency shift is attributed to the increasing dipole-dipole interaction between the hydroxyls on the surface with its increasing surface coverage ⁷¹.

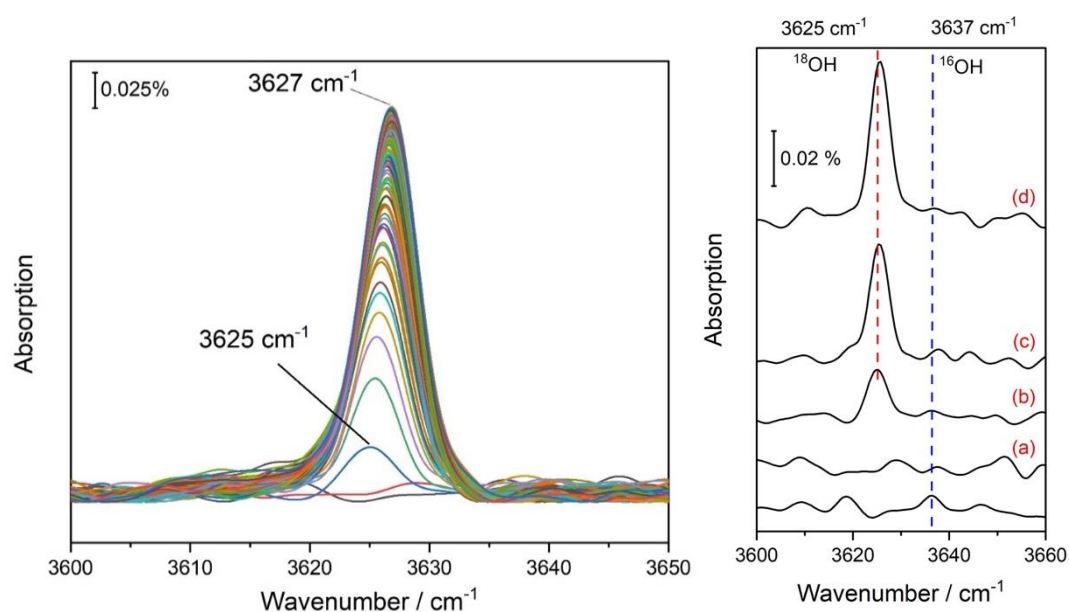


Fig. 3.6: Uptake of $^{18}\text{OH}(\text{ads})$ following water collision on the Cu(111) surface covered with 0.04 ML of $^{16}\text{O}(\text{ads})$. On the right, the first few RAIR spectra from the measurements on the left are shown following $\text{H}_2^{18}\text{O}(\text{g})$ collision on the surface, (a) 0.01 ML, (b) 0.02 ML, (c) 0.03 ML and (d) 0.04 ML.

The $^{16}\text{OH}(\text{ads})$ RAIRS peak, based on the experiment in Fig. 3.6 perhaps was not observed with RAIRS due to the OH adsorbate lying parallel to the surface as shown in Fig. 3.5 or due to the dehydrogenation of the OH(ads) because of its instability, $\text{OH}(\text{ads}) \rightarrow \text{H}(\text{ads}) + \text{O}(\text{ads})$. In order to test this hypothesis, the surface was annealed to higher temperatures

following water dissociation on an 0.02 ML $^{18}\text{O}(\text{ads})$ covered Cu(111) surface at $T_s=180$ K. As shown in Fig. 3.7 below, the $^{16}\text{OH}(\text{ads})$ is not stable at $T_s=220$ K and above. The OH adsorbates desorb from the surface through the disproportionation reaction, $2\text{OH}(\text{ads}) \rightarrow \text{H}_2\text{O}(\text{g}) + \text{O}(\text{ads})$, leaving an O(ads) on the surface⁶⁵. At $T_s=300$ K, all the ^{16}OH adsorbates have desorbed from the surface. Mudiyansele and co-workers also reported similar observation of $^{16}\text{OD}(\text{ads})$ on a Cu(111) surface, where its RAIRS peak showed a decrease in intensity above $T_s = 200$ K and was completely removed from the surface at $T_s = 275$ K⁶⁵.

This experiment also serves as an alternative proof to show that there was no tilting of the ^{18}OH adsorbate formed with the ^{18}O pre-dosed on the surface with increasing OH(ads) coverage on the surface, as previously explained in Fig. 3.6. This is because no other OH RAIRS peak was observed during the annealing process apart from $^{16}\text{OH}(\text{ads})$.

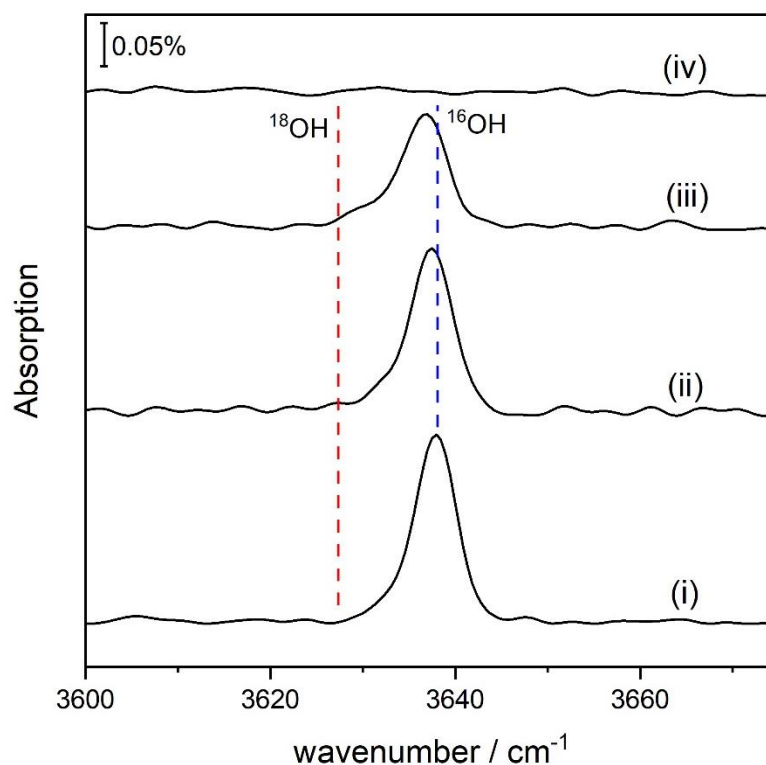


Fig. 3.7: (i) RAIR spectrum measured after 2% H_2^{16}O in He deposition on a surface covered with 0.02 ML of $^{18}\text{O}(\text{ads})$. Following surface annealing to (ii) 220 K, (iii) 250 K and (iv) 300 K, for 2 minutes at each temperature. Dashed red line at 3627 cm^{-1} refers to where the ^{18}OH stretch should be observed.

Perhaps the hydroxyl from the dissociated water molecule was not isolated but interacted with the pre-dosed oxygen hence, prevented the hydrogenation of the pre-adsorbed oxygen. To test this hypothesis, an experiment was performed on a clean Cu(111) surface to check if the OH(ads) RAIRS frequency measured belongs to the isolated OH(ads) on the surface or to an intermediate species.

To study this, the clean Cu(111) surface was exposed to 300 L of $^{16}\text{O}_2(\text{g})$ at $T_s=300$ K resulting in 0.17 ML of $^{16}\text{O}(\text{ads})$ surface coverage. The oxygen exposure was followed by H atoms dosing at $T_s=180$ K using a beam of atomic hydrogen (~ 1 L of H(atom)). A peak at 3634 cm^{-1} is observed in the RAIR spectrum shown in Fig. 3.8. This peak is assigned to the $^{16}\text{OH}(\text{ads})$ and was noted to be 3 cm^{-1} red-shifted to the absorption signal shown for ^{16}OH in Fig. 3.4. The frequency shift can be explained as a result of low $^{16}\text{OH}(\text{ads})$ coverage on the surface, based on Fig. 3.6 above. The result from this experiment shows that the OH(ads) observed in the previous measurements are isolated hydroxyls and not intermediates that interact with neighbouring O(ads) on the surface.

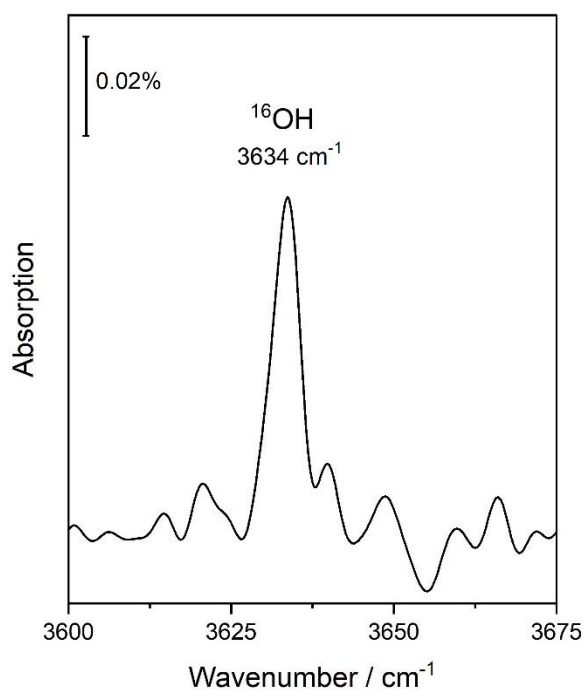


Fig. 3.8: $^{16}\text{OH}(\text{ads})$ RAIRS peak at 3634 cm^{-1} following hydrogenation of $^{16}\text{O}(\text{ads})$ with H atoms.

So far, only OH(ads) from the interacting water molecules was observed and the OH(ads) from the pre-adsorbed oxygen was not measured with RAIRS. The OH(ads) peak observed also exhibited dipole-dipole coupling effect with increasing coverage on the surface and it was shown to be stable up to $T_s = 220$ K. The IR frequency measured for the OH(ads) was confirmed to arise from the isolated hydroxyl species on the surface.

3.2.2 Saturation depends on the pre-dosed O(ads) coverage

It is still unclear if the O(ads) pre-dosed on the surface acts as a spectator in the water dissociation process or participates in the reaction. To further investigate this problem, I probed the role of the initially adsorbed O(ads) by varying the oxygen coverage on the surface prior to water molecules exposure. If oxygen pre-dosed on the surface acts only as a catalyst and is not consumed in the reaction, the maximum hydroxyl coverage achieved for the different pre-adsorbed oxygen coverage would remain the same. In contrary, if the surface oxygen converts into hydroxyl by accepting a hydrogen from the water molecule, then the saturation coverage attained for the different pre-dosed oxygen coverage will vary as the limiting parameter is the available oxygen adsorbates for the reaction.

To perform this study, three known coverage of O(ads) on a Cu(111) surface were used. Prior to this experiment, the oxygen coverage on the surface was measured with AES and calibrated based on the known saturation coverage of O(ads)– 0.5 ML⁵⁴. More details are explained in chapter 4.

The following Fig. 3.9 shows the absorption signal peak height for $^{16}\text{OD(ads)}$ measured with RAIRS at 2689 cm^{-1} on a surface pre-dosed with 0.02 ML, 0.07 ML and 0.09 ML of $^{18}\text{O(ads)}$, during $\text{D}_2^{16}\text{O(ads)}$ collision with the Cu(111) at $T_s = 180$ K. The water molecules arrived on the surface with $E_{\text{kin}} = 0.28$ eV. Again, only a single peak was observed for the OD(ads) on the surface, belonging to the water molecules from the molecular beam – $^{16}\text{OD(ads)}$. Based on the Fig. 3.9, it is clear that the saturation peak heights achieved for the different surface oxygen coverage increased with increasing oxygen on the surface which indicates the initial ^{18}O adsorbates are consumed in the reaction as suggested by Mudiyansele et al.⁶⁵.

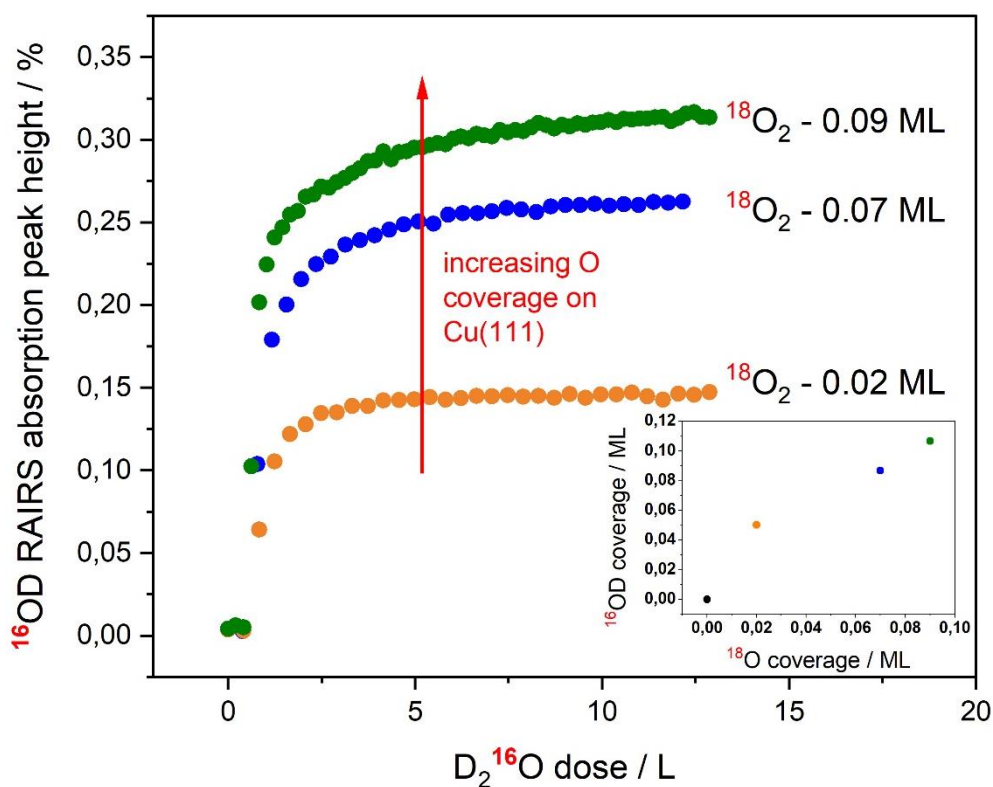


Fig. 3.9: RAIRS absorption signal peak height for $^{16}\text{OD}(\text{ads})$ measured at 2689 cm^{-1} with increasing exposure of $\text{D}_2^{16}\text{O}(\text{g})$ on the $\text{Cu}(111)$ surface with varying pre-adsorbed $^{18}\text{O}(\text{ads})$ coverage. The inset compares the initial $^{18}\text{O}(\text{ads})$ coverage on the surface with $^{16}\text{OD}(\text{ads})$ coverage following $\text{D}_2^{16}\text{O}(\text{g})$ dissociation.

It is also very interesting that the $^{16}\text{OD}(\text{ads})$ coverage exhibits a linear increase with the pre-adsorbed $^{18}\text{O}(\text{ads})$ coverage on the surface, shown in inset of Fig. 3.9. Further analysis of this information shows that for a surface with 0.02 ML of pre-adsorbed $^{18}\text{O}(\text{ads})$, 0.05 ML of $^{16}\text{OD}(\text{ads})$ was measured on the surface, which is 2.5 times more than the oxygen coverage we started with. Every oxygen atom reacted with one incoming water molecule to form $2\text{OD}(\text{ads})$ on the surface, therefore giving twice the coverage of $\text{OD}(\text{ads})$ compared to the initially pre-dosed $\text{O}(\text{ads})$ coverage. However, in this case only the $^{16}\text{OD}(\text{ads})$ peak was observed with RAIRS so, there should have been approximately 0.02 ML of $^{16}\text{OD}(\text{ads})$ measured if two $\text{OD}(\text{ads})$, one $^{16}\text{OD}(\text{ads})$ and one $^{18}\text{OD}(\text{ads})$ were formed from the reaction. Instead, a 0.05 ML of only $^{16}\text{OD}(\text{ads})$ was measured. This observation can be explained as a result of the disproportionation reaction, which will be explained later in this chapter.

When the initial coverage of $^{18}\text{O}(\text{ads})$ was increased to 0.07 ML and 0.09 ML, the $^{16}\text{OD}(\text{ads})$ coverage was measured to be 0.09 ML and 0.11 ML, respectively. Although for

these initial $^{18}\text{O}(\text{ads})$ coverages, the $^{16}\text{OD}(\text{ads})$ coverage increased on the surface, the increment is not almost twice the $^{18}\text{O}(\text{ads})$ coverage as observed for the 0.02 ML of $^{18}\text{O}(\text{ads})$ instead, it is only 20-30% more than the initial oxygen atom coverage. This indicates the presence of oxygen islands on the surface ⁶³. Water dissociates at the periphery of these islands thus, as the surface oxygen coverage increases, these islands get larger rendering less available reactive sites (oxygen on the periphery of the islands) for the reaction.

3.3 Mechanism of water dissociation

3.3.1 Finding H atoms with RAIRS

Based on the published mechanism for water dissociation on an oxygen covered surface ($\text{H}_2\text{O}(\text{ads}) + \text{O}(\text{ads}) \rightarrow 2\text{OH}(\text{ads})$) coupled with isotopic oxygen atoms – $^{18}\text{O}_2$ and $^{16}\text{O}_2$, we expected to measure two hydroxyl RAIRS peaks ⁶. However, time and again only one absorption signal belonging to the $\text{OH}(\text{ads})$ from the incoming water molecules was measured using RAIRS. Perhaps the oxygen on the Cu(111) surface is not a participant in the reaction but acts just as a catalyst which reduces the barrier for water dissociation on a Cu(111) surface. If this is true, after water molecules dissociate on an oxygen covered surface, the surface must be covered with isolated H atoms.

Mudiyanselage et al. measured the H-Cu stretch with RAIRS as a sharp feature at 1153 cm^{-1} for $T_s = 180\text{ K}$ ⁷². They proposed that this peak only appears in the RAIRS measurement when the hydrogen atoms occupy both the sub-surface sites and the three-fold hollow sites on the Cu(111) surface, as the absorption signal at 1153 cm^{-1} was suggested to arise due to the vibrational coupling between the sub-surface and surface hydrogen atoms.

In our lab, a Cu(111) surface covered with hydrogen atoms was prepared by a hydrogen atom beam source (HABS) operated at 1600 K. The surface was exposed to different amounts of H atoms followed by RAIRS measurements as shown in Fig. 3.10 – left. The surface was then heated to remove the hydrogen atoms by recombinative desorption while recording a TPD measurement shown in Fig. 3.10- right. The RAIRS measurement shows a peak at 1153 cm^{-1} after the surface was exposed to 250 L (calculated by taking the lowest limit of cracking efficiency of H_2 , 80% multiplied by the exposure of $\text{H}_2(\text{g})$ in Langmuir) – Figure 3.10, left (a).

This peak was observed to red-shift to 1147 cm^{-1} when the H atoms exposure was increased to 1588 L.

Performing a TPD measurement for a surface dosed with 1588 L of H produced a shoulder at $T_s = 240\text{ K}$ to the desorption peak at $T_s = 310\text{ K}$. Increasing the H exposure to 1941 L and then performing a TPD measurement, resulted in two clear peaks in the TPD trace observed at $T_s = 240\text{ K}$ and $T_s = 310\text{ K}$. The peak at 240 K was assigned to the H atoms from the sub-surface and the peak at 310 K was assigned to surface hydrogen atoms⁷². By analysing the area under the peaks in the TPD traces, one can identify the surface sites from which the H atoms desorb. When the H(atom) exposure was increased from 1588 L to 1941 L the higher temperature TPD peak shows a constant area suggesting this peak to belong to the surface adsorbed H atoms as the surface adsorption sites on the Cu(111) from which H atoms can desorb are limited. The TPD peak with the lower temperature instead shows an increment in the area under the peak when the H(atom) exposure was increased from 1588 L to 1941 L which indicates a higher number of sites available for H atoms, the sub-surface sites. Whereas, for a lower H(atom) exposure- 160 L, only a single peak at 320 K is observed in the TPD trace of Figure 3.10, right panel (a). Since this is the only peak observed at low hydrogen dose, it appears that the hydrogen atoms adsorb on the surface sites first followed by the sub-surface sites.

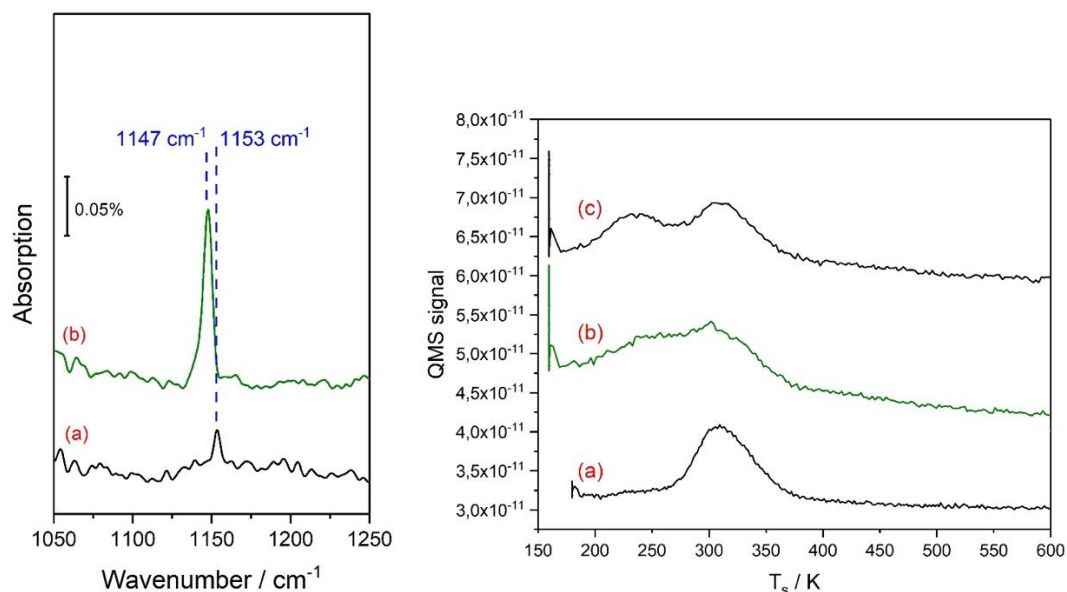


Fig. 3.10: Left - RAIR spectra measured with MCT detector following (a) 250 L and (b) 1588 L of H(atoms) exposure using HABS. Right - TPD traces showing desorption of H_2 from the Cu(111) surface when the surface was heated with a 2 K/s heating ramp. The surface was initially exposed to (a) 160 L, (b) 1588 L and (c) 1941 L of H atoms.

When water molecules were dissociated on a $^{16}O(\text{ads})$ - 0.17 ML covered Cu(111) surface, no peak was observed for the H-Cu stretch around 1153 cm^{-1} . This is most likely due to the low coverage of H atoms formed from the water dissociation which led to the absence of the sub-surface hydrogen atoms. Since both the surface adsorbed and sub-surface H atoms are required to be present simultaneously for the appearance of the RAIRS absorption signal at 1153 cm^{-1} , the peak around 1153 cm^{-1} was not observed after water dissociation on a Cu(111) surface. In summary, no conclusive result was obtained to prove the presence/absence of the isolated H atoms on the surface of the Cu(111) surface following water dissociation on an oxygen covered surface.

3.3.2 Using HABS to identify the products of water dissociation

Another method to check if the O(ads) pre-dosed on the surface was hydrogenated during the water dissociation process, is to perform an experiment which allows the growth of the 'missing' OH(ads) RAIRS peak with the aid of hydrogen atoms. For this experiment, I pre-dosed a clean Cu(111) surface with approximately 0.07 ML of $^{16}O(\text{ads})$ - and then exposed the surface to a background dosing of $H_2^{18}O(\text{g})$ - $7 \cdot 10^{-9}$ mbar. As shown in Fig. 3.11 this

experiment resulted in the growth of a single peak at 3627 cm^{-1} assigned to the $^{18}\text{OH}(\text{ads})$ on the surface. After that, the surface was exposed to H atoms with HABS resulting in the formation of the $^{16}\text{OH}(\text{ads})$ peak at 3639 cm^{-1} .

This previously 'missing' peak for $^{16}\text{OH}(\text{ads})$ increased in intensity with increasing H atoms exposure and simultaneously, the $^{18}\text{OH}(\text{ads})$ peak reduced in intensity. The decrease in the $^{18}\text{OH}(\text{ads})$ peak intensity can be explained by the hydrogenation of the $^{18}\text{OH}(\text{ads})$ during the H atoms exposure, $^{18}\text{OH}(\text{ads}) + \text{H}(\text{atom}) \rightarrow \text{H}_2^{18}\text{O}(\text{g})$, resulting in its removal from the surface as gaseous water molecules. The red-shift in the frequency of the $^{18}\text{OH}(\text{ads})$ stretch with increasing H atoms exposure can be explained as reduced dipole-dipole coupling between the $^{18}\text{OH}(\text{ads})$ on the surface as its coverage reduces on the surface.

Furthermore, the 3639 cm^{-1} peak assigned to the $^{16}\text{OH}(\text{ads})$ RAIRS peak increases in intensity with increasing background dosing of H atoms. This indicates the pre-dosed $^{16}\text{O}(\text{ads})$ on the Cu(111) surface was not fully hydrogenated following H_2^{18}O dissociation. However, this conclusion might be misled because water dissociation occurs only at the periphery of the oxygen islands therefore, there were still free O atoms on the surface for hydrogenation.

It is known that oxygen dosing on a clean Cu(111) surface results in the formation of local surface oxidation where the oxygen atoms form islands originating at the defects⁶³. The oxygen atoms on the periphery of the islands are expected to react with the incoming water molecules but the oxygen atoms in the middle of the islands are not reactive as there are no neighbouring Cu sites available for the adsorption of $\text{OH}(\text{ads})$ from the dissociation of the water molecules. A similar presence of reactive and non-reactive oxygen atoms to water dissociation was reported by Grellner *et al*⁷³. Therefore, the $^{16}\text{OH}(\text{ads})$ observed in Fig. 3.11 could be the result of hydrogenation of the non-reactive O atoms in the middle of the O islands and not from the reactive oxygen atoms.

The $^{16}\text{OH}(\text{ads})$ peak was also observed to red-shift (6 cm^{-1}) with increasing coverage on the surface and this is in contradiction to the previous observation in Fig. 3.6 where with increasing $\text{OH}(\text{ads})$ coverage on the surface, the RAIRS peak blue-shifted. Two effects are suspected to contribute to this observation. One is the dipole-dipole coupling between the ^{16}OH adsorbates on the surface with increasing hydrogenation of the unreactive oxygen on the surface. However, this effect would result in a blue-shift in the absorption which is not

the case here therefore, the dipole-dipole coupling effect is expected to be small. As the net frequency shift is towards the lower frequency, it indicates weakening of the O-H bond which is proposed to be a consequence of hydrogen bonding between the oxygen of the $^{16}\text{OH}(\text{ads})$ and the hydrogen adsorbates.

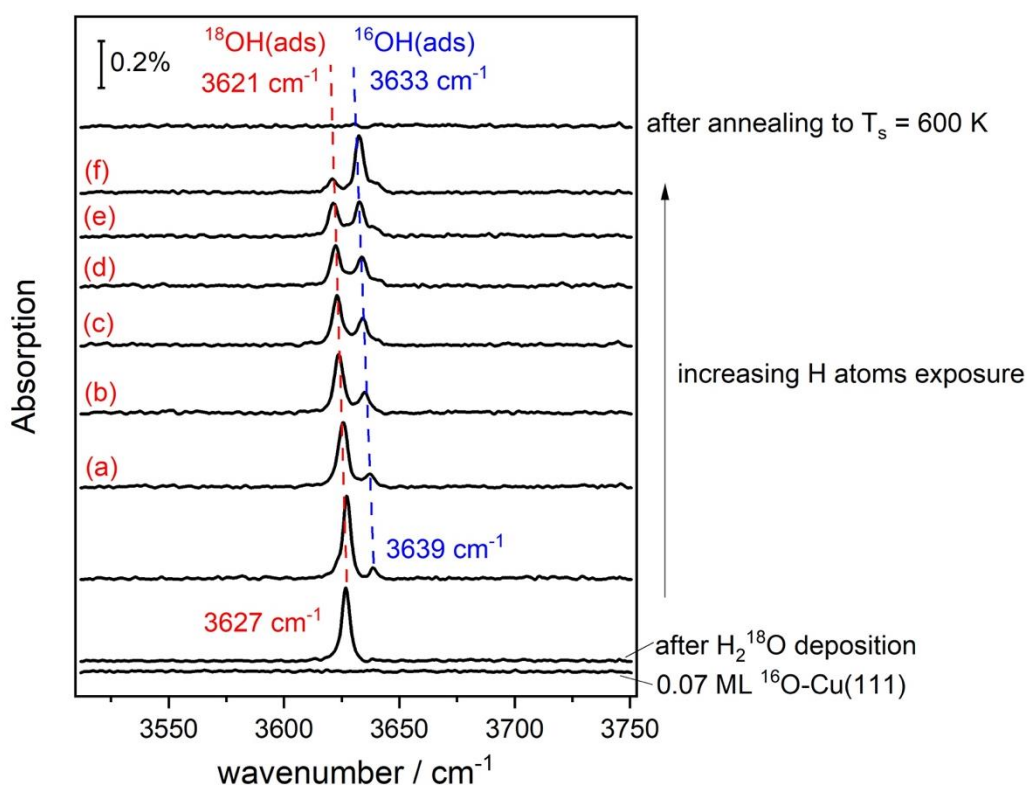


Fig. 3.11: The uptake of the $^{16}\text{OH}(\text{ads})$ - 3639 cm^{-1} absorption signal measured after surface exposure to hydrogen atoms from HABS. The surface was initially dosed with 0.07 ML of $^{16}\text{O}(\text{ads})$ oxygen and then reacted to water molecules until the $^{18}\text{OH}(\text{ads})$ - 3627 cm^{-1} RAIRS peak saturated. The H(atoms) dose was as following, (a) 0.2 L, (b) 0.4 L, (c) 0.4 L, (d) 0.4 L, (e) 0.8 L and (f) 17.6 L.

During the exposure of water molecules, the $\text{OH}(\text{ads})$ adsorbates were observed to act as anchor points to trap molecular water forming $\text{OH} + \text{H}_2\text{O}$ mixed layer on the surface¹⁵. It has been reported that the water molecules trapped between $\text{OH}(\text{ads})$ on the surface are strongly bound hence desorbs at a higher surface temperature than from molecular water with no interaction with surface hydroxyls. For instance, on $\text{Cu}(110)$ the peak desorption temperature for water molecules on a clean surface was reported at $T_s = 170\text{ K}$ whereas, the

tightly bound water from the mixed OH + H₂O layer was observed to desorb at T_s = 200 K and 235 K ⁷⁴.

The interaction of the OH(ads) with trapped water molecules on a Cu(111) was tested by colliding a MB of 2% D₂¹⁶O in He with a Cu(111) surface, initially dosed with 0.07 ML of ¹⁶O(ads). The surface was kept at T_s = 170 K during this experiment, lower than the peak desorption temperature for ice on the surface. Fig. 3.12 – top panel shows the changes in the RAIRS peak height for ¹⁶OD(ads) on the surface with and without the MB. The result demonstrates how the RAIRS peak intensity is hampered by 40% when the MB is on and its recovery upon stopping the MB. The King and Wells measurement presented in Fig. 3.12 – bottom panel instead shows the QMS signal for m/z 20 obtained simultaneously with the RAIRS spectra in Fig. 3.12- top panel.

When the flag no longer blocked the surface, clear dips are observed in the QMS trace indicating adsorption of the water molecules whereas when the flag was moved into the MB, upward spikes are detected in the QMS trace indicating desorption of the water molecules from the surface. This shows that the trapped water molecules were short-lived on the surface thus were removed instantly upon blocking of the MB, shown by black arrows in Fig. 3.12- bottom panel.

The instant desorption of water molecules at low surface temperature, T_s = 170 K suggests that they do not originate from the OH + H₂O mixed layer on the surface but from the clean Cu atom surface sites. Since the Cu(111) was not fully covered with the pre-adsorbed oxygen atoms, a large fraction of oxygen-free Cu atoms were available for molecular water adsorption which must be where the water molecules observed in Fig. 3.12 originate from.

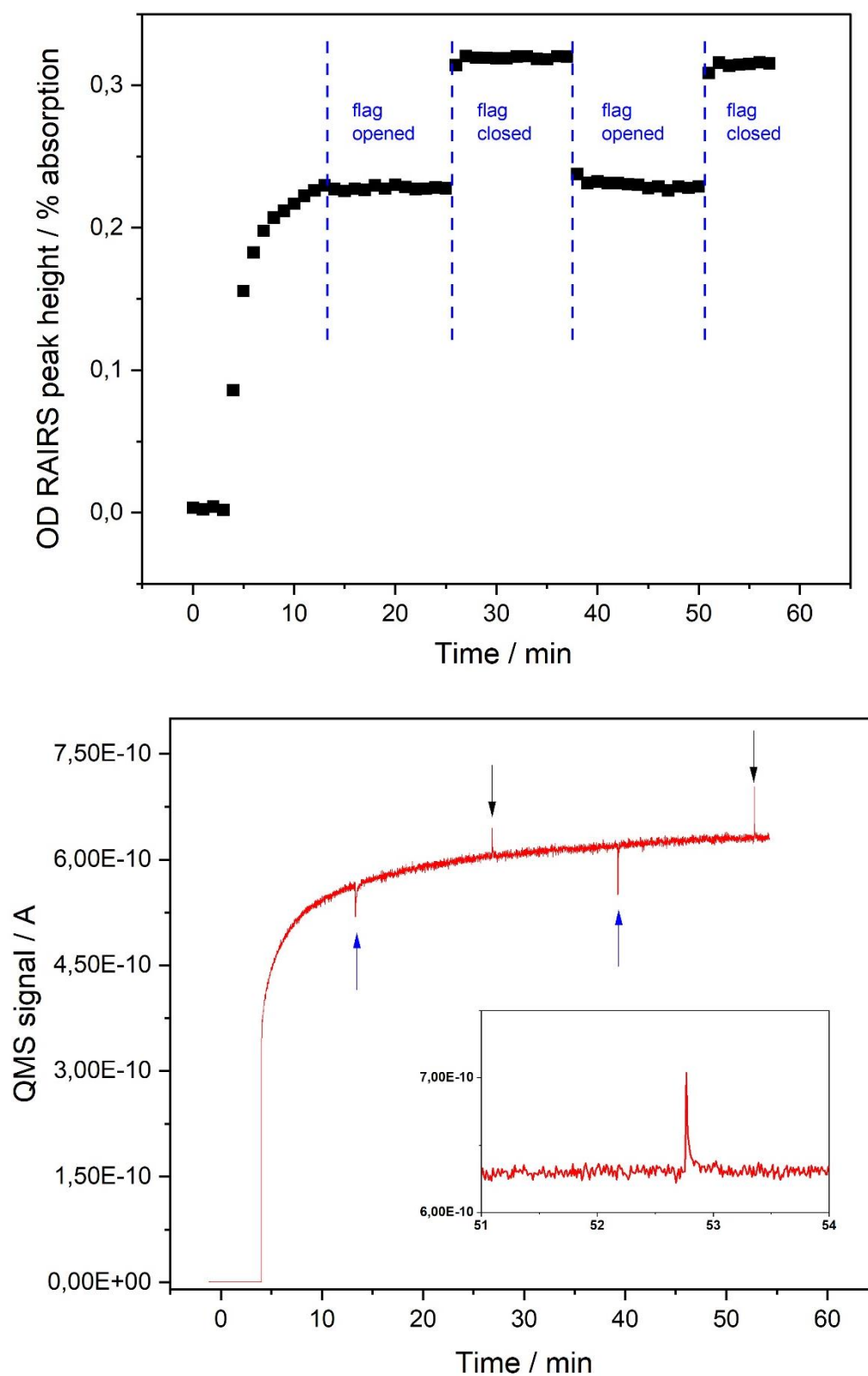


Fig. 3.12: Top panel- The ^{16}OD coverage on the surface with increasing deposition of D_2^{16}O on 0.07 ML $^{16}\text{O}(\text{ads})$ pre-dosed Cu(111) surface. Bottom panel- QMS trace for the m/z 20 where the blue arrows show the time when the flag was removed from the MB path while the black arrows show the time when the flag was placed in the MB path. Inset shows a QMS spike observed at around time=53 minutes when the flag blocked the MB from the surface.

To complement the RAIRS measurements in Fig. 3.11, during H atoms exposure on the surface, QMS measurements were also performed and are presented in Fig. 3.13. The labels shown in Fig. 3.13 match with those in Fig. 3.11. It is clear that every time H atoms were exposed on the surface, the QMS signals for m/z 20 and 17 show increments as a result of removal of water molecules following hydrogenation of $^{18}\text{OH}(\text{ads})$ into H_2^{18}O and double hydrogenation of $^{16}\text{O}(\text{ads})$ into H_2^{16}O , respectively. For the $\text{H}_2^{16}\text{O}(\text{g})$, I monitored the QMS signal for m/z 17 instead of 18 because m/z 18 have approximately 20% contribution from $\text{H}_2^{18}\text{O}(\text{ads})$ but m/z 17 comes from only $\text{H}_2^{16}\text{O}(\text{g})$.

Looking closely at the area below m/z 17 and 20 of the respective QMS traces, one can say that almost three times more of $\text{H}_2^{16}\text{O}(\text{g})$ (m/z 18 calculated from the fragmentation yield of m/z 17) desorbed from the surface compared to $\text{H}_2^{18}\text{O}(\text{g})$ - Fig.3.13 (a). This is a surprising observation as we know that the $^{18}\text{OH}(\text{ads})$ needs to hydrogenate only once unlike the $^{16}\text{O}(\text{ads})$ which has to hydrogenate twice before desorbing as water molecules. Based on this, the obvious expectation was to have more of the $\text{H}_2^{18}\text{O}(\text{g})$ desorbing compared to $\text{H}_2^{16}\text{O}(\text{g})$. Since this is not what was observed, the measurement can be explained as a result of hydrogen atoms beam size. During H atoms deposition, the area covered by the beam is bigger than the surface area. As water molecules are sticky, they are always present on the inner walls of the UHV chamber which could have dislodged when H atoms struck the walls causing a higher rise in QMS signal for m/z 17 than m/z 20.

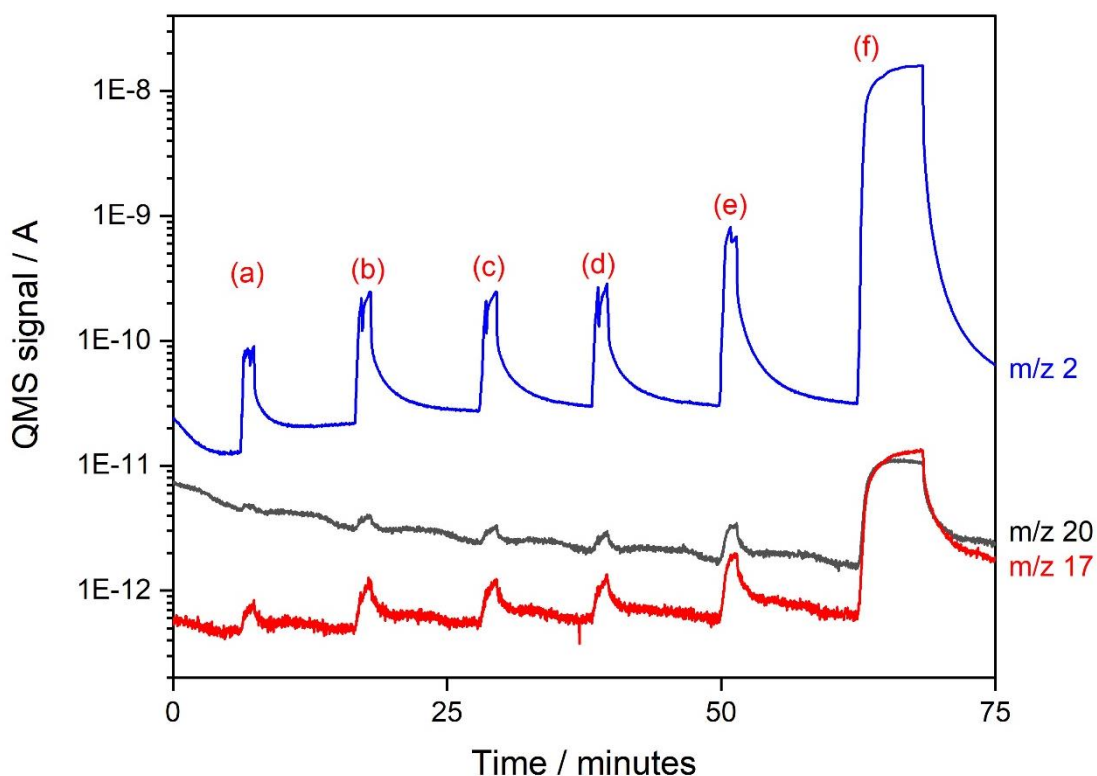


Figure 3.13: QMS trace for m/z 20 ($H_2^{18}O$), m/z 17 (fragment of $H_2^{16}O$) and m/z 2 (H_2) during the exposure of H atoms from the HABS. The labels (a-f) match with the RAIR spectra in Fig. 3.11.

3.3.3 Reducing incoming water flux

Water flux incident on the surface can be reduced by chopping the MB which lowers the flux by $\times 100$ compared to without a chopper (typically 0.03 ML s^{-1}). An alternate way to significantly reduce the number of water molecules that arrive on the surface is by using the water molecules in the UHV background. The partial pressure of H_2O originating from the UHV chamber is typically around $1.1 \cdot 10^{-11} \text{ mbar}$ and the molecules impinging on the surface was estimated to be $2 \cdot 10^{-6} \text{ ML s}^{-1}$.

Figure 3.14 shows the results of an experiment where the Cu(111) surface was first dosed with 0.07 ML of ^{18}O and then left in the UHV background (pressure = $\sim 10^{-11} \text{ mbar}$) where it was exposed to water molecules ($H_2^{16}O$) present in the UHV background for 32 minutes before leaking in $H_2^{16}O$ directly into UHV (pressure = $7 \cdot 10^{-10} \text{ mbar}$) - Fig. 3.14. Initially, two absorption peaks are observed to grow in the O-H stretch region, one for $^{16}OH(\text{ads})$ and one for $^{18}OH(\text{ads})$. What is interesting here is of course, the presence of the $^{18}OH(\text{ads})$ formed by H transfer from the incident $H_2^{16}O$ to $^{18}O(\text{ads})$. **This is the 'missing' RAIRS OH peak that**

we were not able to observe with RAIRS in all the previous experiments. The difference between this and the previous experiments, is that now the incident water flux is three orders of magnitude lower than while exposing the surface to the molecular beam or during background exposures (water partial pressure = $\sim 10^{-8}$ mbar).

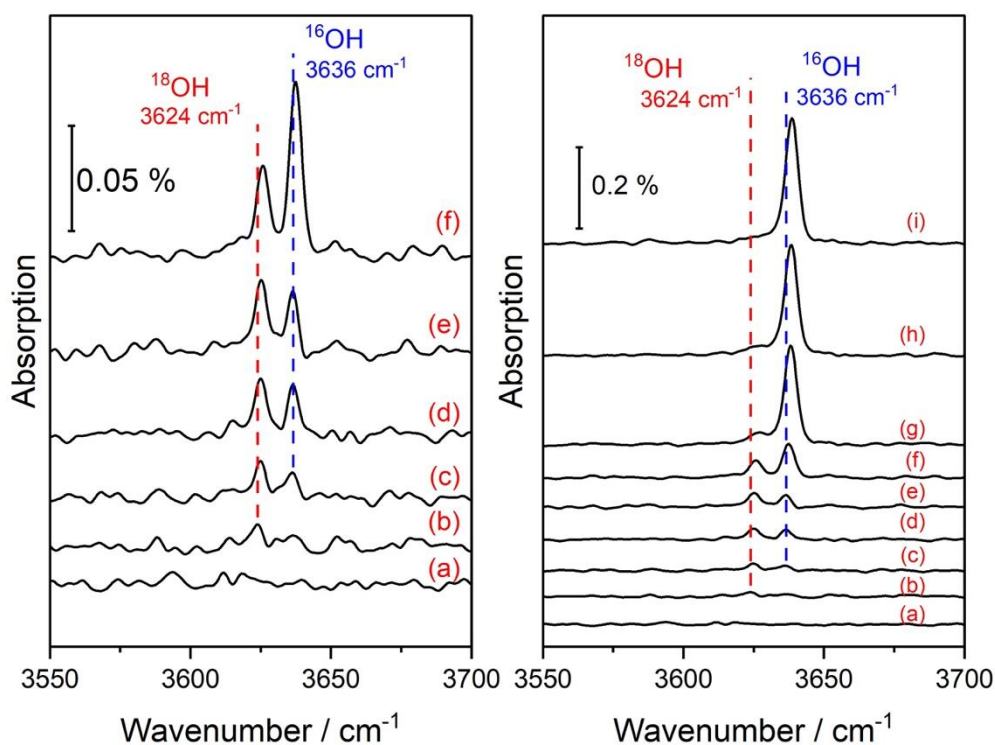
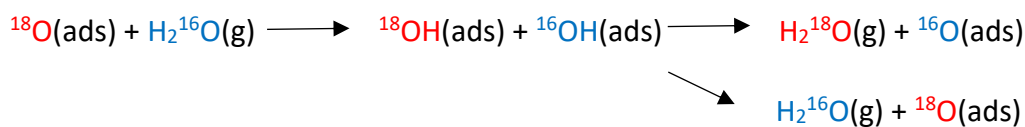


Fig. 3.14: RAIR spectra showing the uptake of two OH(ads) peaks on a partially oxygen covered Cu(111) surface- 0.07 ML of $^{18}\text{O}(\text{ads})$. Both the spectra on the left and right are from the same experiment where the spectra were taken (a) after 0.07 ML $^{18}\text{O}(\text{ads})$ surface coverage, (b)-(f) following background water molecules exposure and (g)-(j) following H_2^{16}O leak into UHV chamber. (b) $2 \cdot 10^{-3}$ L, (c) $5 \cdot 10^{-3}$ L, (d) $1 \cdot 10^{-2}$ L, (e) $1.5 \cdot 10^{-2}$ L, (f) $1.6 \cdot 10^{-2}$ L, (g) 0.13 L, (h) 0.28 L and (i) 0.92 L.

Though the $^{18}\text{OH}(\text{ads})$ signal initially grows together with the $^{16}\text{OH}(\text{ads})$ signal, it is observed to reach a maximum and then starts to decrease in intensity while the $^{16}\text{OH}(\text{ads})$ signal continues to grow in intensity (Fig. 3.14). This indicates that the $^{18}\text{OH}(\text{ads})$ adsorbates are unstable and are removed by a secondary reaction which most likely is the disproportionation reaction with $^{16}\text{OH}(\text{ads})$ leading to their desorption as $\text{H}_2^{18}\text{O}(\text{g})$, leaving $^{16}\text{O}(\text{ads})$ on the surface.



After 32 minutes, $\text{H}_2{}^{16}\text{O}(\text{g})$ was leaked directly into the UHV chamber ($7 \cdot 10^{-10}$ mbar) and the results obtained are shown in Fig. 3.14 (g-i). In this case, the ${}^{18}\text{OH}(\text{ads})$ RAIRS peak was observed to reduce until the peak disappeared while the ${}^{16}\text{OH}(\text{ads})$ RAIRS absorption signal increased significantly with increasing $\text{H}_2{}^{16}\text{O}$ exposure (from 0.13 L to 0.92 L). From this observation it is evident that when the surface was exposed to a higher flux of incoming water molecules, only a single RAIRS peak of $\text{OH}(\text{ads})$ with O of the incoming water molecules was measured due to the removal of the pre-adsorbed ${}^{18}\text{O}$ from the surface through the disproportionation reaction.

In order to test the hypothesis for the replacement of the pre-dosed oxygen ${}^{18}\text{O}(\text{ads})$ by ${}^{16}\text{O}(\text{ads})$ through a disproportionation reaction of the hydroxyls, the QMS signal for m/z 20 ($\text{D}_2{}^{16}\text{O}$ and fragment of $\text{D}_2{}^{18}\text{O}$) and 22 ($\text{D}_2{}^{18}\text{O}$) were monitored in a K&W experiment exposing a Cu(111) surface pre-dosed with 0.07 ML of ${}^{18}\text{O}(\text{ads})$ to a 2% D_2O in He beam. The results are presented Fig. 3.15. An increase in the m/z 22 QMS signal (red trace) is observed upon admission of the MB into the UHV chamber while the K&W flag still blocks the molecular beam from striking the surface. When the flag was removed after $t=760$ seconds and the $\text{D}_2{}^{16}\text{O}$ beam collides with the Cu(111) a rapid rise in the QMS signal for m/z 22 and a drop in the signal for m/z 20 are observed. A spike in the QMS signal for m/z 22 is a proof that the disproportionation reaction occurred resulting in the removal of $\text{D}_2{}^{18}\text{O}(\text{g})$ m/z 22 as explained previously. The dip for m/z 20 instead is a consequence of the molecular and dissociated $\text{D}_2{}^{16}\text{O}(\text{g})$ adsorption on the oxygen covered Cu(111) surface. The fragment of m/z 22 which contributes to the m/z 20 signal in the QMS trace is approximately 20% based on the fragmentation of H_2O obtained from the National Institute of Standards and Technology (NIST) hence it is negligible in this case. Based on the measurements from Fig. 3.14 and Fig. 3.15, the reactive ${}^{18}\text{O}$ on the periphery of the oxygen islands are selectively exchanged with ${}^{16}\text{O}$ producing islands of ${}^{18}\text{O}$ with ${}^{16}\text{O}$ decorating the perimeter of these islands.

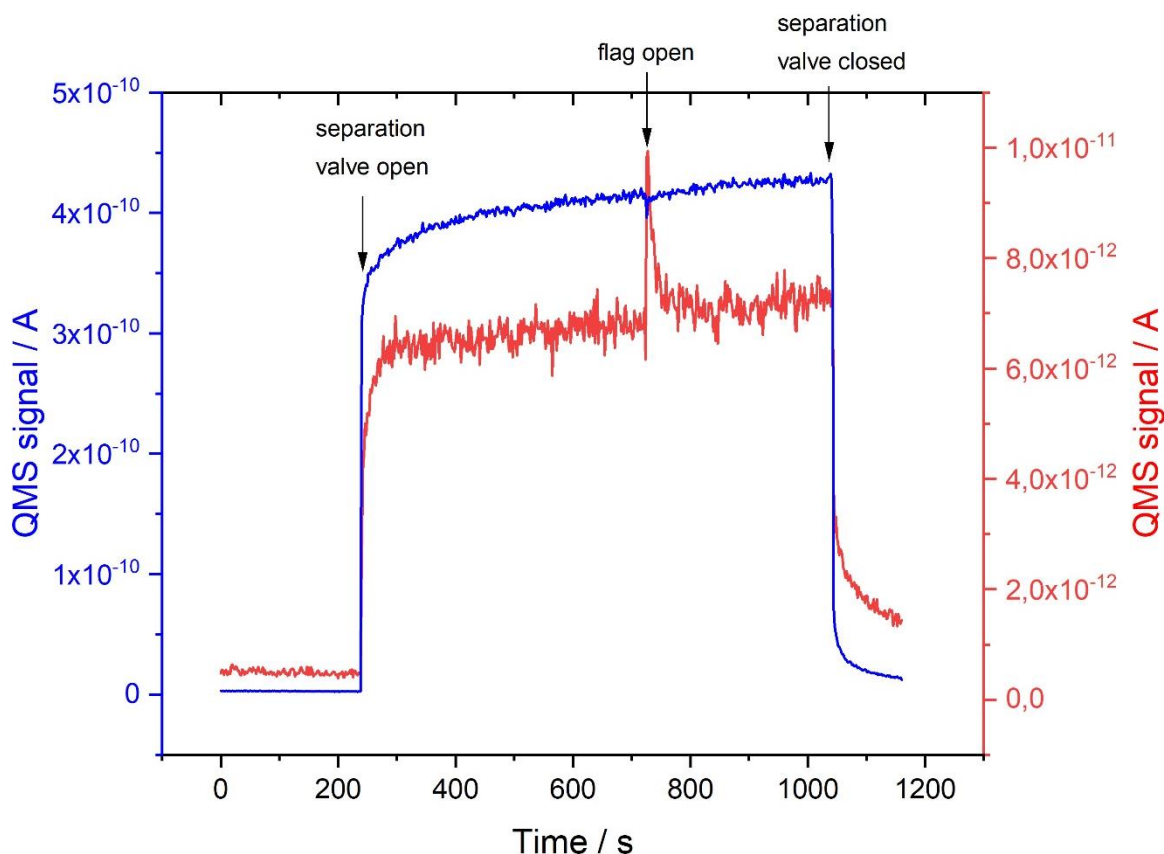


Fig. 3.15: QMS trace showing m/z 20 (blue) and m/z 22 (red) during the ^{18}O covered surface exposure to a MB of D_2^{16}O in He was leaked into the UHV chamber.

3.4 Summary

In short, a partially oxidised Cu(111) surface allows for facile O-H bond breaking in water molecules. The pre-dosed oxygen on the surface significantly reduces the activation barrier for the dissociation of water and also gets consumed in the reaction. The water dissociation process was observed to be almost barrierless because even water molecules from the UHV background easily dissociated on an oxygen covered surface. The facile water dissociation on partially oxygen covered surface compared to a bare Cu(111) surface is because the oxygen atom on the O-Cu(111) surface helps to abstract one of the hydrogen atoms from the water molecule resulting in the breaking of an O-H bond.

My study shows that when water molecules collide with the Cu(111), the pre-adsorbed surface oxygen atoms abstract one of the hydrogens from a water molecule causing

water to dissociate and form two hydroxyl adsorbates. This observation supports the published mechanism for the reaction between an oxygen atom adsorbed on a Cu(111) surface with a water molecule. At $T_s = 180$ K, the adsorbed hydroxyl species were found to be unstable thus leading towards their recombinative desorption as water molecules through disproportionation reaction. This way, the pre-dosed oxygen atoms were slowly replaced with the oxygen atoms from the incoming water molecules. During my initial experiments, the disproportionation reaction was not apparent from my experiments as the D_2O flux onto the surface was 1000 times larger with a MB compared to the flux of water molecules from the UHV background.

Chapter 4: Quantum state resolved D₂O reactivity on a clean Cu(111) surface

4.1 Overview

In the previous chapter, I have discussed the implications of introducing oxygen atoms on the Cu(111) surface prior to collision with water molecules. In this chapter, the focus will be to measure sticking coefficients of dissociative chemisorption of water molecules on a clean Cu(111) surface. Based on DFT calculations, Jiang and Fang reported an activation barrier of 1.5 eV for this reaction⁵⁰. One can overcome the barrier by either using translational or vibrational energy. I employed both these energies in order to obtain sticking probabilities from water dissociation on a bare Cu(111) surface. The translational energy was provided to the molecules by seeding in He and by heating the expansion nozzle up to 1050 K whereas, the vibrational energy was added by excitation of the antisymmetric O-D stretch normal mode by a resonant cw IR laser. It is important to note that heating the nozzle to 1050 K also provides vibrational energy to the molecules.

Water is a non-linear molecule and has 9 degrees of freedom in which 3 of them are vibrational degrees of freedom ($3N-6=3$, where N = number of atoms in the molecule) namely, symmetric- ν_1 , bending- ν_2 and asymmetric- ν_3 . All the three vibrational modes are IR active. A D₂O molecule belongs to the C_{2v} point group where ν_1 and ν_2 have the same symmetry, A₁ while ν_3 is of B₂ symmetry. It is categorized as asymmetric top molecule due to the three unequal moments of inertia it possesses. The rotational levels for this molecule can be expressed with J, total angular momentum quantum number and K_a and K_c which are the quantum numbers used to indicate how the rotational levels of the asymmetric top molecule relate to the rotational levels of a oblate symmetric top and prolate symmetric top molecule.

In this chapter, I used excitation of the D₂O molecules to the asymmetric O-D stretching mode near 2800 cm⁻¹ in order to measure the sticking probabilities for the dissociative chemisorption of the vibrationally excited water molecules on a Cu(111) surface. I chose to use D₂O in the state resolved experiments due to the presence of H₂O in air (~18

mbar) which would strongly absorb the IR laser radiation (100% absorption based on an IR absorption measurement performed for H₂O in air, which showed a 10% absorption in a beam path of 28 cm around 3756 cm⁻¹ (ν_3) through the 4 m beam path to the machine. Because of the low natural abundance ($\sim 2 \cdot 10^{-6}$ %) of doubly deuterated water, absorption of the laser radiation can be neglected.

4.2 Sticking coefficients measurements with RAIRS

Sticking probabilities for dissociative chemisorption of gas molecules on metal surfaces can be measured by using the K&W method described in Chapter 2. However, ground state water dissociation on a clean Cu(111) surface was predicted to have low sticking coefficients (< 1%) for $E_{\text{trans}} < 1$ eV, thus rendering the K&W method not sensitive enough for this study³⁵. Going above 1 eV would require the nozzle to be heated above 1050 K which in turn would increase vibrational energy in the molecules. As a solution, RAIRS was employed in this investigation to measure the sticking coefficients. Two advantages of using RAIRS for this measurement is that, (a) RAIRS can distinguish the OH product from molecular water and (b) RAIRS can measure a sticking coefficient in the order of 10^{-5} . On top of that, RAIRS can discern isotopologues on the surface, such as OH and OD thus, it can also be used to study the bond selective dissociation of HOD molecules. Morten Hundt, a doctoral student from our lab successfully performed quantum state resolved measurements of D₂O on a Ni(111) using AES. However, AES is an elemental measurement tool which measures O on the surface therefore, is not able to distinguish between OH(ads) and OD(ads) on the surface unlike RAIRS.

In order to obtain the sticking probability values, one needs to plot the hydroxyl coverage on the surface as a function of incoming water dose on the Cu(111) surface. The initial slope of the plot is the initial sticking coefficient of dissociative chemisorption of water molecules on the surface. The disproportionation reaction explained in Chapter 3 is negligible in the initial sticking coefficient measurement as we need two OH(ads) in close vicinity for the reverse of water dissociation to occur.

4.2.1 RAIRS absorption to absolute coverage

To calculate sticking coefficients of D₂O dissociation on a clean Cu(111) surface, I first had to calibrate the RAIRS absorption signal in terms of OD(ads) coverage. To do so, I exposed a clean Cu(111) surface to different doses of oxygen at two surface temperatures, $T_s = 300$ K or $T_s = 650$ K as shown in Table 1. Using Auger Electron Spectroscopy (AES), I then measured the O to Cu peak-to-peak Auger ratio signal at 520 eV for O and 920 eV for Cu, shown in Fig. 4.1, for each of the O₂ exposures and calibrated these measurements to the known saturation coverage of 0.5 ML of O on Cu⁵⁴. The saturation oxygen coverage was reported by Jensen and co-workers from nuclear reaction analysis (NRA) for a Cu₂O oxide with the “29” superstructure as 0.5 ± 0.05 ML⁵⁴.

Table 4 and Fig. 4.2 show oxygen uptake data measured for the two different surface temperatures ($T_s = 300$ K – blue squares and $T_s = 650$ K – red dots). Depositing O₂ at $T_s = 650$ K was reported by Therrien et al. to form the “29” superstructure of Cu₂O and I used this condition to obtain the AES O:Cu ratio which corresponds to 0.5 ± 0.05 ML⁵⁴. Since Jensen and co-workers used the AES peak-to-peak height ratio of O at 510 eV and Cu at 105 eV, I used only the reported O coverage at saturation, 0.5 ML to calibrate the O(OD) coverage following O₂(D₂O) exposure on the Cu(111) surface in my experiments⁵⁴.

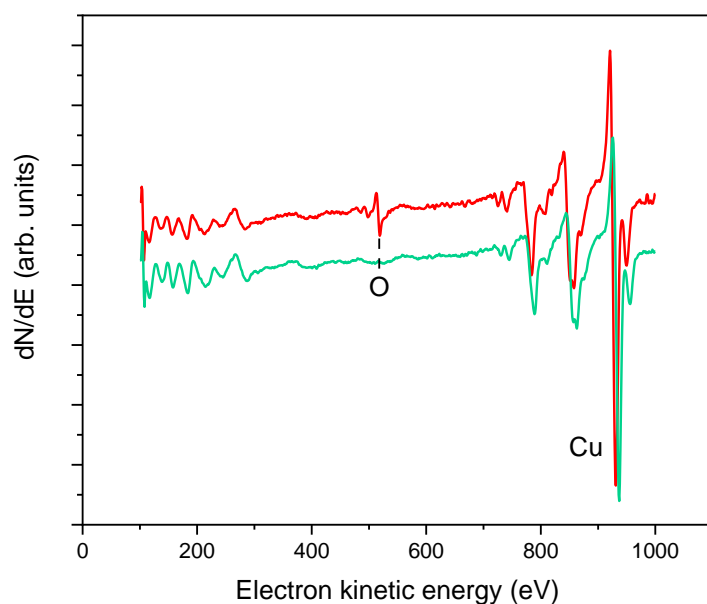


Fig. 4.1: Auger electron spectra measured from the Cu(111) surface. The green spectrum shows a clean Cu(111) surface after sputtering and annealing. The red spectrum was taken following surface exposure to 300 L of O₂ at T_s = 300 K.

Table 4 : Calibrating Auger signal to O coverage on the surface.

Experimental conditions used	Auger ratio	O coverage / ML
30L of O ₂ at Ts=300K	0,01	0,02
84L of O ₂ at Ts=300K	0,03	0,07
150L of O ₂ at Ts=300K	0,04	0,09
300L of O ₂ at Ts=300K	0,08	0,17
300L of O ₂ at Ts=650K	0,21	0,46
400L of O ₂ at Ts=650K	0,23	0,50
500L of O ₂ at Ts=650K	0,23	0,50

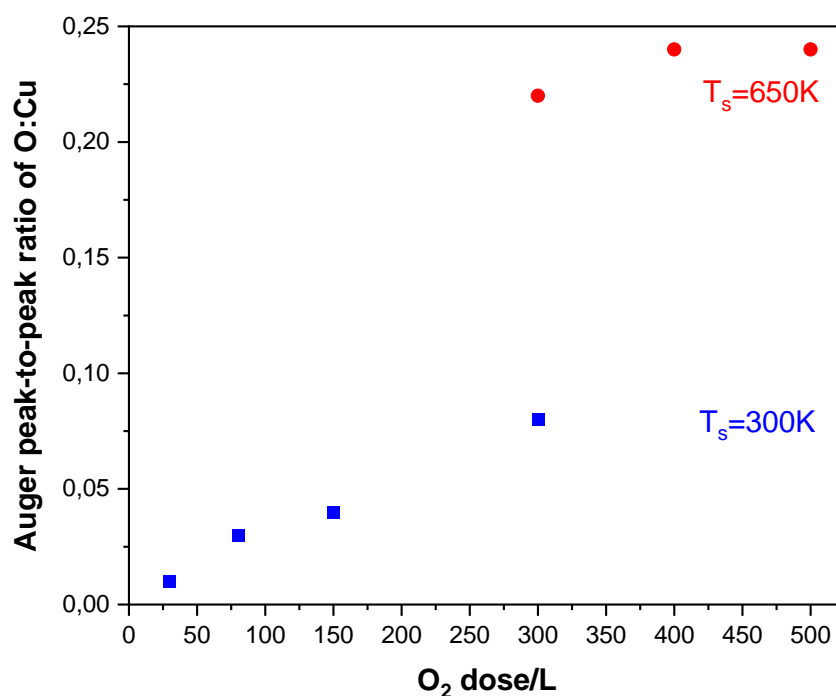


Fig. 4.2: O₂ deposition on a clean Cu(111) surface performed at two different surface temperatures followed by Auger signal measurements at 520 eV for O and 920 eV for Cu.

Now that we have calibrated the O/Cu AES peak-to-peak signal ratio in terms of surface coverage O(ads), the OD(ads) surface coverage can be obtained by calibrating the OD(ads) RAIRS absorption signal in terms of coverage with the calibrated O/Cu AES signal. To do that, I measured a RAIRS uptake curve for OD(ads) at 2689 cm⁻¹ using a gas mixture of 2% D₂O in He with $E_{kin} = 0.82$ eV and $T_s = 180$ K, followed by an Auger measurement as shown in Fig. 4.3. The peak absorption of the O-D stretch RAIRS signal at 2689 cm⁻¹ was then calibrated against the O coverage obtained from the calibrated AES detection. This allowed me to calibrate the OD RAIRS peak signal in terms of OD(ads) coverage by performing a least squares fit to the data points. The resulting slope is 35.82 ML/ RAIRS absorption signal $\pm 8\%$.

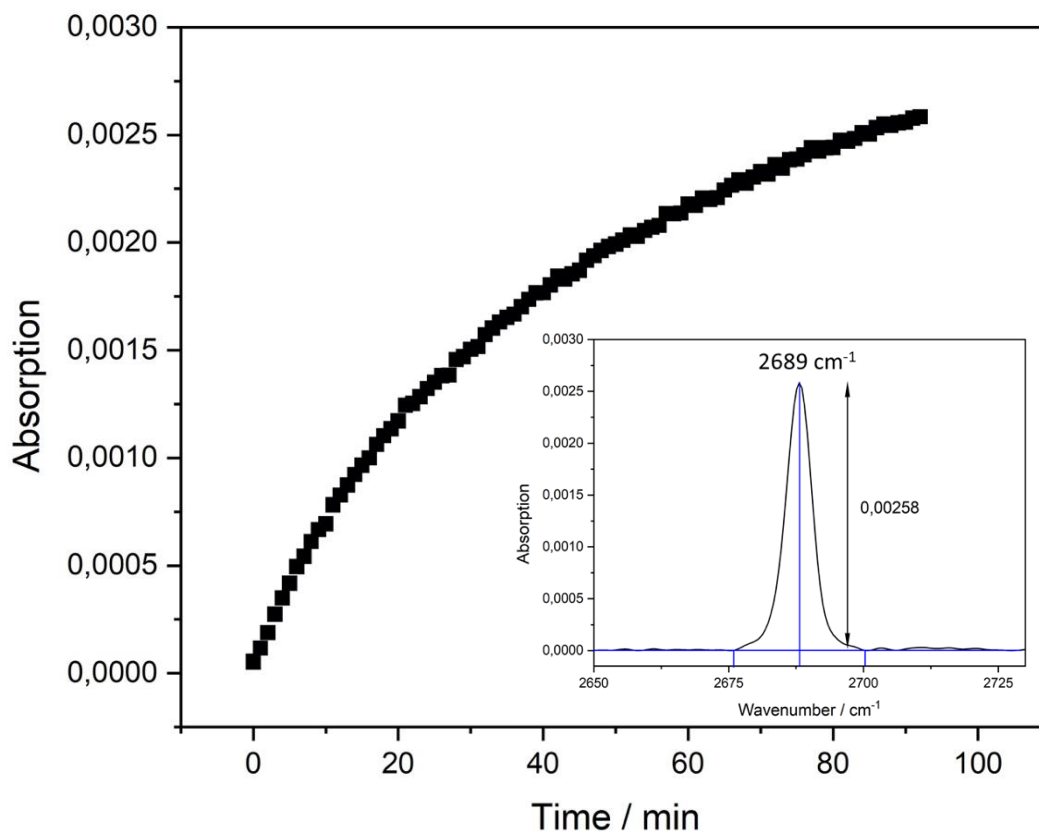


Fig. 4.3: RAIRS uptake curve of the O-D stretch at 2689 cm⁻¹ used for the calibration of RAIRS absorption to the OD(ads) coverage on the surface. Inset shows a RAIRS peak corresponding to the O-D stretch on a Cu(111) surface at T_s = 180 K after D₂O deposition with E_{kin} = 0.82 eV.

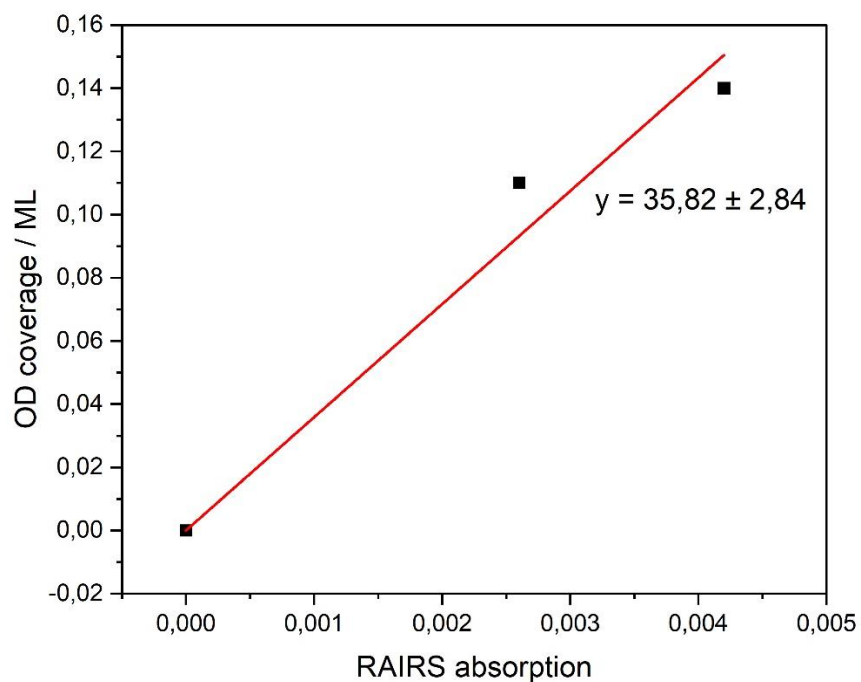


Fig. 4.4: Calibration of RAIRS absorption to OD coverage on a clean Cu(111) surface.

Below are the two steps involved in the conversion of the RAIRS peak absorption spectra to OD(ads) coverage on the surface.

RAIRS (absorption) ↔ **AES (O/Cu)** ↔ **Absolute coverage**

*Known coverage
from Cu₂O*⁵⁴

As mentioned at the beginning of this section, one needs both the product's coverage on the surface along with the dose of water molecules arriving on the surface to obtain the initial sticking coefficient for water dissociation. I have just explained how the coverage of OD(ads) can be obtained from the measured RAIRS absorption signal whereas the method used to identify the dose of water molecules arriving on the surface was shown in Chapter 2, section 2.2.3. The next section will focus on how the sticking probabilities were obtained from the OD(ads) coverage vs D₂O dose plot using Langmuir uptake fit.

4.2.2 S₀ obtained from OD(ads) coverage vs dose of water molecules

The following RAIRS measurements of the OD(ads) uptake were performed with an incident beam of 2% D₂O in He with E_{kin} of the deuterated water with E_{kin} = 0.82 or E_{kin} = 0.86 eV and a surface temperature of 180 K. During the experiment, the RAIRS absorption for OD(ads) was measured as a function of time while simultaneously monitoring the QMS signal for m/z 20 (D₂O). The RAIRS absorption signal was converted into the OD(ads) coverage in ML as explained in section 4.2.1. The dose in ML was calculated from equations 2.3 and 2.6. After that, Langmuir fits were used to obtain the initial sticking coefficients as shown in Fig. 4.5.

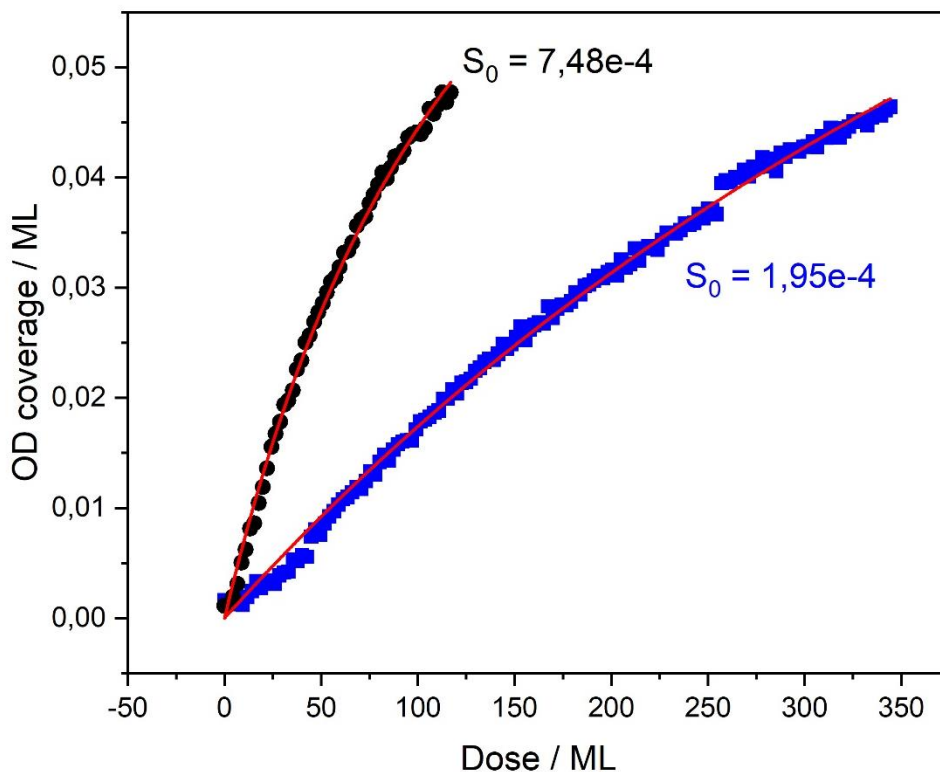


Fig. 4.5: OD uptake following D₂O dissociation with different E_{kin} on a clean Cu(111) surface at $T_s = 180$ K. Black – $E_{kin} = 0.86$ eV and blue – $E_{kin} = 0.82$ eV.

Fig. 4.5 above shows the OD surface coverage, θ_{OD} as a function of incident D₂O dose. The red lines are the fits of a Langmuir uptake model,

$$\theta_{OD} = \frac{A \cdot B \cdot Dose}{1 + B \cdot Dose} \quad (4.1)$$

to the data. The uptake model function above was derived from surface coverage-dependent water sticking probability shown below. Since each water molecule dissociates to form OD(ads) and D(ads), it will take up two adsorption sites on the surface.

$$S(\theta_{OD}) = S_0 \cdot (1 - \theta_{OD})^2 \quad (4.2)$$

S_0 is the initial sticking coefficient on a clean Cu(111) surface and the θ_{OD} is the surface coverage of the OD(ads). To include any further site blocking by each adsorbate, I used an

adjustable parameter λ to account for the effective number of sites blocked by each adsorbate. Now, the sticking probability equation above becomes

$$S(\Theta_{OD}) = S_0 \cdot (1 - \lambda\Theta_{OD})^2 \quad (4.3)$$

The time dependent coverage is related to the $S(\Theta_{OD})$ as following:

$$\frac{d\Theta_{OD}(t)}{dt} = f \cdot S(\Theta_{OD}) = f \cdot S_0 \cdot (1 - \lambda\Theta_{OD}(t))^2 \quad (4.4)$$

f is the flux of the MB in ML/s. Integrating the equation above will give us

$$\Theta_{OD}(t) = \frac{f \cdot S_0 \cdot t}{1 + \lambda \cdot f \cdot S_0 \cdot t} \quad (4.5)$$

This above equation can also be written as a function of dose, D which is the Langmuir uptake model used to fit the RAIRS uptake curves in Fig. 4.5.

$$\Theta_{OD}(D) = \frac{A \cdot B \cdot Dose}{1 + B \cdot Dose} = \frac{S_0 \cdot D}{1 + \lambda \cdot S_0 \cdot D} \quad (4.6)$$

Where

$A = 1/\lambda$ (the asymptotes of the uptake curves in Figure 7 i.e. saturation coverage)

$A \cdot B = S_0$

$$D = f \cdot t$$

t is the exposure time

From the fits in Fig. 4.5, the S_0 measured for D₂O with $E_{\text{kin}} = 0.82$ eV is 1.81×10^{-4} and for $E_{\text{kin}} = 0.86$ eV is 6.96×10^{-4} .

4.3 Laser-off results

The dissociative chemisorption of water molecules on a clean Cu(111) surface was predicted to be a reaction with barrier of approximately 1.5 eV⁵⁰. One can overcome this barrier through the addition of translational energy or vibrational energy to the incident water molecules. In this section, I have investigated the effect of increasing translational energy on the dissociation of D₂O molecules on a Cu(111) surface by increasing the nozzle temperature from $T_n = 300$ K to $T_n = 1050$ K and the results are presented in Fig. 4.6 below. It is important to note that by raising the nozzle temperature, I also introduce vibrational energy into the molecules. Table 5 shows the vibrational population fraction at different nozzle temperatures, calculated using the vibrational partition function as explained in Chapter 2 (section 2.3.4). The estimated vibrational energy in the water molecules are also shown in the table below.

Table 5: Vibrational population of D₂O molecules at the nozzle temperatures used for laser-off experiments.

		Vibrational state population					
		$\nu_1 = 1$	$\nu_2 = 1$	$\nu_2 = 2$	$\nu_3 = 1$	ground state	
T_n/K	E_{kin}/eV	2691.606 cm^{-1}	1190.790 cm^{-1}	2359.689 cm^{-1}	2799.758 cm^{-1}		E_{vib}/eV
300	0.28	0	0.003	0	0	0.997	0
900	0.75	0.013	0.125	0.022	0.011	0.828	0.041
1000	0.82	0.020	0.146	0.032	0.017	0.784	0.056
1050	0.86	0.024	0.157	0.038	0.021	0.760	0.064

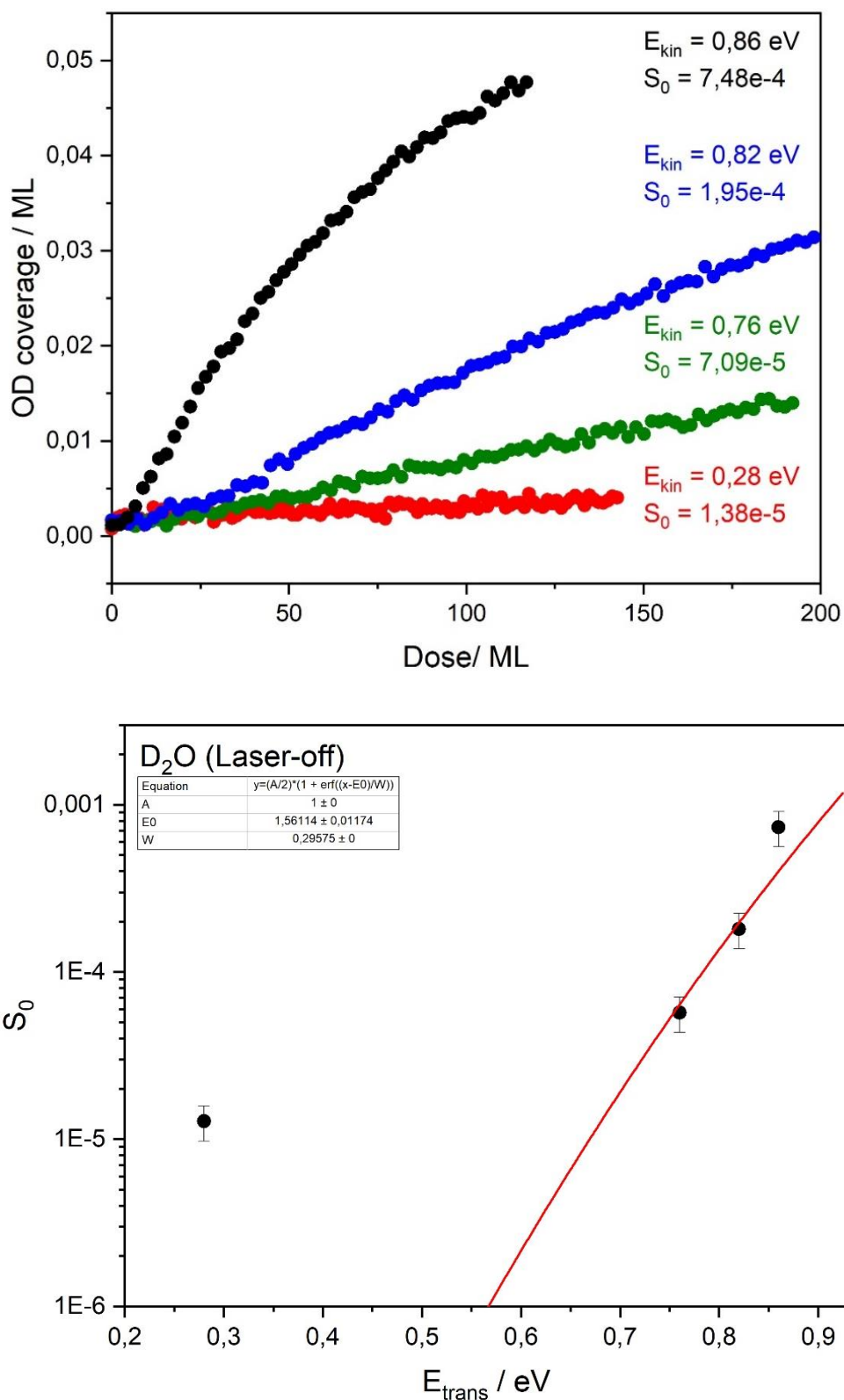


Fig. 4.6: Top- Uptake of OD(ads), measured with RAIRS, on the surface when 2% D₂O in He was incident on the surface at $T_s = 180$ K, with varying E_{kin} of incident D₂O molecules. Bottom- Sticking coefficients obtained from the OD uptake plotted as a function of translational energy of impinging water molecules in a logarithmic scale. The red line shows the S-shape curve fitting line for the sticking probabilities.

The data was fit using S-shape reactivity curve using the following function ⁷⁵

$$S_0(E, \nu) = \frac{A(\nu)}{2} \left(1 + \operatorname{erf} \frac{E - E_0^\nu}{W(\nu)} \right) \quad (4.7)$$

where $S_0(E, \nu)$ refers to the initial sticking coefficient, S_0 at translational energy, E and vibrational quantum state, ν . A is the asymptote of the reactivity and it was fixed to unity whereas E_0^ν is the average barrier height. A Gaussian distribution is assumed for the barrier heights with width, $W(\nu)$.

Water dissociation was observed to be enhanced by ~ 50 times with increasing translational energy from $E_{\text{kin}} = 0.28$ eV to 0.86 eV. As mentioned earlier, increasing the nozzle temperature in these experiments results in raising the thermal vibrational energy of the molecules alongside its kinetic energy. Thus, the enhanced water dissociation observed at higher translational energies in Fig. 4.6 may have contribution from the vibrationally excited molecules.

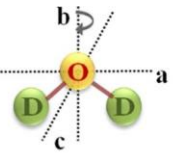
Furthermore, at the lowest translational energy, 0.28 eV, there is still a sticking coefficient for dissociative adsorption of D₂O on the Cu(111) although the energy is far below the predicted activation barrier. This observation may be attributed to oxygen contamination in the MB. In the previous chapter, I have demonstrated that oxygen atoms on the surface significantly lowers the barrier for water dissociation. Therefore, any oxygen in the MB arriving on the surface will dissociatively adsorb and the D₂O molecules which impinge on the oxygen adsorbates will be easily dissociated. The uptake of OD(ads) for the $E_{\text{kin}} = 0.28$ eV from Fig. 4.6- top is $\sim 1 \cdot 10^{-7}$ ML s⁻¹. Another explanation for the S_0 at the lowest translational energy is tunnelling effect as predicted by Zhang and co-workers based on their calculations where they observed a significant sticking probability for the ground state H₂O molecules in the low energy regions ³⁹.

The data point with the lowest E_{trans} was not considered for the S-curve fit since at this energy, water dissociated due to oxygen contamination on the surface. The oxygen

contamination contribution was corrected for the other initial sticking coefficients, i.e. $E_{\text{trans}} > 0.7$ eV.

4.4 Laser-on results

D₂O molecule comprises of 2 deuterium atoms with nuclear spin, $I_D = 1$ each and an oxygen atom with nuclear spin 0. The spin combinations thus gives six symmetric (*ortho*) and three antisymmetric (*para*) nuclear spin states for D₂O, Fig. 4.7⁷⁶. Based on Pauli's principle when the two bosons are interchanged, the total wavefunction of the molecule must remain symmetric. Therefore, the symmetric (*ortho*) nuclear spin of D₂O requires the rotational wavefunction to be symmetric whereas the antisymmetric (*para*) nuclear spin state requires rotational wavefunction to be antisymmetric in order for the total wavefunction to be symmetric. This brings us to the selection rule, when $K_a + K_c$ is even, we obtain states with *ortho* D₂O but when $K_a + K_c$ is odd, *para* D₂O is obtained for the vibrational ground state molecules.



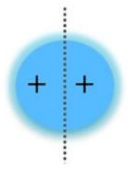
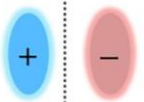
	Ψ_{spin}	Ψ_{rvib}
Ortho	$ 2, 2\rangle = 1, 1\rangle 1, 1\rangle$ $ 2, 1\rangle = \frac{1}{\sqrt{2}}(1, 0\rangle 1, 1\rangle + 1, 1\rangle 1, 0\rangle)$ $ 2, 0\rangle = \frac{1}{\sqrt{6}}(1, -1\rangle 1, 1\rangle + 2 1, 0\rangle 1, 0\rangle + 1, 1\rangle 1, -1\rangle)$ $ 2, -1\rangle = \frac{1}{\sqrt{2}}(1, -1\rangle 1, 0\rangle + 1, 0\rangle 1, -1\rangle)$ $ 2, -2\rangle = 1, -1\rangle 1, -1\rangle$ $ 0, 0\rangle = \frac{1}{\sqrt{3}}(1, -1\rangle 1, 1\rangle - 1, 0\rangle 1, 0\rangle + 1, 1\rangle 1, -1\rangle)$	<p style="text-align: center;">Symmetric $I=2, 0$</p> <p style="text-align: center;">Symmetric</p> <div style="text-align: center;">  </div> <p style="text-align: center;">$K_a + K_c = \text{even}$</p>
Para	$ 1, 1\rangle = \frac{1}{\sqrt{2}}(1, 0\rangle 1, 1\rangle - 1, 1\rangle 1, 0\rangle)$ $ 1, 0\rangle = \frac{1}{\sqrt{2}}(1, -1\rangle 1, 1\rangle - 1, 1\rangle 1, -1\rangle)$ $ 1, -1\rangle = \frac{1}{\sqrt{2}}(1, -1\rangle 1, 0\rangle - 1, 0\rangle 1, -1\rangle)$	<p style="text-align: center;">Anti-symmetric $I=1$</p> <p style="text-align: center;">Anti-symmetric</p> <div style="text-align: center;">  </div> <p style="text-align: center;">$K_a + K_c = \text{odd}$</p>

Fig. 4.7: Right- Symmetric and antisymmetric spin wavefunctions, Ψ_{spin} resulting from the combinations of the wavefunctions of the deuterium atoms while left- symmetry of ro-vibronic wavefunctions, Ψ_{rvib} . I refers to the total nuclear spin and m_I refers to the magnetic nuclear spin. Reproduced with permission from⁷⁶.

To report sticking coefficients for dissociative adsorption of water on the Cu(111) surface, one needs to know the fraction of ro-vibrationally excited D₂O molecules. As mentioned above, D₂O has two nuclear spin isomers, *ortho* and *para* with 2:1 nuclear spin statistical weight ratio. At zero Kelvin, only the lowest rotational state of *ortho* (0₀₀) and *para* water (1₀₁) are occupied and with increasing temperature, more rotational states are populated. The transition frequencies for R-branch excitation of the ν_3 mode from $v=0$ originating from the 5 lowest rotational states are shown in Table 6 below.

Table 6: The five lowest rotational level transitions for D₂O molecules.

Transition	$\tilde{\nu}$ (cm ⁻¹)	Spin isomer
R ₀₀ (0)	2799.75	Ortho
R ₀₁ (1)	2811.21	Para
R ₁₁ (1)	2808.76	Ortho
R ₁₀ (1)	2813.68	Para
R ₀₂ (2)	2821.67	Ortho

In my experiments, I used the *ortho* D₂O due to its higher statistical weight. The fraction of excited molecules in the different rotational states were obtained from the ratio of the asymptotes of the fluence curves measured at different nozzle temperatures. The method for fluence curves measurements has been explained in Chapter 2.

Fig. 4.8 shows the fluence curves measured at a nozzle temperature $T_n = 400$ K. Since I was exciting only the *ortho* D₂O molecules, I measured fluence curves for the three initial rotational states, $J_{K_a K_c} = 0_{00}$, 1_{11} and 2_{02} of *ortho* D₂O. From the measured fluence curves, I determined that 27% of the molecules in the MB are in the 1_{11} state - R₁₁(1) transition, 25% in the 0_{00} state - R₀₀(0) transition and 16% in the 2_{02} initial state - R₀₂(2) transition.

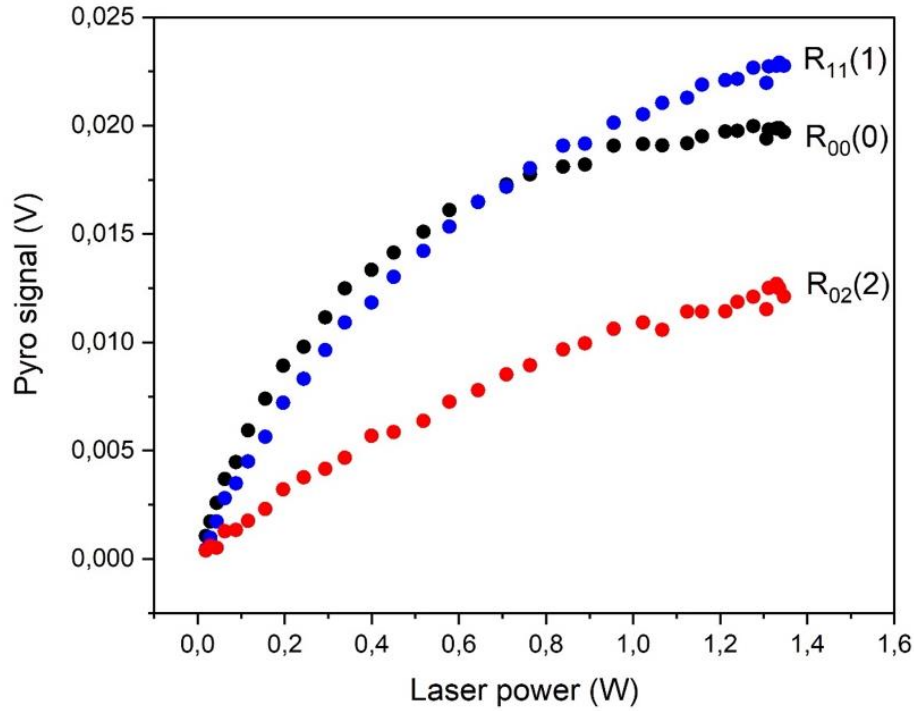


Fig. 4.8: Fluence curves measured for three lowest rotational transitions of ortho D₂O molecules.

To obtain the rotational temperature of the D₂O in the MB, one needs to compare the measured excited fractions to the calculated population as a function of rotational temperatures shown in Fig. 4.9. The relative population for the different rotational states is given by:

$$p(J_{K_A K_C}) = \frac{g_i \cdot (2J + 1) \cdot \exp\left(\frac{-E(J_{K_A K_C})}{kT}\right)}{Q_i(T)} \quad (4.8)$$

Where g_i refers to the effective nuclear spin weight, $2/3$ – *ortho* and $1/3$ – *para*. The i indicates either *ortho* or *para*. In order to obtain the relative population of the rotational levels, we need to divide by $Q_i(T)$, the rotational partition function. $Q_i(T)$ was obtained from the sum of 35 lowest J-levels from the energies presented in the work of Shirin *et al.*⁷⁷.

$$Q_i(T) = \sum_{J_K A K_C} g_i \cdot (2J + 1) \cdot \exp\left(\frac{-E(J_{K_A K_C})}{kT}\right) \quad (4.9)$$

Fig. 4.9 shows the calculated population of D₂O for the 3 lowest rotational states for *ortho* D₂O water. Comparing the data from Fig. 4.8 to Fig. 4.9, the rotational temperature at T_n = 400 K was obtained as 12 K ± 1 K. Since the J_{K_aK_c} = 1₁₁ depopulates slowly with increasing temperature, I chose this state to be excited for my study.

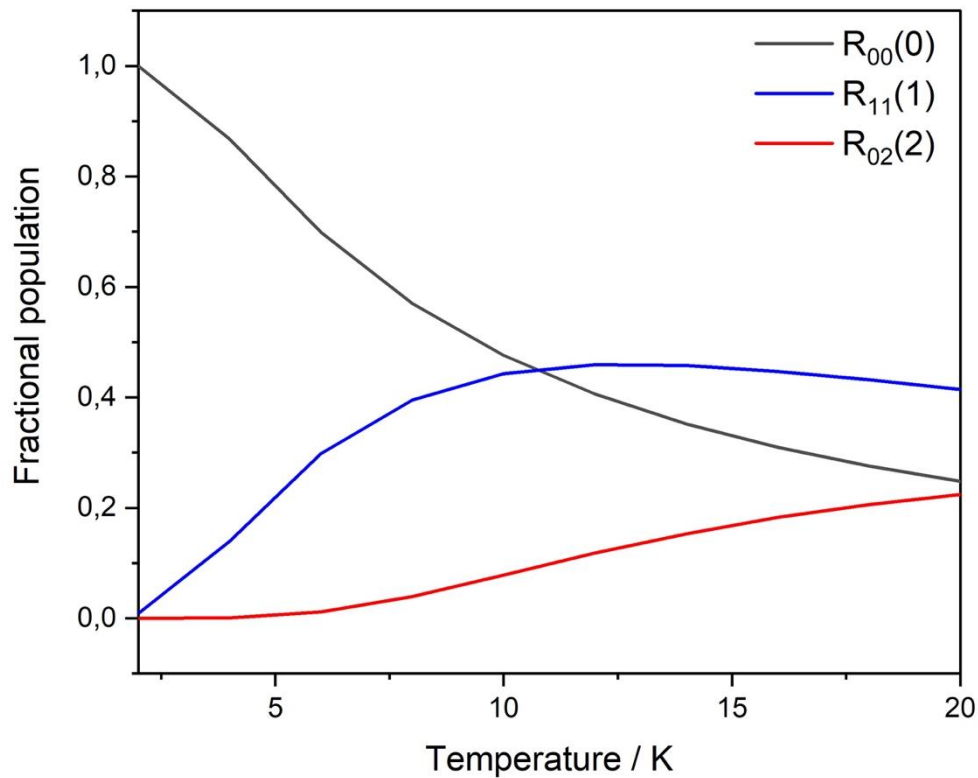


Fig. 4.9: Calculated fraction of *ortho* D₂O molecules as a function of rotational temperature for 3 lowest rotational energy levels, normalised to the maximum value.

It is not always feasible to measure fluence curves at high nozzle temperatures due to a decrease in signal to noise ratio of the pyroelectric detector signal for increasing nozzle temperature. This signal decrease is the result of the following factors:

- a) With increasing T_n , rotational temperature of the D₂O in the MB increases which reduced the population in each of the rotational states.
- b) Excitation become less efficient with increasing MB speed because the transit time, which is the time spent by molecules in the laser beam, is reduced.

In order to overcome this problem, an alternative method was used to determine the fraction of excited molecules at higher T_n . In this method, the pyroelectric detector signal was assumed to be proportional to the flux of excited molecules.

$$V(ref) = \alpha \cdot f_{exc}(ref) \cdot flux(ref) \quad (4.10)$$

$V(ref)$ is the pyroelectric detector signal for a reference state while α is the proportionality constant. Using the second method explained in Chapter 2 (refer section 2.3.4) for determining the rotational temperature, the fraction of excited molecules (f_{exc}) for the reference state is calculated. Once α is determined from equation 4.10, the excited fraction of the same state at different nozzle temperature can be found using the following equation 4.13. The excited fraction from $J_{K_a K_c} = 1_{11}$ for various nozzle temperatures are shown in Table 7.

$$f_{exc} = \frac{V(T_n)}{V(ref)} \cdot \frac{flux(ref)}{flux(T_n)} \cdot f_{exc}(ref) \quad (4.11)$$

Table 7: The excited fraction of D₂O molecules for $J_{K_a K_c} = 1_{11}$ at different nozzle temperatures.

T_n / K	$n_{v=0}$	$n_{J_{K_a K_c}=1_{11}}$	$f^{exc} (calc)$	f^{exc}
300	0.997	-	-	0.234
400	0.986	0.30	0.265	0.265
600	0.940	-	-	0.088
700	0.908	-	-	0.045
800	0.875	-	-	0.017

In order to calculate the state resolved sticking coefficients for the ν_3 excited state from the laser-on measurements, it is crucial to correct for the contribution of the thermally excited vibrational molecules (refer to Table 2 in section 2.3.4). This contribution drops out if we take the difference between the laser-on and laser-off reactivity since the state preparation changes only the $v=0$ population in the MB. Therefore, the state resolved reactivity for D₂O on a Cu(111) surface can be determined from the following equation ⁷⁵,

$$S_0^{\nu_3} = \frac{S_0^{laser\ on} - S_0^{laser\ off}}{f_{exc}} + S_0^{v=0} \quad (4.12)$$

where $S_0^{laser\ on}$ is the initial sticking coefficient obtained as a result of ro-vibrational excitation of molecules with laser and $S_0^{v=laser\ off}$ is the reactivity of D₂O molecules without laser excitation at the same incident translational energy. $S_0^{v=0}$ is the sticking probability of ground state D₂O molecules is the sticking probability of ground state D₂O molecules, in this case, it was taken as zero.

Fig. 4.10- top shows the OD(ads) uptake during the collision of 2% D₂O in He with a Cu(111) surface at $T_s = 180$ K, with vibrational excitation of the D₂O into ν_3 mode (R₁₁(1) transition). Various nozzle temperatures were used in these experiments and they are shown in Fig. 4.10-top along with the corresponding translational energies. The state-resolved sticking coefficients measured from Fig 4.10-top is presented in Fig.4.10-bottom. The values for S_0 were obtained using formula 4.12 and the plots were fit with the S-curve fit explained above, formula 4.7. The summary of the information obtained is presented in Table 8.

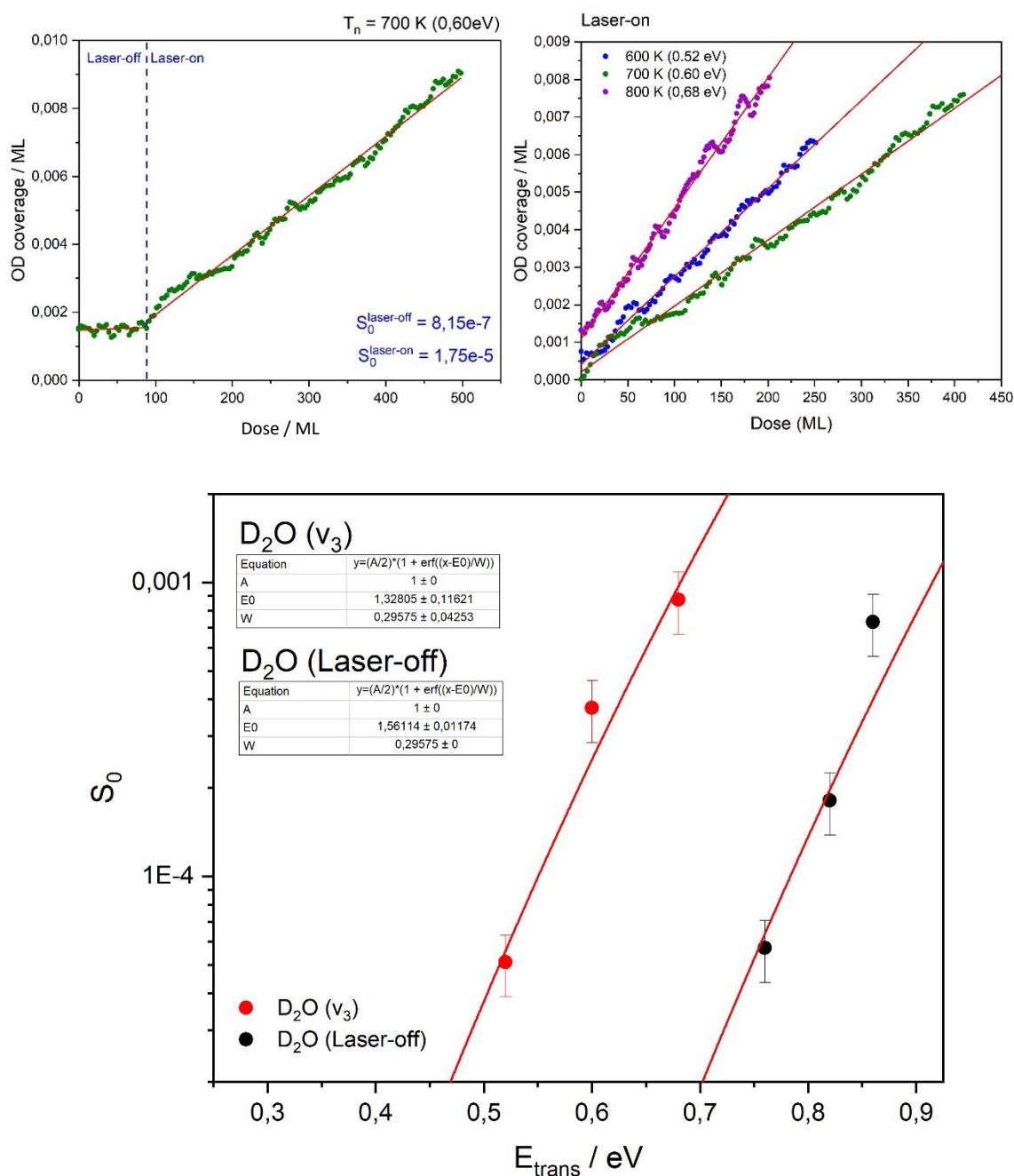


Fig. 4.10: Top, left- OD(ads) coverage as a function of D₂O dose on Cu(111) at $T_s = 180\text{ K}$ with laser on and off. Top, right- OD(ads) coverage for laser-on with increasing D₂O dose at various E_{kin} . Bottom-State-resolved dissociation probability for dissociative adsorption of D₂O on Cu(111) at $T_s = 180\text{ K}$ as a function of translational energy. The red lines are the S-curve fittings.

Table 8: Summary of the information obtained from the S-curve fittings in Fig.4.10.

State	E_0 /eV	E^{vib} /eV	η
Laser off	1.749 ± 0.015	0	-
ν_3	1.540 ± 0.075	0.35	0.70

Following the initial sticking coefficient measurements and the S-curve fittings, the vibrational efficacy was calculated. The vibrational efficacy, η gives the relative effect of the ν_3 vibrational energy for overcoming the reaction barrier compared to the same amount of translational energy and it is calculated as the following,

$$\eta^v = \frac{E_0^{v=0} - E_0^v}{E^{vib}} \quad (4.13)$$

where the $E_0^{v=0} - E_0^v$ is shift in translational energy between the S-curves for $v=0$ and ν_3 . E^{vib} is the vibrational energy of the incident molecules and corresponds to the energy of the infrared photons used for excitation of the ν_3 transition.

By using the shift in S-curves obtained from the laser-on and laser-off experiments, the η was calculated to be 0.70, lower than unity. A vibrational efficacy lower than unity shows that the translational energy is more efficient in promoting the reaction compared to the vibrational energy. According to the Polanyi rules, the value of 0.6 is an indication of an 'early barrier' reaction where vibrational energy is predicted to enhance the reaction less than the translational energy. A theoretical study by Jiang and co-workers predicted that ν_3 vibrational excitation of water molecules activates the dissociative adsorption of water more efficiently than the corresponding amount of translational energy, Fig. 4.11³⁵. The authors also predicted the symmetric stretch mode to show the strongest effect among the three vibrational modes, ν_1 – symmetric stretch mode, ν_2 – bending mode and ν_3 – asymmetric stretch mode.

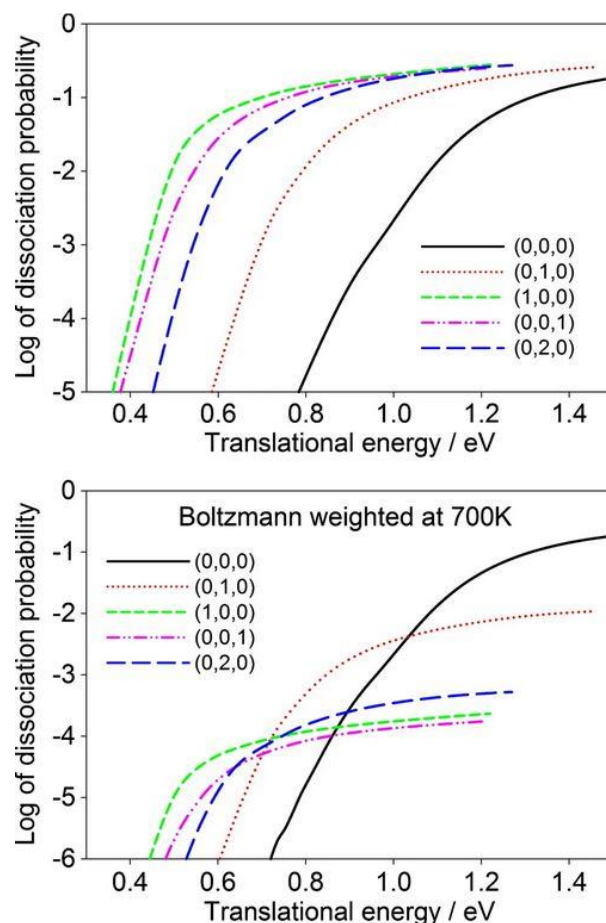


Fig. 4.11: Sticking probabilities predicted for different initial vibrational states of H₂O on Cu(111)-(v_1, v_2, v_3). The top figure is without Boltzmann weighting whereas the bottom figure includes Boltzmann weighting.

Another theoretical calculation performed for the dissociative chemisorption of H₂O on a Cu(111) included all the nine degrees of freedom in the quantum model³⁹. In this study, the authors predicted the vibrational energy to enhance the water dissociation better than the translational energy similar to the study by Jiang *et al.*^{35,39}. However, the asymmetric stretch mode and not the symmetric stretch mode of H₂O was found to promote the reaction better due to the strong coupling of the asymmetric stretch mode with the reaction coordinate.

One explanation for my sticking coefficient measurements to give a vibrational efficacy, $\eta < 1$ is that the S_0 of the laser-off experiments had significant contribution from the molecules in the higher vibrational states, shown in Table 5. Therefore, the S_0 measured for the laser-off, $E_{\text{tran}} > 0.7$ eV experiments are higher than the true value for ground state

molecules. This in turn shifted the laser-off S-curve to lower translational energy which results in an efficacy for the ν_3 lower than unity unlike the predictions from theoretical calculations³⁵.

4.5 Summary

Water dissociation on a clean Cu(111) surface was measured with and without laser excitation using RAIRS technique. The translational energy of the incident D₂O molecules was controlled by seeding in He gas at a seed ratio of approximately 2% and by heating of the expansion nozzle. Increasing the nozzle temperature also adds thermal vibrational energy to the incident D₂O(g) molecules. For the laser-on experiments, the D₂O molecules were excited to antisymmetric O-D stretch mode ν_3 via the R₁₁ rotational transition from $J_{K_a K_c} = 1_{11}$ state. The vibrational efficacy, η was determined to be 0.7 which indicates that the translational energy is more efficient in promoting water dissociation on a clean Cu(111) surface compared to vibrational energy. This is in contrast with theoretical predictions. The fact that the measured value of $\eta < 1$ might be due to the laser-off experiments having significant effect from the vibrationally excited molecules at higher nozzle temperatures.

Chapter 5: CH(ads) co-adsorbed with hydrogen atoms on a Pt(211) surface

5.1 Overview

Studying the formation and reactivity of small hydrocarbons on metal surfaces is important to understand better the catalytic processes such as the Fischer-Tropsch synthesis and the steam reforming reaction^{4,78}. Methylidyne (CH), the smallest hydrocarbon is a key intermediate in the Fischer-Tropsch synthesis and therefore has gained attention among surface scientists leading to studies on the reaction of methylidyne on metals such as Ni and Pt^{79,80}.

Previously, the group of Trenary studied the formation of methylidyne on a Pt(111) surface using infrared spectroscopy⁸⁰. They proposed three methods to form methylidyne on Pt(111) namely, i) thermal decomposition of diiodomethane (CH₂I₂), ii) decomposition of ethylene (C₂H₄) and iii) hydrogenation of carbon atoms. The third method, surface carbon hydrogenation, was performed by first exposing the surface to 2 L of ethylene (C₂H₄) at T_s = 750 K followed by surface exposure to 40 L of H₂ at T_s = 85 K. Upon surface heating to T_s = 200 K, a peak at 2974 cm⁻¹ assigned to the CH(ads) appeared in their RAIRS measurement as shown in Fig. 5.1. With increasing surface temperature, it was found that this CH(ads) peak red-shifted by 18 cm⁻¹ and then disappeared above T_s = 500 K. In Trenary *et al.*'s paper, the frequency shift was attributed to the coverage of the co-adsorbed hydrogen atoms because the frequency shift occurs only up to T_s = 400 K and above that, there was no significant frequency change. Since H₂ is known to desorb around 300 K from a Pt(111) surface, one expects no hydrogen to remain on the surface above T_s = 400 K hence, indicating that the presence of hydrogen was the reason the shift in the RAIRS C-H stretch frequency⁸⁰.

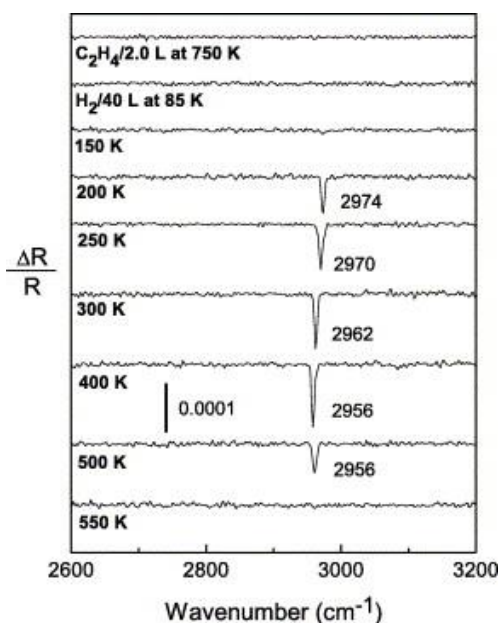


Fig. 5.1: RAIRS spectra from Trenary et al. showing formation of methylidyne (CH) from carbon atoms hydrogenation on a Pt(111) surface initially dosed with carbon atoms using ethylene (C_2H_4). The CH(ads) RAIRS peak shifted continuously from 2974 cm^{-1} to 2956 cm^{-1} with increasing surface temperature from $T_s = 200\text{ K}$ to $T_s = 500\text{ K}$. Reproduced with permission ⁸⁰.

In my study, I have used RAIR spectroscopy to investigate CH(ads) adsorbed on a stepped Pt(211) surface with co-adsorbed hydrogen atoms. As described in chapter 2, RAIRS is a highly sensitive tool to study adsorbates on metal surfaces because it does not only provide information on the type of adsorbates on the surface but in certain cases allows one to identify the adsorption site of a chemical species ⁸¹. Previously, it was shown by studies in our lab that RAIRS can identify the nascent products of methane dissociation on the steps and terraces of a Pt(211) surface, as shown in the Fig. 5.2 below ²⁴. It was observed that the RAIRS frequency of the methyl on the steps (2903 cm^{-1}) is blue shifted to the methyl on the terraces (2886 cm^{-1}).

The ability to observe site-selective dissociation with RAIRS has allowed us to have better control of the reactions occurring on the different sites of a surface. For example, in order to dissociate CH_4 only on the terraces of the Pt(211) surface, we first passivate the steps of the Pt(211) surface with CO(ads). The site blocking is confirmed by recording RAIRS peak for CO(ads) during the gas deposition on the surface. Once the RAIRS peak height for the CO(ads) on the step sites reaches a plateau, indicating saturation of the adsorbates on the steps, we stop the CO exposure. A continuous beam of CH_4 with $E_{kin} = 65\text{ kJ/mol}$ incident

energy is then deposited on the surface which results in methyl formation only on the terraces of Pt(211) since the steps are decorated with CO(ads) ⁴².

Apart from the site selective adsorption, RAIRS technique also allows one to gain insight into the chemical environment of the adsorbates of interest. For instance, Deng *et al.* detected the CH(ads) on a Pt(111) surface to interact with co-adsorbed hydrogen atoms which caused a continuous blueshift of the C-H stretch frequency with increasing H(ads) coverage ⁸⁰. Zhang et al. observed that the peak intensity of CO(ads) is closely related to the coverage of O(ads) on a Cu(111) surface using infrared spectroscopy ⁸². We can therefore agree that the RAIRS technique is able to provide detailed information about the adsorbates on a surface including interaction with neighbouring adsorbates.

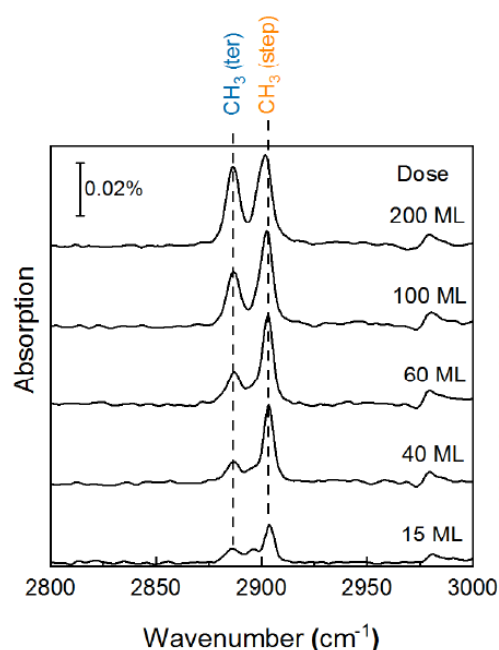


Fig. 5.2: RAIR spectra showing methyl formation on the steps and terraces of a Pt(211) surface recorded during surface exposure to a molecular beam of 3% CH₄ in He at T_s = 120 K with E_{kin} = 65 kJ/mol of incident energy. Reproduced from ⁴².

In this chapter, I will explore the properties of CH(ads) co-adsorbed with hydrogen/deuterium atoms on a Pt(211) surface. The RAIRS measurements recorded will be compared with the work of Trenary and his co-workers. On top of that, further studies performed to identify the origin of the CH(ads) will be presented.

5.2 RAIRS measurements of CH(ads) peaks

5.2.1 Three distinct CH(ads) absorption peaks

In our lab, methylidyne was prepared by thermal decomposition of methyl on a Pt(211) surface. Chemisorbed methyl was formed by methane dissociation using a molecular beam of 3% CH₄ in He with $E_{kin} = 65$ kJ/mol of kinetic energy incident on a Pt(211) surface at $T_s = 150$ K. At this incident energy, methyl, CH₃(ads) was produced on both the steps and terraces of the Pt(211) surface as observed in the RAIR spectra at 2901 cm⁻¹ and 2886 cm⁻¹, respectively - Fig. 5.3 (a). The assignment of these peaks are explained in detail in Gutiérrez-González's paper ²⁴.

Heating the surface covered with methyl to $T_s = 250$ K caused the removal of the CH₃(ads) peaks indicating recombinative desorption and/or thermal decomposition of the methyl species - Fig. 5.3 (c). In the same spectrum, there is an appearance of a C-H stretch peak at 2972 cm⁻¹ assigned to the CH(ads) formed from the decomposition of the methyl species. This peak appears at a similar frequency as observed by Trenary et al. for the CH₃(ads) on a Pt(111) surface - Fig. 5.1. In the next immediate spectrum, heating the surface to $T_s = 310$ K shows a reduction in the intensity of this peak and the emergence of a novel peak at 2962 cm⁻¹ - Fig. 5.3 (d). Continuous surface heating in steps to $T_s = 330$ K and 350 K produced another C-H stretch peak at 2951 cm⁻¹ Fig. 5.3 (e-f). Table 9 summarizes the vibrational frequencies observed and the corresponding adsorbates.

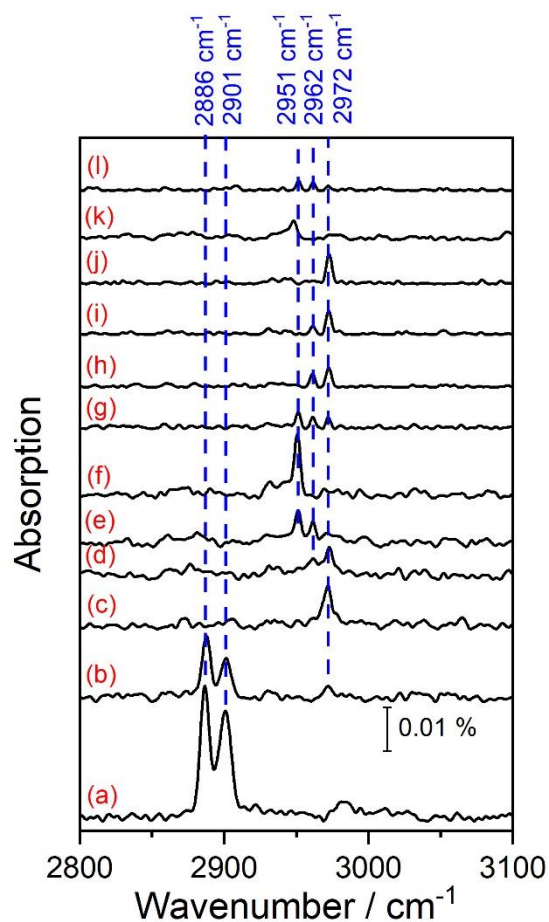


Fig. 5.3: (a) RAIR spectrum following dissociation of CH_4 molecules on a Pt(211) surface at $T_s = 150$ K with $E_{kin} = 65$ kJ/mol of incident energy. (b) After annealing the surface at $T_s = 230$ K for 2 minutes and then cooling to $T_s = 150$ K prior to RAIRS measurement. Similar procedure was used for (c) to (f) but at different annealing T_s - (c) $T_s = 250$ K, (d) $T_s = 310$ K, (e) $T_s = 330$ K and (f) $T_s = 350$ K. When all the H atoms on the surface were removed after heating the surface to $T_s = 350$ K, the surface was exposed to (g) 0.5 L, (h) 1.0 L, (i) 1.8 L, (j) 2.3 L of D_2 at $T_s = 150$ K. (k) Annealing surface once again to $T_s = 350$ K and (l) 0.5 L of D_2 deposition at $T_s = 150$ K.

Table 9: Assignment of RAIRS peaks observed in Fig. 5.3.

Frequencies / cm^{-1}	Assignments
2886	$\text{CH}_3(\text{ads})$ on terraces
2901	$\text{CH}_3(\text{ads})$ on steps
2951	CH(ads)
2962	
2972	

In order to test if the three CH(ads) absorption peaks observed in Fig. 5.3 (c-f) are associated with the changing surface hydrogen atoms coverage as reported by Trenary's group as in Fig. 5.1, I heated the surface in steps to $T_s = 350$ K and annealed for 2 minutes to desorb the hydrogen atoms on the surface, Fig. 5.3 (f). The TPD traces in Fig. 5.4 show deuterium desorbing from the steps and terraces of the Pt(211) surface and the D_2 doses used can be directly compared to the RAIRS spectra in Fig. 5.3. Following surface annealing at $T_s = 350$ K, an apparent shift appears in the RAIRS absorption peak from 2972 cm^{-1} to 2951 cm^{-1} . By slowly increasing the deuterium coverage on the surface from 0.5 L to 2.3 L, shown in Fig 5.3 (g-j), the most blue-shifted peak at 2972 cm^{-1} was restored. Reheating the surface to $T_s = 350$ K shifted the CH(ads) peak back to 2951 cm^{-1} , Fig. 5.3 (k) and redepositing 0.5 L of D_2 on the surface again caused all the three peaks to be visible. In short, the surface hydrogen/deuterium coverage plays a role in the appearance and disappearance of the three discrete CH(ads) peaks.

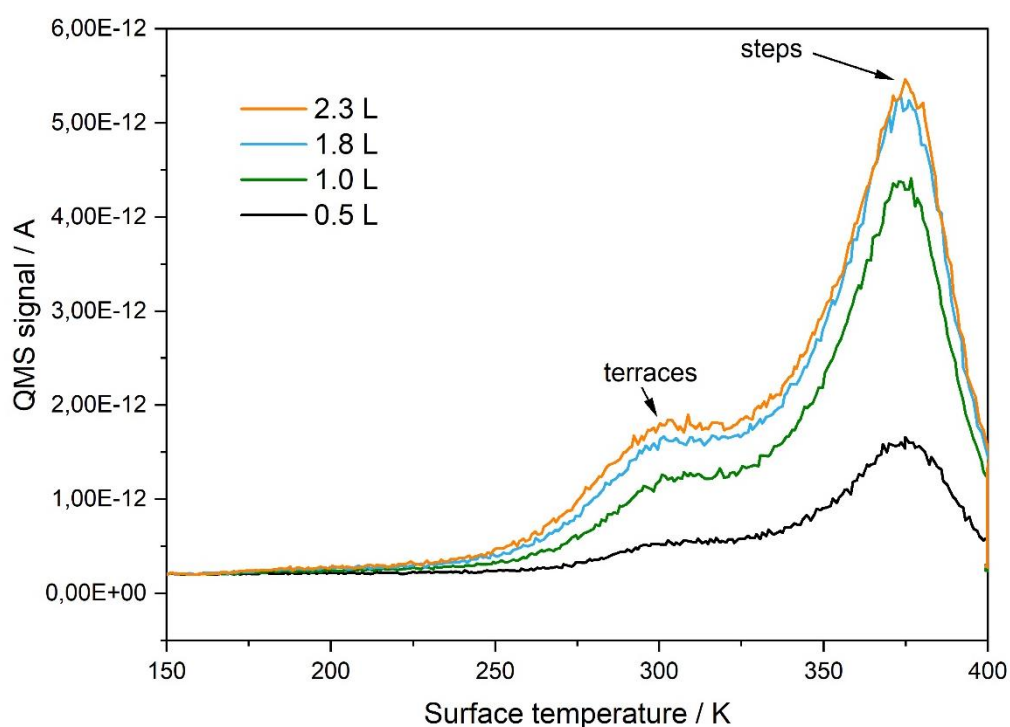


Fig. 5.4: TPD traces of D_2 desorption from the Pt(211). The surface was exposed to varying doses of D_2 followed by surface heating from $T_s = 150$ K to $T_s = 400$ K with a 2 K/s heating ramp which caused desorption of deuterium molecules from the steps and terraces of Pt(211).

Although the relative intensity of the three peaks can be attributed to the varying hydrogen/deuterium coverage on the surface, the three distinct frequencies of the CH(ads) with different amounts of co-adsorbed hydrogen is strikingly different from what Trenary and his co-workers reported for CH(ads) on a Pt(111) surface. They observed what appears with $E_{\text{kin}} = 65$ kJ/mol of incident energy to be a continuous shift in C-H stretch frequency from 2974 cm^{-1} to 2956 cm^{-1} for CH(ads) adsorbate with decreasing hydrogen coverage on the Pt(111) surface. Therefore, the surface structures must be responsible for the difference in the RAIR. Unlike a flat Pt(111) surface where all surface atoms are equivalent, the Pt(211) surface has three different surface sites with different activation barriers for reactions. These reactive sites are labelled as steps (S), terraces (T) and corners (C) as shown in Fig. 5.5.

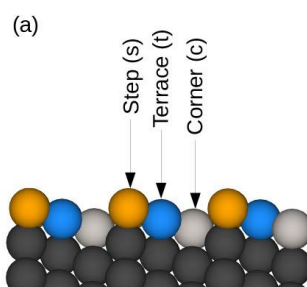


Fig. 5.5: A schematic showing the side view of a Pt(211) surface where the three adsorption sites are visible. Reproduced with permission from ⁸¹.

When the same experiments were performed with incident CD_4 molecules instead of CH_4 , as shown in Fig. 5.6 below there was again a clear transfer of intensity between the three CD(ads) peaks measured at 2217 cm^{-1} , 2210 cm^{-1} and 2201 cm^{-1} . $\text{CD}_3(\text{ads})$ appears to be slightly more stable than $\text{CH}_3(\text{ads})$ indicated by the fact that the most blue-shifted CD(ads) peak appeared only after surface heating to $T_s = 250$ K unlike the CH(ads) which already appeared at $T_s = 230$ K – Fig. 5.3(b). This may be due to kinetic isotope effect where more energy is required to break the C-D bonds in the $\text{CD}_3(\text{ads})$ since the zero-point energy for C-D is lower than a C-H bond.

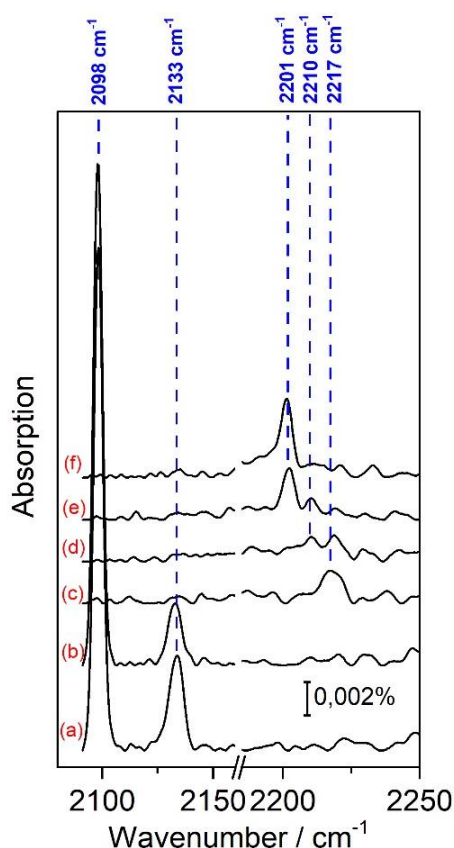


Fig. 5.6: RAIR spectra showing the dehydrogenation of $CD_3(ads)$ on steps - 2133 cm^{-1} and terraces - 2098 cm^{-1} into $CD(ads)$ and the three discrete $CH(ads)$ peaks shifting with increasing surface temperature. (a) After exposure of 2% CD_4 in He at $T_s = 150\text{ K}$ and $E_{kin} = 72\text{ kJ/mol}$, there was CH_3 on the steps and terraces of the Pt(211) surface. (b) Surface was briefly annealed to $T_s = 230\text{ K}$ for 2 minutes and cooled down to $T_s = 150\text{ K}$ before recording RAIRS. This step was repeated but the surface was heated to different surface temperatures - (c) 250 K, (d) 310 K, (e) 330 K and (f) 350 K.

5.2.2 Why three discrete CH(ads) peaks?

As described in the previous section, RAIRS is able to distinguish between adsorbates on the different surface sites. Therefore, the first hypothesis formulated to explain the three CH(ads) RAIRS peaks was that each peak corresponds to a different adsorption site on the Pt(211) surface. If this is true, then one must be able to reproduce the peaks by saturating the most stable site first with CH(ads) followed by the next stable site and the next. This hypothesis was then tested by continuously exposing the Pt(211) surface at $T_s = 380\text{ K}$ to a beam of 3% CH_4 in He with $E_{kin} = 65\text{ kJ/mol}$ of incident energy, Fig. 5.7. The surface temperature used in this experiment was deliberately placed at the peak desorption temperature of H_2 to remove any H atoms coming from the dehydrogenation of methane

molecules, through recombinative desorption. This step is important as it ensures no interaction between the co-adsorbed H atoms and the methylidyne on the surface during the experiment.

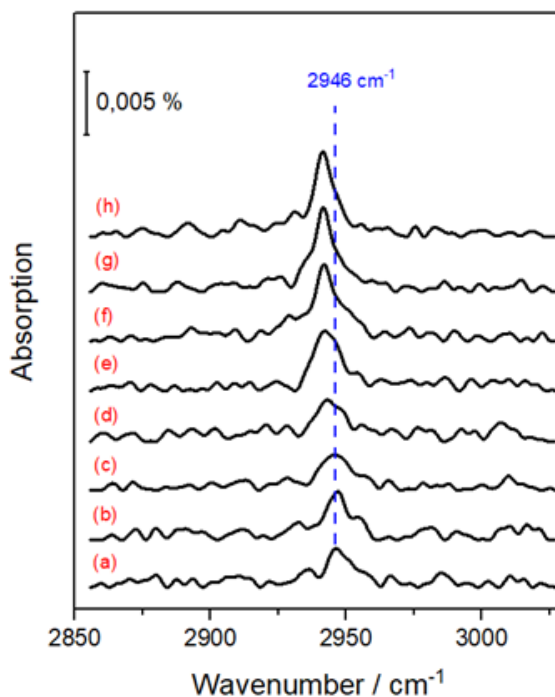


Fig. 5.7: RAIRS spectra showing the uptake of CH(ads) with time, where time increases from bottom to top. Every RAIRS spectrum was taken following an additional of 0.4 L of methane exposure at $T_s = 380$ K with $E_{kin} = 65$ kJ/mol incident energy - (a) 0.4 L, (b) 0.8 L, (c) 1.2 L, (d) 1.6 L, (e) 2.0 L, (f) 2.4 L, (g) 2.8 L and (h) 3.2 L.

Fig. 5.7 shows only a single peak near 2946 cm^{-1} . This shifts slightly to the red with increasing CH(ads) coverage but there is no evidence for the formation of any other peaks, Fig. 5.7 (g-h). Since we still observe a single peak for CH(ads) after saturation as shown in Fig. 5.7 (f-h), it can be concluded that the three CH(ads) peaks were not the result of methylidyne adsorbed in three different adsorption sites on the Pt(211).

DFT calculations predict that the CH(ads) and H(ads) adsorb on the steps of Pt(211) forming a row of adsorbates along the steps of the surface⁸¹. The CH(ads) prefers to adsorb in a threefold hollow site between two step atoms and one terrace atom (sst)⁸¹. The H(ads) adsorbates instead prefer the bridge site between two step atoms (ss). The restricted motion of hydrogen atoms in one dimension allows only three varying hydrogen environments in the

immediate vicinity of a CH(ads) namely zero hydrogen (0H), 1 hydrogen (1H) and 2 hydrogen (2H) atoms adjacent to a CH adsorbate. This brings us to our second hypothesis which is that each of the CH(ads) peak observed in the RAIR spectra correspond to a CH adsorbate surrounded by a specific number of hydrogen atom(s), 0H, 1H or 2H as shown in Fig. 5.8.

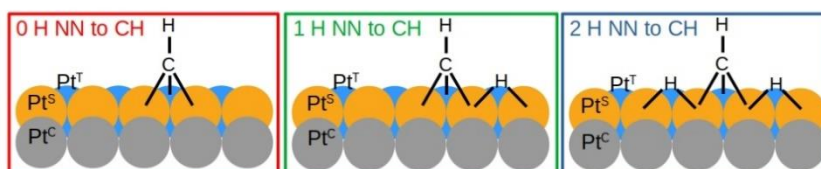


Fig. 5.8: Schematic diagram showing the adsorption of CH(ads) on the sst sites and H(ads) on the ss sites of a Pt(211) surface. Reproduced with permission from ⁸¹.

This hypothesis was further investigated with density functional theory (DFT) calculations performed by our collaborator, Prof. Fabio Busnengo in which the CH(ads) species was placed near varying neighbouring hydrogen atoms- 0H, 1H, 2H, 3H, 4H or 5H. Vibrational frequencies for CH(ads) in the different hydrogen environments were computed and interestingly, three different frequencies were obtained, 3027 cm^{-1} , 3036 cm^{-1} and 3041 cm^{-1} assigned to CH(ads) with 0H, 1H or 2H nearest neighbour ⁸¹. It is known that the DFT calculations typically predict much higher frequencies compared to experimental vibrational frequencies ⁸³. Nevertheless, the relative frequencies predicted were found to be more reliable ⁸⁴. The DFT predicted vibrational frequencies for CH(ads) are 14 cm^{-1} apart between two of the extreme values and my experimental data shows a difference of 21 cm^{-1} between the maximum and minimum frequency. Since anharmonic effects were not included in the DFT calculations, a better comparison will be between the vibrational frequencies of the CD(ads) adsorbates. Theoretical calculations predict a 11 cm^{-1} difference whereas RAIR spectra in Fig. 5.6 shows a 16 cm^{-1} of difference between the two most extreme CD(ads) absorption peaks ⁸¹. In this case, the DFT calculations have a closer resemblance to the vibrational frequencies measured experimentally.

Based on the DFT calculations, the three peaks observed in the RAIRS spectra in Fig. 5.3 can be assigned. The peak at 2951 cm^{-1} is assigned to the methylidyne with 0H in its vicinity, 2962 cm^{-1} to CH(ads) with 1H nearest neighbour and 2972 cm^{-1} to 2H nearest neighbour. Besides DFT, one can also assign the methylidyne peaks to the corresponding hydrogen environments based on the hydrogen coverage on the surface. Since heating the surface to $T_s = 350\text{ K}$ removes adsorbed hydrogen atoms, the single peak observed at 2951 cm^{-1} can be expected to appear in a condition where there is 0H atom in its vicinity. The most blue-shifted CH(ads) peak must belong to the CH(ads) with maximum number of neighbouring hydrogen atoms, 2H since we observe this peak immediately following the dehydrogenation of methyl species on the step and terraces. The RAIRS peak in between these extremes therefore could be predicted to belong to the CH(ads) with 1H nearest neighbour.

5.2.3 H-D isotope exchange on the surface

Watson *et al.* observed hydrogen-deuterium exchange between methylidyne, CH(CD) adsorbed on a Pt(110)-(1x2) surface and $D_2(H_2)$ gas molecules⁸⁵. They report a facile exchange between $D_2(\text{gas})$ and CH(ads) via Langmuir-Hinshelwood reaction especially at surface temperatures $350\text{ K} - 450\text{ K}$, to produce CD(ads) and HD(gas)⁸⁵.

In my experiments, I also observed a similar behaviour between CH(ads) and D_2 gas molecules. Fig. 5.9 shows an experiment where methane molecules were collided with a clean Pt(211) surface at $T_s = 300\text{ K}$ with $E_{\text{kin}} = 65\text{ kJ/mol}$ resulting in a single RAIRS peak at 2970 cm^{-1} , Fig. 5.9 (a). Heating the surface caused $D_2(\text{g})$ desorption and the CH(ads) peak to red shift, Fig. 5.9 (b). Incremental deposition of deuterium caused the recovery of the peak at 2790 cm^{-1} . Once again heating the surface to $T_s = 350\text{ K}$ produced the most red shifted peak at 2948 cm^{-1} but this time, another peak also appeared, Fig. 5.9 (g). The new peak appeared in the C-D stretch region at 2198 cm^{-1} and is assigned to the CD(ads) with zero deuterium atom nearby. Redepositing 0.5 L of D_2 caused the three CH(ads) absorption peaks to reappear shown in Fig. 5.9 (h) and at the same time, there are two other peaks observed at 2198 cm^{-1} and 2210 cm^{-1} assigned to CD(ads) with zero and one adjacent hydrogen atom, respectively. The lost intensity of the CH(ads) peaks in Fig. 5.9 (g-h) is attributed to the formation of CD adsorbates on the surface through H-D isotope exchange.

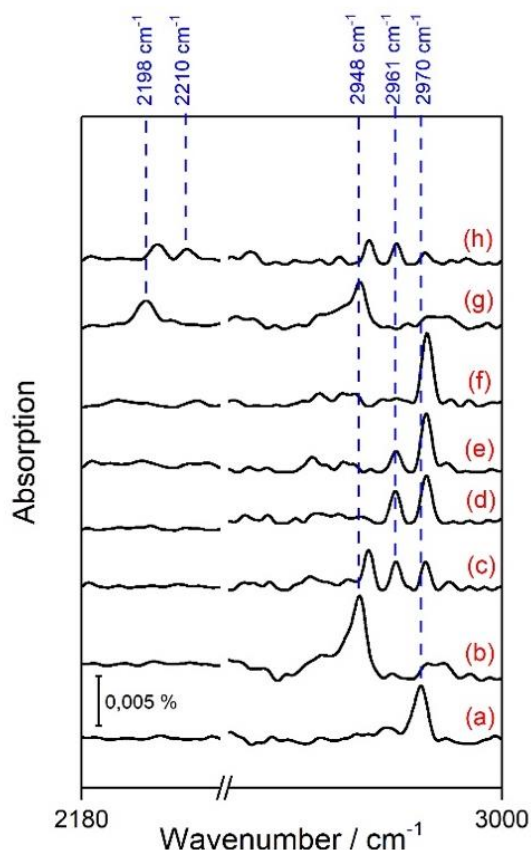


Fig. 5.9: RAIR spectra showing C-H stretch and C-D stretch regions during exposure to D_2 on a Pt(211) surface covered with CH(ads). (a) A RAIR spectrum taken after 3% CH_4 in He with $E_{kin} = 64$ kJ/mol deposition on a Pt(211) surface at $T_s = 300$ K. (b) After heating surface to $T_s = 350$ K which removed surface hydrogen atoms. Then the surface was exposed to varying doses of D_2 – (c) 0.5 L, (d) 1.0 L, (e) 1.8 L and (f) 2.3 L at $T_s = 150$ K. (g) Surface was again annealed at $T_s = 350$ K and (h) exposed to 0.5 L of D_2 at $T_s = 150$ K.

5.3 Origin of the CH(ads): steps and/or terraces?

After assigning the three CH(ads) peaks to different hydrogen environments, the next step is to identify where the methylidyne is originating from. As mentioned above, in this study, methylidyne was formed on the Pt(211) surface through thermal decomposition of the methyl species which was initially deposited on the steps and terraces of the surface. Did both the CH_3 (steps) and CH_3 (terraces) contribute to the methylidyne observed or only one of the adsorption sites did? Two experiments were performed to try to answer this question. The results are shown in Fig. 5.10.

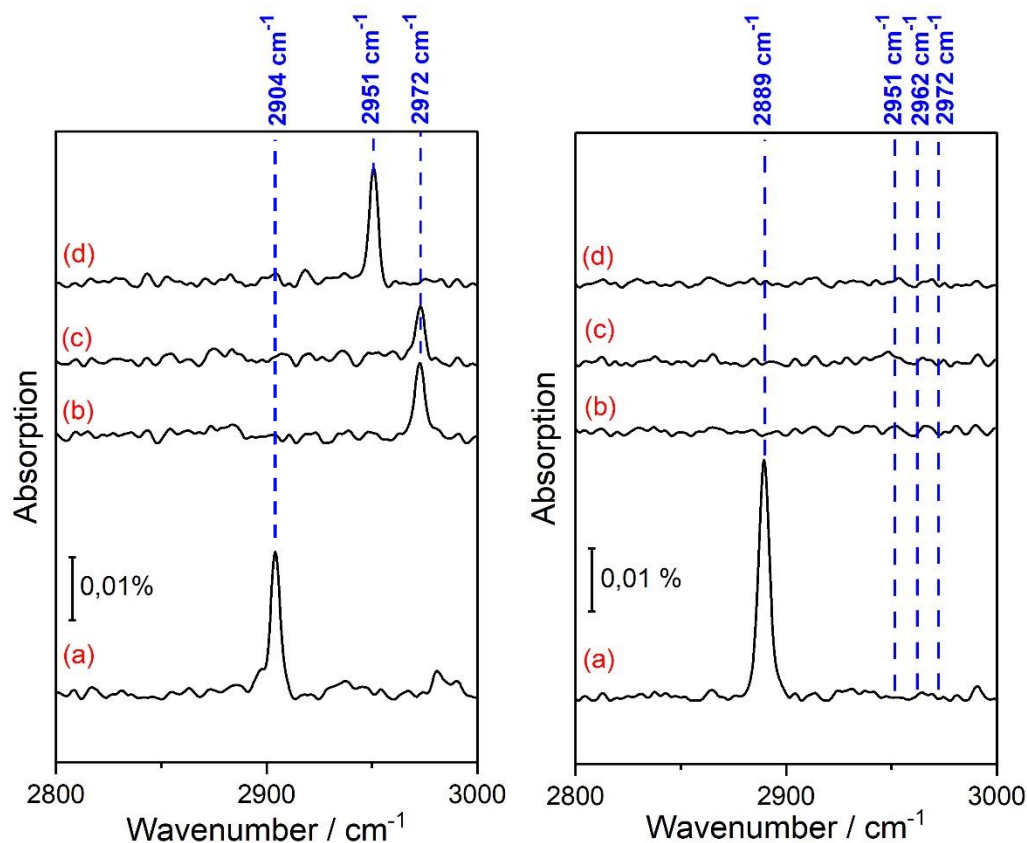


Fig. 5.10: Left panel- (a) RAIR spectrum of methane deposition with $E_{kin} = 41$ kJ/mol at $T_s = 120$ K resulting in the formation of methyl on steps of Pt(211) observed at 2904 cm⁻¹ followed by surface heating to (b) $T_s = 250$ K, (c) 300 K and (d) 350 K. Right panel- (a) RARS spectrum after dissociating CH₄ with the 65 kJ/mol incident energy on a Pt(211) at $T_s = 120$ K – the step sites of the Pt(211) surface was previously passivated with deuterium atoms. After heating the surface to (b) $T_s = 250$ K, (c) $T_s = 300$ K and (d) $T_s = 350$ K.

Based on the different dissociation barriers for methane on the steps (42 kJ/mol) and terraces (84 kJ/mol), I was able to study the origin of the methylidyne species by controlling the incident energy of methane molecules⁴⁹. The measurement in the left panel of Fig. 5.10 was performed by colliding a molecular beam of 3% CH₄ in He on a Pt(211) surface with $E_{kin} = 41$ kJ/mol at $T_s = 120$ K which produced methyl only on the steps of the Pt(211) at 2904 cm⁻¹. Following that, the surface was heated to $T_s = 250$ K- left panel of Fig. 5.10 (b) which produced CH(ads) at 2972 cm⁻¹, previously assigned to CH(ads) with 2 adjacent hydrogen atoms. Additional surface heating to $T_s = 300$ K and then to $T_s = 350$ K resulted in the replacement of the 2972 cm⁻¹ peak with 2951 cm⁻¹ absorption peak, assigned to CH(ads) with OH nearby. The peak near 2960 cm⁻¹ assigned to CH(ads) with 1H nearest neighbour, is missing in this experiment because surface heating was performed in bigger steps compared to Fig. 5.3.

Since I was only interested in understanding the origin of CH(ads) comes from, I did not try to reproduce the three CH(ads) peaks.

A similar experiment was carried out for the methyl on the terraces- Fig. 5.10, right panel. In this case, the surface was cleaned and then the step sites were passivated with deuterium atoms. This was achieved by leaking in 1 L of D₂ molecules into the UHV chamber while the surface was at T_s = 120 K. As the step sites were no longer available for the adsorption of the dissociated methane, only the terraces of the surface were covered with CH₃(ads) when the surface was exposed to a molecular beam of 3% CH₄ in He at T_s = 120 K with E_{kin} = 65 kJ/mol. This was confirmed with RAIRS measurements where a C-H stretch peak was recorded at 2890 cm⁻¹ (assigned to methyl on terraces) – Fig. 5.10(a), right panel. The surface was once again heated in steps to try to dehydrogenate the CH₃(ads) on the terraces of Pt(211). This time, there was no CH(ads) adsorbate observed, as shown in the right panel of Fig. 5.10 (b-d). Based on these results, it is clear that the CH(ads) observed on the Pt(211) surface originate from the decomposition of methyl on the step sites.

Further evidence showing that only the CH₃(ads) on the steps dehydrogenate to form the methylidyne species is presented in Fig. 5.11. In this case, the experiments were performed at a higher surface temperature, T_s = 220 K and it was found that by depositing methane molecules on the Pt(211) surface with 41 kJ/mol of incident energy, CH(ads) is the only product on the surface – Fig. 5.11(b), left panel. It is known from previous studies that a kinetic energy of 41 kJ/mol is only sufficient for methane dissociation on the steps of Pt(211) therefore, the CH(ads) peaks observed must be the result of continuous dehydrogenation of the hot methyl products on the steps⁴².

At first, the most red-shifted CH(ads) peak was observed at 2950 cm⁻¹, assigned to methylidyne with OH in its vicinity, Fig. 5.9(b), left panel. This observation is in contrast to Fig. 5.3 where the 2972 cm⁻¹ peak (for CH adsorbate with 2 neighbouring H atoms) appeared first following methyl decomposition. This difference can be explained as due to the low number of blocked sites on the surface at T_s = 220 K during initial deposition of methane molecules. Apart from that, the higher surface temperature also enhances hydrogen atoms diffusion along the steps of the surface. Thus, for a short time, almost all methylidyne adsorbates had zero adjacent hydrogen atom resulting in the appearance of a peak at 2950 cm⁻¹ first. With

increasing surface exposure to CH₄, the CH(ads) RAIRS peak slowly shifted in intensity to the most blue shifted CH(ads) RAIRS peak at 2972 cm⁻¹.

The right panel of Fig. 5.11 instead shows the RAIR spectra recorded during the deposition of methane beam at T_s = 220 K with E_{kin} = 64 kJ/mol. As the incident energy is enough to overcome the dissociation barriers on both the step and terrace sites of the Pt(211) surface, we observe CH₃(ads) on both these sites at 2904 cm⁻¹ (steps) and 2889 cm⁻¹ (terraces) at first, Fig. 5.11(c) -right panel ⁴². The methyl species on the steps was present briefly before it started broadening and disappearing whereas, the RAIRS peak for methyl on terraces grew as the exposure to methane molecules was increased. Even before the methyl peaks appeared, methylidyne absorption peaks were already visible. As in Fig. 5.11 -left panel, the most red-shifted peak at 2950 cm⁻¹ again appeared first before shifting in intensity to the more blue-shifted absorption peak. In this experiment, the source of CH(ads) can be clearly identified. The growing methyl coverage on the terraces and the short-lived methyl species on the steps show that the CH(ads) species comes only from the dehydrogenation of CH₃(ads) on the steps. This indicates that methylidyne forms one dimensional rows of adsorbates on the steps of Pt(211). The three discrete peaks of CH(ads) observed arise due to the confined motion of hydrogen atoms on the steps of the Pt(211) resulting in either 0, 1 or 2 hydrogen atoms near the CH(ads).

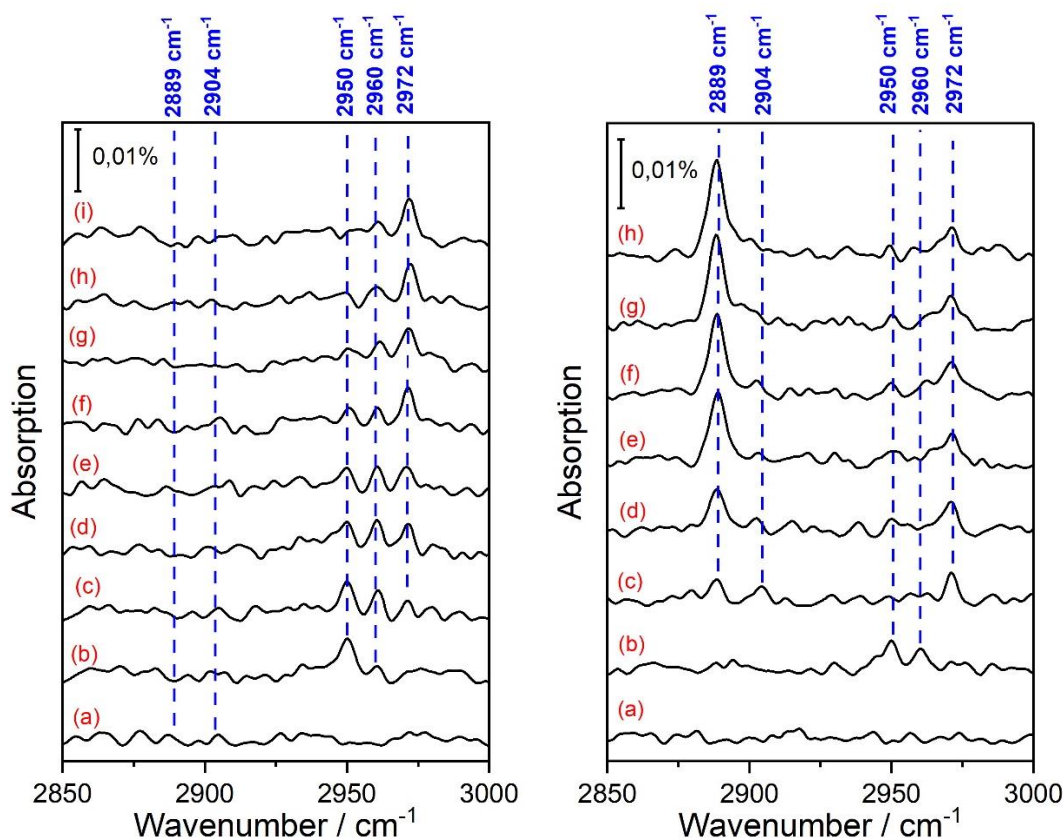


Fig. 5.11: RAIR spectra recorded during deposition of methane molecules on the Pt(211) with translational energy of 41 kJ/mol – left panel and 64 kJ/mol- right panel. Each spectrum was recorded following different methane molecules exposure – (a) 0 L, (b) 0.5 L, (c) 1.5 L, (d) 2.5 L, (e) 3.5 L, (f) 4.5 L, (g) 5.5 L, (h) 6.5 L and (i) 9.5 L.

5.4 Conclusion

In summary, methylidyne CH(ads) was formed on a Pt(211) surface through methyl dehydrogenation on the steps. Three RAIRS peaks at fixed frequency but with varying peak intensities were observed and their formation could be controlled by changing the surface coverage of co-adsorbed hydrogen atoms. The surprising observation of three discrete vibrational frequencies for the same adsorbate was tested based on two hypotheses - (i) the three RAIRS peaks of CH(ads) arise from different adsorption sites on the Pt(211) surface and (ii) three hydrogen environments namely, 0H, 1H and 2H around the methylidyne contribute to the three RAIRS peaks. The latter is proposed to explain the observation of the three distinct CH(ads) absorption peaks. When CH₄ was replaced with CD₄, three CD(ads) absorption peaks were observed and they behaved similar to the CH(ads) species. The methylidyne

adsorbates were also found to have a tendency to undergo H-D isotope exchange to form CD(ads) in the presence of D(ads).

Chapter 6: Conclusions and future work

6.1 Summary

6.1.1. Dissociation of water molecules on Cu(111)

The water dissociation mechanism on a partially oxygen covered Cu(111) surface was confirmed to be $\text{H}_2\text{O}(\text{g}) + \text{O}(\text{ads}) \rightarrow 2\text{OH}(\text{ads})$ with isotope labeling experiments. This is the first direct evidence for the formation of the two hydroxyls from water dissociation on the Cu(111) surface. At $T_s = 180$ K, a secondary process (disproportionation reaction), $2\text{OH}(\text{ads}) \rightarrow \text{H}_2\text{O}(\text{g}) + \text{O}(\text{ads})$ was observed to occur while water dissociated on the surface which replaced the initially dosed surface oxygen atoms with the oxygen atoms from the incoming water molecules. Apart from that, the formation of oxygen islands on the surface with two types of oxygen, the reactive oxygen atoms on the periphery of the islands and the non-reactive oxygen atoms in the middle of the islands were also observed in the experiments.

On a clean Cu(111) surface the state-resolved sticking coefficients for D_2O was measured for the anti-symmetric vibrational mode, ν_3 . The vibrational efficacy was determined as $\eta=0.7$. Based on Polanyi rules, this demonstrates the reaction has an 'early barrier' but the result is in contraction to the theoretical predictions. The vibrational efficacy measured showed a value lower than unity perhaps as a result of the laser-off experiments having prominent contribution from the vibrationally excited D_2O molecules, with increasing T_n .

6.1.2 Methylidyne co-adsorbed with hydrogen atoms on a Pt(211)

$\text{CH}(\text{ads})$ was produced on a stepped Pt(211) surface from thermal decomposition of $\text{CH}_3(\text{ads})$ on the step sites of the surface. Three discrete peaks assigned to methylidyne species were detected in the RAIR spectrum. They were observed to red-shift with decreasing surface hydrogen coverage and vice versa. With experiments and DFT calculations, the three $\text{CH}(\text{ads})$ peaks were demonstrated to arise from the different number of H atoms surrounding the CH adsorbate, 0H, 1H or 2H. The specific number of neighbouring hydrogen atoms present

near the CH(ads) was explained as a result of the confined one-dimensional motion of the hydrogen atoms on the steps of the Pt(211) surface.

6.2 Future work

6.2.1 Facile OD(ads) to OH(ads) exchange

During my study of dissociative adsorption of D₂O on the Cu(111) surface, I observed the OD(ads) species to be replaced by OH(ads). An experiment which demonstrate this observation is shown in Fig. 6.1. In this study, a MB of 2% D₂O in He with $E_{kin} = 1.1$ eV was collided with a Cu(111) surface resulting in the formation of OD(ads) measured with RAIRS at 2687 cm⁻¹- Fig. 6.1 (a). After exposing the surface to ~ 0.06 ML of D₂O in the MB, the beam was stopped and RAIR spectra were measured continuously. With time, the intensity of the OD peak was observed to reduce and a new peak was recorded at 3637 cm⁻¹, assigned to OH(ads).

The changing surface coverage of the OD(ads) and OH(ads) are presented in Fig.6.1 (b). Clearly, when the MB was no longer arriving on the surface, the OD(ads) coverage decreased and simultaneously more OH(ads) species appeared on the surface. An equilibrium between both the species was attained with time. This is an evidence for H-D exchange between surface bound OD(ads) and another molecule that acts as a source of H. Since the isotopic exchange was detected when the MB was stopped, the source of hydrogen must be coming from the molecules in the UHV background, either H₂O(g) or H₂(g).

Plotting the sum of the surface coverage of OH(ads) + OD(ads) shows a decrease in their total coverage once the MB was stopped indicating desorption of the isotopic hydroxyls through disproportionation reaction. In this condition, the rate of desorption through disproportionation is higher than the rate of dissociative adsorption of water molecules.

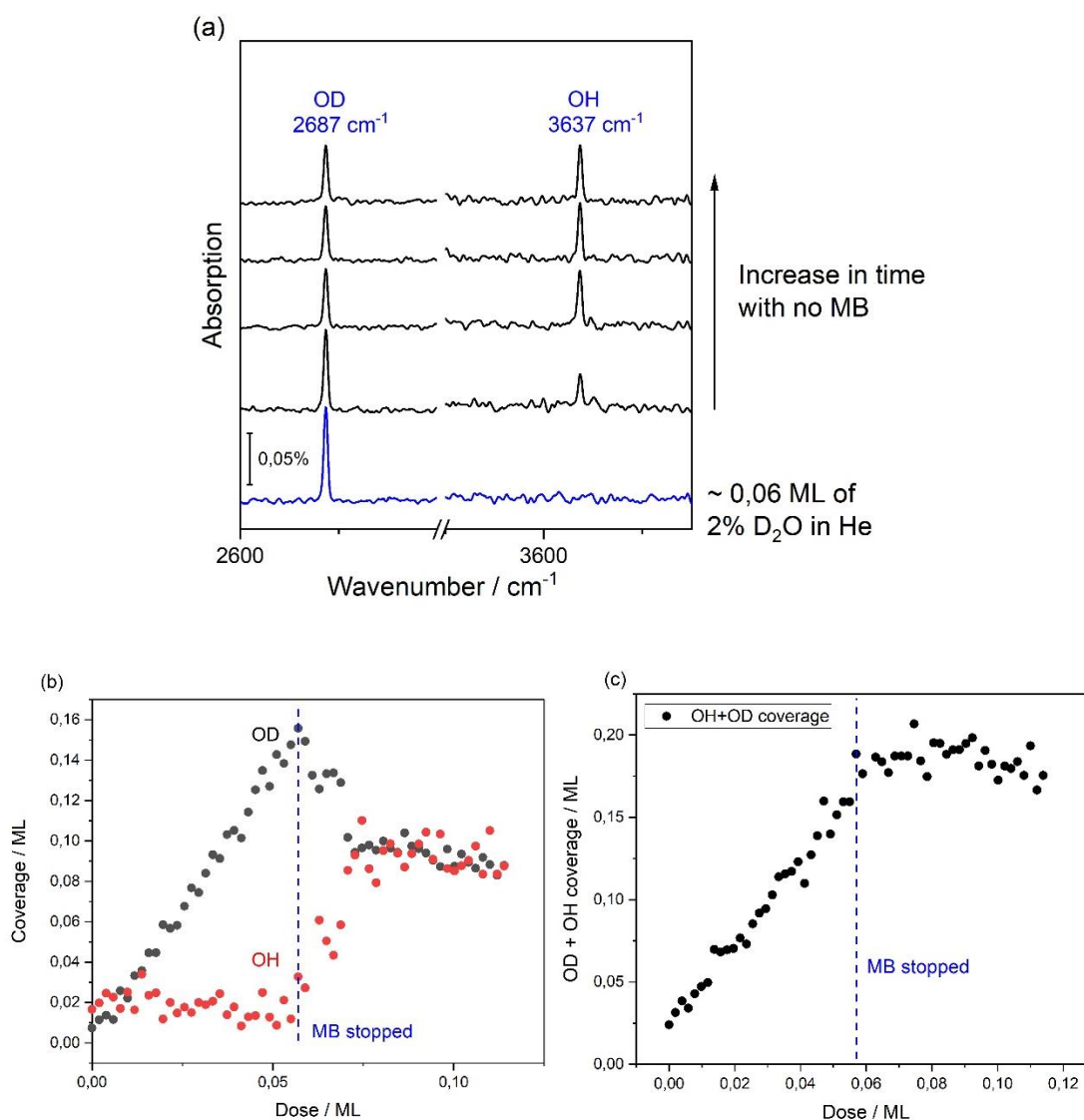


Fig. 6.1: (a) RAIR spectra showing the reduction of OD(ads) peak intensity and the appearance of a novel peak at 3637 cm^{-1} . (b) The coverage of OD and OH on the surface during surface exposure to a MB of 2% D_2O in He with $E_{kin} = 1.1 \text{ eV}$ and the evolution of these species after the MB was stopped. (c) Total coverage of the adsorbates (OH + OD) plotted from (b).

The source of H for the H/D exchange of the hydroxyl adsorbates in Fig. 6.1 was tested using deuterated water molecules. Initially the surface was pre-covered with 0.07 ML of oxygen atoms and allowed to react with $\text{H}_2\text{O}(\text{g})$ from the UHV chamber to produce OH(ads) on the surface. $\text{D}_2\text{O}(\text{g})$ was then leaked into the UHV chamber and this resulted in the OH(ads) conversion into OD(ads) as shown in Figure 6.2 below. It is clear that in this case, the $\text{D}_2\text{O}(\text{g})$ is the source of D however, it is not clear if the exchange occurs after the D_2O adsorbs on the surface (Langmuir-Hinshelwood reaction) or with an incoming gaseous D_2O (Eley-Riedel reaction) and the surface OH(ads). It will be interesting to continue this study and identify the

mechanism of H/D exchange between the hydroxyl on the surface and incident water molecules.

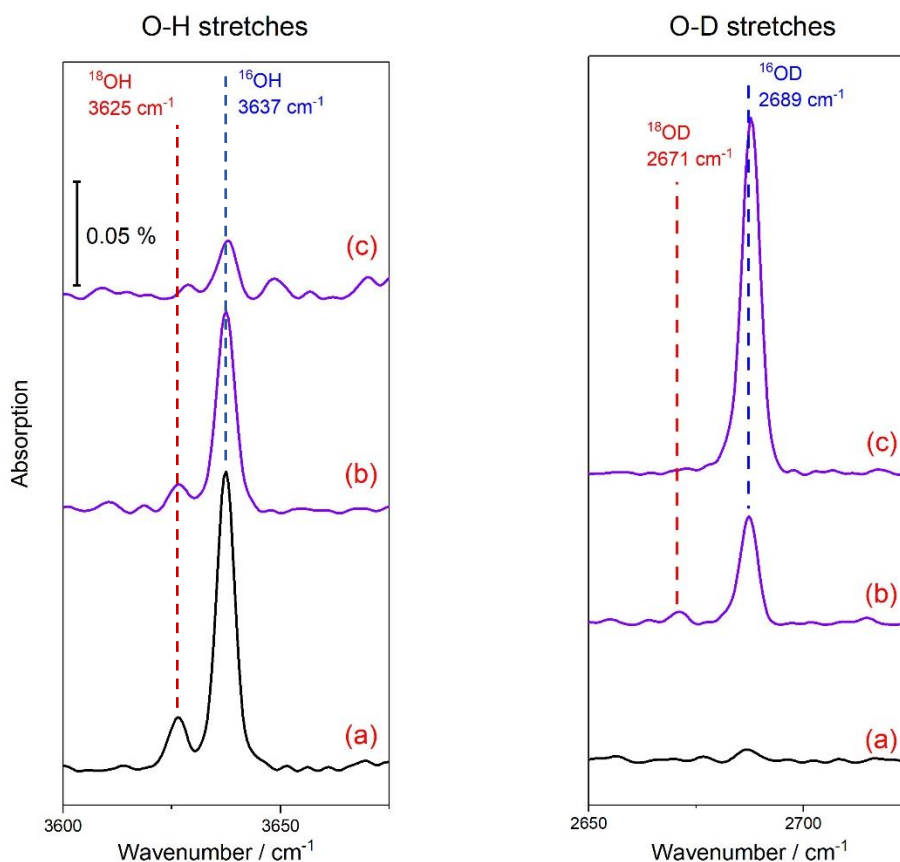


Fig. 6.2: On the left, the IR spectra for O-H stretches are presented and on the right, RARS spectra for O-D stretches are shown. Both set of IR spectra demonstrate the uptake for surface hydroxyls when a surface with 0.07 ML of $^{18}\text{O}(\text{ads})$ was exposed to $\text{H}_2^{16}\text{O}(\text{g})$ from the UHV background (black spectra) followed by surface exposure to $\text{D}_2^{16}\text{O}(\text{g})$ (purple spectra). The amount of water exposure for the different spectra are as following, (a) 0.09 L, (b) 0.11 L and (c) 0.46 L.

6.2.2 Site-selective water dissociation study on stepped surfaces using RARS

RARS is a powerful surface science tool to identify reactions occurring on different adsorption sites on metal surfaces. The first site-selective dissociation for methane on the steps and terraces of a Pt(211) was performed in our lab ²⁴. The nascent products on the different adsorption sites were distinguished from their absorption frequencies measured using RARS. Being able to measure the products on the steps and terraces of Pt(211) enabled one to control reactions on the different sites, separately.

The dissociative adsorption of water molecules have been investigated on various stepped surfaces such as Cu(110) and Fe(100) but no surface site specific studies have been reported ^{6,8}. It will therefore be very interesting to perform investigations of water dissociation on stepped Cu surfaces while monitoring the site-selective reaction with RAIRS.

6.2.3 Vibrational mode specific water dissociation on Cu(111)

Being able to perform quantum state resolved experiments involving addition of vibrational energy to the incident molecules and then measuring the efficiency of a reaction is a huge progress in the heterogeneous catalysis studies. Based on the model proposed by Polanyi, the water dissociation on metal surfaces has a “late” transition state ¹⁶. Therefore, it is predicted that the reaction will be significantly enhanced with vibrational energy compared to translational energy.

A theoretical study was performed by Jiang *et al.* to identify if vibrational energy promotes water dissociation on a Cu(111) surface better than translational energy ³⁵. The following Fig. 6.3 is one of their results from the DFT calculations. It shows sticking probabilities predicted for different vibrational modes of the incident water molecules, (ν_1 -symmetric stretch, ν_2 -bending mode, ν_3 -antisymmetric stretch) and ground state molecules ³⁵. In general, vibrationally promoted molecules are observed to have higher reactivity than translational energy. The symmetric stretching mode was calculated to have the most prominent effect compared to the asymmetric and bending modes. This enhancement was considered a result of the symmetrically stretched vibration to be in the reaction coordinates. The calculated results can be tested in our laboratory by preparing the water molecules in specific vibrational states before colliding with a Cu(111) surface. Simultaneous measurement of the dissociation product with RAIRS will give the sticking probabilities for the different vibrational modes which can then be compared with the theoretical values.

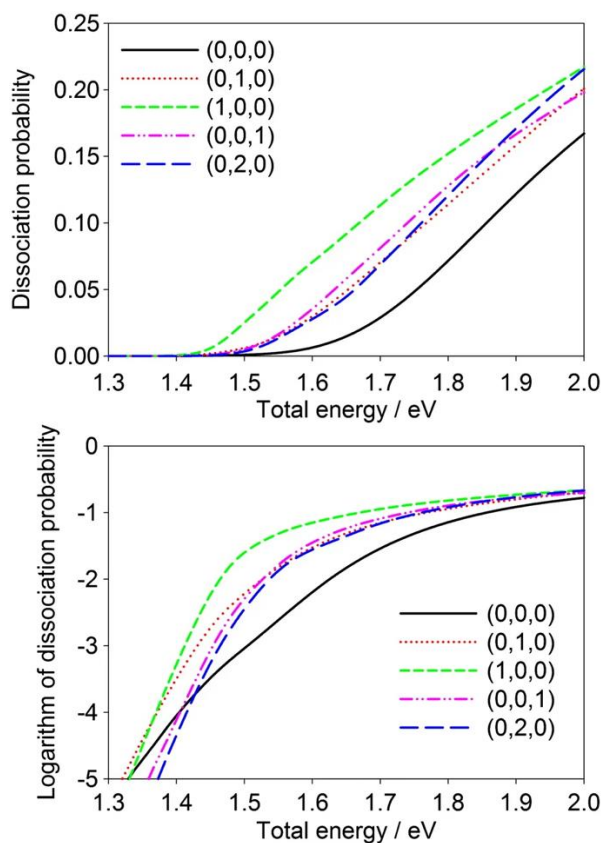


Fig.6.3: Top- Reactivity of vibrationally excited water molecules (v_1, v_2, v_3) on a Cu(111) where the black curve represents the molecules in the ground state. Bottom- Same as the top graph but dissociation probability is in the logarithmic scale. Reproduced from ³⁵.

6.2.4 Bond selectivity study of HOD

Apart from the vibrational mode selectivity, bond selective dissociative chemisorption of water molecules on a Cu(111) surface could be studied in our lab. A DFT calculation study performed by Jiang *et al.*, investigated the implications of exciting a specific bond in the HOD molecules on its dissociation on a Cu(111) and their results are shown in Fig. 6.4 where (abc) refer to a- ν_{OD} , b- bending, c- ν_{OH} ³⁶. Placing vibrational energy in the O-D stretch caused this bond to selectively break as shown in Fig. 6.4- top. Whereas, when the O-H stretch was excited, the dissociation favoured the O-H bond, Fig. 6.4-bottom. The higher reactivity exhibited by vibrationally excited molecules was attributed to the “late barrier” on the potential energy surface for water dissociation whereas the O-H or O-D bond-selective dissociation was explained as a result of the slow redistribution of vibrational energy in the HOD molecules.

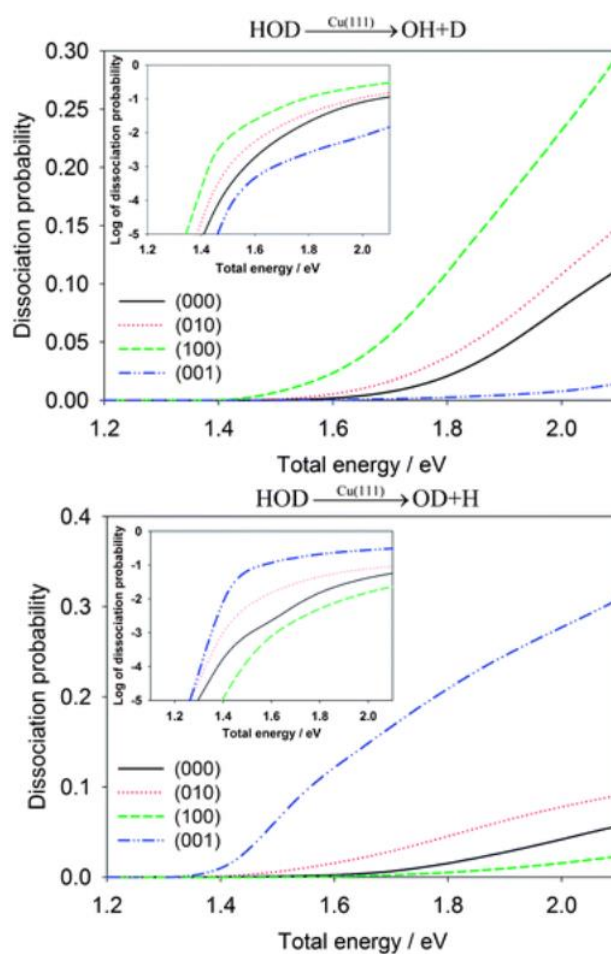


Fig. 6.4: The probability of dissociative chemisorption of HOD molecules in various low-lying vibrational states. The reaction can occur through two channels, top- $\text{HOD} \rightarrow \text{OH} + \text{D}$ and bottom- $\text{HOD} \rightarrow \text{OD} + \text{H}$. Reproduced from ³⁶.

6.2.5 Quantum state resolved study of CO_2 dissociation on a Cu(111)

Quan and co-workers conducted a study of CO_2 reaction with adsorbed H atoms on a Cu(111) surface using RAIRS, TPD and supersonic expanded molecular beam ⁸⁶. The reaction was proposed to proceed through Eley-Riedel mechanism where the impinging CO_2 molecules react with the H adsorbates on the surface resulting in the formation of $\text{HCOO}(\text{ads})$. The reaction was reported to be improved when the CO_2 molecules were vibrationally excited. The O-C-O bending mode was proposed to be the main contributor to the enhanced CO_2 reaction with H on the Cu(111) surface as this vibrational mode resembles the transition state ⁸⁶. However, there is a limitation to this study. The authors could not isolate the molecules in a specific vibrational state because they populated the vibrational states of CO_2 by thermal

heating of the nozzle. In our lab, instead, we are able to prepare the incident CO₂ molecules in a specific ro-vibrational state using laser. Therefore, we could test the study by Quan *et al.* using IR laser coupled with RAIRS.

References

- (1) Jennings, J. R. *Catalytic Ammonia Synthesis: Fundamentals and Practice*; Springer Science & Business Media, 1991.
- (2) Roduner, E. Understanding Catalysis. *Chem Soc Rev* **2014**, *43* (24), 8226–8239. <https://doi.org/10.1039/C4CS00210E>.
- (3) Che, M. Nobel Prize in Chemistry 1912 to Sabatier: Organic Chemistry or Catalysis? *Catal. Today* **2013**, *218–219*, 162–171. <https://doi.org/10.1016/j.cattod.2013.07.006>.
- (4) Chorkendorff, I.; Niemantsverdriet, J. W. *Concepts of Modern Catalysis and Kinetics*, 1st ed.; John Wiley & Sons, Ltd, 2003. <https://doi.org/10.1002/3527602658>.
- (5) J, B. S. R.; Loganathan, M.; Shantha, M. S. A Review of the Water Gas Shift Reaction Kinetics. *Int. J. Chem. React. Eng.* **2010**, *8* (1). <https://doi.org/10.2202/1542-6580.2238>.
- (6) Henderson, M. A. The Interaction of Water with Solid Surfaces: Fundamental Aspects Revisited. *Surf. Sci. Rep.* **2002**, *46* (1), 1–308. [https://doi.org/10.1016/S0167-5729\(01\)00020-6](https://doi.org/10.1016/S0167-5729(01)00020-6).
- (7) Hinch, B. J.; Dubois, L. H. Stable and Metastable Phases of Water Adsorbed on Cu(111). *J. Chem. Phys.* **1992**, *96* (4), 3262–3268. <https://doi.org/10.1063/1.461971>.
- (8) Thiel, P. A.; Madey, T. E. The Interaction of Water with Solid Surfaces: Fundamental Aspects. *Surf. Sci. Rep.* **1987**, *7* (6), 211–385. [https://doi.org/10.1016/0167-5729\(87\)90001-X](https://doi.org/10.1016/0167-5729(87)90001-X).
- (9) Kimmel, G. A.; Petrik, N. G.; Dohnálek, Z.; Kay, B. D. Layer-by-Layer Growth of Thin Amorphous Solid Water Films on Pt(111) and Pd(111). *J. Chem. Phys.* **2006**, *125* (4), 044713. <https://doi.org/10.1063/1.2218844>.
- (10) Beniya, A.; Sakaguchi, Y.; Narushima, T.; Mukai, K.; Yamashita, Y.; Yoshimoto, S.; Yoshinobu, J. The Growth Process of First Water Layer and Crystalline Ice on the Rh(111) Surface. *J. Chem. Phys.* **2009**, *130* (3), 034706. <https://doi.org/10.1063/1.3060952>.
- (11) Gallagher, M. E.; Haq, S.; Omer, A.; Hodgson, A. Water Monolayer and Multilayer Adsorption on Ni(111). *Surf. Sci.* **2007**, *601* (1), 268–273. <https://doi.org/10.1016/j.susc.2006.09.034>.
- (12) Glebov, A.; Graham, A. P.; Menzel, A.; Toennies, J. P. Orientational Ordering of Two-Dimensional Ice on Pt(111). *J. Chem. Phys.* **1997**, *106* (22), 9382–9385. <https://doi.org/10.1063/1.474008>.
- (13) Massey, A.; McBride, F.; Darling, G. R.; Nakamura, M.; Hodgson, A. The Role of Lattice Parameter in Water Adsorption and Wetting of a Solid Surface. *Phys Chem Chem Phys* **2014**, *16* (43), 24018–24025. <https://doi.org/10.1039/C4CP03164D>.
- (14) Hodgson, A.; Haq, S. Water Adsorption and the Wetting of Metal Surfaces. *Surf. Sci. Rep.* **2009**, *64* (9), 381–451. <https://doi.org/10.1016/j.surfrep.2009.07.001>.

-
- (15) Yamamoto, S.; Andersson, K.; Bluhm, H.; Ketteler, G.; Starr, D. E.; Schiros, T.; Ogasawara, H.; Pettersson, L. G. M.; Salmeron, M.; Nilsson, A. Hydroxyl-Induced Wetting of Metals by Water at Near-Ambient Conditions. *J. Phys. Chem. C* **2007**, *111* (22), 7848–7850. <https://doi.org/10.1021/jp0731654>.
- (16) Polanyi, J. C. Concepts in Reaction Dynamics. *Acc. Chem. Res.* **1972**, *5* (5), 161–168. <https://doi.org/10.1021/ar50053a001>.
- (17) Chadwick, H.; Beck, R. D. Quantum State Resolved Gas–Surface Reaction Dynamics Experiments: A Tutorial Review. *Chem. Soc. Rev.* **2016**, *45* (13), 3576–3594. <https://doi.org/10.1039/C5CS00476D>.
- (18) Juurlink, L. B. F.; McCabe, P. R.; Smith, R. R.; DiCologero, C. L.; Utz, A. L. Eigenstate-Resolved Studies of Gas-Surface Reactivity: CH₄ (v₃) Dissociation on Ni(100). *Phys. Rev. Lett.* **1999**, *83* (4), 868–871. <https://doi.org/10.1103/PhysRevLett.83.868>.
- (19) Maroni, P.; Papageorgopoulos, D. C.; Sacchi, M.; Dang, T. T.; Beck, R. D.; Rizzo, T. R. State-Resolved Gas-Surface Reactivity of Methane in the Symmetric C-H Stretch Vibration on Ni(100). *Phys. Rev. Lett.* **2005**, *94* (24), 246104. <https://doi.org/10.1103/PhysRevLett.94.246104>.
- (20) Beck, R. D.; Maroni, P.; Papageorgopoulos, D. C.; Dang, T. T.; Schmid, M. P.; Rizzo, T. R. Vibrational Mode-Specific Reaction of Methane on a Nickel Surface. *Science* **2003**, *302* (5642), 98–100. <https://doi.org/10.1126/science.1088996>.
- (21) Hundt, P. M.; Jiang, B.; van Reijzen, M. E.; Guo, H.; Beck, R. D. Vibrationally Promoted Dissociation of Water on Ni(111). *Science* **2014**, *344* (6183), 504–507. <https://doi.org/10.1126/science.1251277>.
- (22) Sinha, A.; Hsiao, M. C.; Crim, F. F. Bond-selected Bimolecular Chemistry: H+HOD(4vOH)→OD+H₂. *J. Chem. Phys.* **1990**, *92* (10), 6333–6335. <https://doi.org/10.1063/1.458312>.
- (23) Killelea, D. R.; Campbell, V. L.; Shuman, N. S.; Utz, A. L. Bond-Selective Control of a Heterogeneously Catalyzed Reaction. *Science* **2008**, *319* (5864), 790–793. <https://doi.org/10.1126/science.1152819>.
- (24) Gutiérrez-González, A.; Torio, M. E.; Busnengo, H. F.; Beck, R. D. Site Selective Detection of Methane Dissociation on Stepped Pt Surfaces. *Top. Catal.* **2019**, *62* (12), 859–873. <https://doi.org/10.1007/s11244-019-01170-5>.
- (25) Gutiérrez-González, A.; Crim, F. F.; Beck, R. D. Bond Selective Dissociation of Methane (CH₃D) on the Steps and Terraces of Pt(211). *J. Chem. Phys.* **2018**, *149* (7), 074701. <https://doi.org/10.1063/1.5041349>.

-
- (26) Xu, H.; Fu, C.; Zhang, Z.; Chai, P.; Wu, L.; Wang, H.; Huang, W. Role of Coadsorbates in Shaping the Reaction Pathways of Alkyl Fragments on Co Surfaces. *J. Phys. Chem. C* **2020**, *124* (45), 24786–24794. <https://doi.org/10.1021/acs.jpcc.0c07189>.
- (27) Díaz, C.; Pijper, E.; Olsen, R. A.; Busnengo, H. F.; Auerbach, D. J.; Kroes, G. J. Chemically Accurate Simulation of a Prototypical Surface Reaction: H₂ Dissociation on Cu(111). *Science* **2009**, *326* (5954), 832–834. <https://doi.org/10.1126/science.1178722>.
- (28) Kroes, G.-J.; Gross, A.; Baerends, E.-J.; Scheffler, M.; McCormack, D. A. Quantum Theory of Dissociative Chemisorption on Metal Surfaces. *Acc. Chem. Res.* **2002**, *35* (3), 193–200. <https://doi.org/10.1021/ar010104u>.
- (29) Perdew, J. P.; Ruzsinszky, A.; Csonka, G. I.; Vydrov, O. A.; Scuseria, G. E.; Constantin, L. A.; Zhou, X.; Burke, K. Restoring the Density-Gradient Expansion for Exchange in Solids and Surfaces. *Phys. Rev. Lett.* **2008**, *100* (13), 136406. <https://doi.org/10.1103/PhysRevLett.100.136406>.
- (30) Filippi, C.; Healy, S. B.; Kratzer, P.; Pehlke, E.; Scheffler, M. Quantum Monte Carlo Calculations of H₂ Dissociation on Si(001). *Phys. Rev. Lett.* **2002**, *89* (16), 166102. <https://doi.org/10.1103/PhysRevLett.89.166102>.
- (31) Mondal, A.; Seenivasan, H.; Tiwari, A. K. Water Dissociation on Cu (111): Effects of Molecular Orientation, Rotation, and Vibration on Reactivity. *J. Chem. Phys.* **2012**, *137* (9), 094708. <https://doi.org/10.1063/1.4749246>.
- (32) Farjamnia, A.; Jackson, B. The Dissociative Chemisorption of Water on Ni(111): Mode- and Bond-Selective Chemistry on Metal Surfaces. *J. Chem. Phys.* **2015**, *142* (23), 234705. <https://doi.org/10.1063/1.4922625>.
- (33) Tiwari, A. K.; Nave, S.; Jackson, B. Methane Dissociation on Ni(111): A New Understanding of the Lattice Effect. *Phys. Rev. Lett.* **2009**, *103* (25), 253201. <https://doi.org/10.1103/PhysRevLett.103.253201>.
- (34) Tiwari, A. K.; Nave, S.; Jackson, B. The Temperature Dependence of Methane Dissociation on Ni(111) and Pt(111): Mixed Quantum-Classical Studies of the Lattice Response. *J. Chem. Phys.* **2010**, *132* (13), 134702. <https://doi.org/10.1063/1.3357415>.
- (35) Jiang, B.; Ren, X.; Xie, D.; Guo, H. Enhancing Dissociative Chemisorption of H₂O on Cu(111) via Vibrational Excitation. *Proc. Natl. Acad. Sci.* **2012**, *109* (26), 10224–10227. <https://doi.org/10.1073/pnas.1203895109>.
- (36) Jiang, B.; Xie, D.; Guo, H. Vibrationally Mediated Bond Selective Dissociative Chemisorption of HOD on Cu(111). *Chem. Sci.* **2013**, *4* (1), 503–508. <https://doi.org/10.1039/C2SC21393A>.
- (37) Jiang, B.; Guo, H. Prediction of Mode Specificity, Bond Selectivity, Normal Scaling, and Surface Lattice Effects in Water Dissociative Chemisorption on Several Metal Surfaces Using the Sudden

- Vector Projection Model. *J. Phys. Chem. C* **2014**, *118* (46), 26851–26858. <https://doi.org/10.1021/jp5090839>.
- (38) Guo, H.; Jiang, B. The Sudden Vector Projection Model for Reactivity: Mode Specificity and Bond Selectivity Made Simple. *Acc. Chem. Res.* **2014**, *47* (12), 3679–3685. <https://doi.org/10.1021/ar500350f>.
- (39) Zhang, Z.; Liu, T.; Fu, B.; Yang, X.; Zhang, D. H. First-Principles Quantum Dynamical Theory for the Dissociative Chemisorption of H₂O on Rigid Cu(111). *Nat. Commun.* **2016**, *7* (1), 11953. <https://doi.org/10.1038/ncomms11953>.
- (40) *Vibrationally Bond-Selective Chemisorption of Methane Isotopologues on Pt(111) Studied by Reflection Absorption Infrared Spectroscopy*; Chen, L., Ed.; EPFL: Lausanne, 2012. <https://doi.org/10.5075/epfl-thesis-5452>.
- (41) Chen, L.; Ueta, H.; Bisson, R.; Beck, R. D. Quantum State-Resolved Gas/Surface Reaction Dynamics Probed by Reflection Absorption Infrared Spectroscopy. *Rev. Sci. Instrum.* **2013**, *84* (5), 053902. <https://doi.org/10.1063/1.4803933>.
- (42) Gutiérrez González, A. Bond-Selective and Surface-Site-Specific Dissociation of Methane on Platinum, EPFL, Lausanne, 2019. <https://doi.org/10.5075/epfl-thesis-9530>.
- (43) Bhatt, S. B.; Kumar, A.; Subramanian, K. P.; Atrey, P. K.; Team, A. Gas Puffing by Molecular Beam Injection in Aditya Tokamak. *Fusion Eng. Des.* **2005**, *75–79*, 655–661. <https://doi.org/10.1016/j.fusengdes.2005.06.176>.
- (44) Morse, M. D. Chapter 2 - Supersonic Beam Sources. In *Experimental Methods in the Physical Sciences*; Dunning, F. B., Hulet, R. G., Eds.; Atomic, Molecular, and Optical Physics: Atoms and Molecules; Academic Press, 1996; Vol. 29, pp 21–47. [https://doi.org/10.1016/S0076-695X\(08\)60784-X](https://doi.org/10.1016/S0076-695X(08)60784-X).
- (45) Auerbach, D. J.; Rettner, C. T. High-temperature Supersonic Molecular-beam Source. *Rev. Sci. Instrum.* **1992**, *63* (8), 3939–3943. <https://doi.org/10.1063/1.1143242>.
- (46) Matsunaga, N.; Nagashima, A. Saturation Vapor Pressure and Critical Constants of H₂O, D₂O, T₂O, and Their Isotopic Mixtures. *Int. J. Thermophys.* **1987**, *8* (6), 681–694. <https://doi.org/10.1007/BF00500788>.
- (47) Mudiyansele, K.; Xu, F.; Hoffmann, F. M.; Hrbek, J.; Waluyo, I.; Boscoboinik, J. A.; Stacchiola, D. J. Adsorbate-Driven Morphological Changes on Cu(111) Nano-Pits. *Phys. Chem. Chem. Phys.* **2015**, *17* (5), 3032–3038. <https://doi.org/10.1039/C4CP05088F>.
- (48) Niehus, H. Surface Reconstruction of Cu (111) upon Oxygen Adsorption. *Surf. Sci.* **1983**, *130* (1), 41–49. [https://doi.org/10.1016/0039-6028\(83\)90258-3](https://doi.org/10.1016/0039-6028(83)90258-3).

-
- (49) Chadwick, H.; Guo, H.; Gutiérrez-González, A.; Menzel, J. P.; Jackson, B.; Beck, R. D. Methane Dissociation on the Steps and Terraces of Pt(211) Resolved by Quantum State and Impact Site. *J. Chem. Phys.* **2018**, *148* (1), 014701. <https://doi.org/10.1063/1.5008567>.
- (50) Jiang, Z.; Fang, T. Dissociation Mechanism of H₂O on Clean and Oxygen-Covered Cu (111) Surfaces: A Theoretical Study. *Vacuum* **2016**, *128*, 252–258. <https://doi.org/10.1016/j.vacuum.2016.03.030>.
- (51) McDonnell, L.; Powell, B. D.; Woodruff, D. P. Temperature Dependent Peaks in Secondary Electron Emission Spectra. *Surf. Sci.* **1973**, *40* (3), 669–682. [https://doi.org/10.1016/0039-6028\(73\)90151-9](https://doi.org/10.1016/0039-6028(73)90151-9).
- (52) Heras, J. M.; Viscido, L. Oxygen Fixing on Cu Due to Electron-Beam Damage during Auger Spectroscopy. *J Vac Sci Technol A* **1997**, *15* (4), 8.
- (53) Wiedmann, L.; Ganschow, O.; Benninghoven, A. Contamination of Clean Metal Surfaces Associated with Electron Bombardment in Conventional AES Analysis. *J. Electron Spectrosc. Relat. Phenom.* **1978**, *13* (3), 243–246. [https://doi.org/10.1016/0368-2048\(78\)85030-0](https://doi.org/10.1016/0368-2048(78)85030-0).
- (54) Jensen, F.; Besenbacher, F.; Stensgaard, I. Two New Oxygen Induced Reconstructions on Cu(111). *Surf. Sci.* **1992**, *269–270*, 400–404. [https://doi.org/10.1016/0039-6028\(92\)91282-G](https://doi.org/10.1016/0039-6028(92)91282-G).
- (55) Therrien, A. J.; Groden, K.; Hensley, A. J. R.; Schilling, A. C.; Hannagan, R. T.; Marcinkowski, M. D.; Pronschinske, A.; Lucci, F. R.; Sykes, E. C. H.; McEwen, J.-S. Water Activation by Single Pt Atoms Supported on a Cu₂O Thin Film. *J. Catal.* **2018**, *364*, 166–173. <https://doi.org/10.1016/j.jcat.2018.04.024>.
- (56) Hundt, P. M. Quantum-State Resolved Gas/Surface Reaction Dynamics of Water and Methane, EPFL, Lausanne, 2014. <https://doi.org/10.5075/epfl-thesis-6061>.
- (57) Ariga, K.; Aono, M. *Advanced Supramolecular Nanoarchitectonics*; William Andrew, 2019.
- (58) *Steric Effects in the Chemisorption of Vibrationally Excited Methane on Nickel*; Yoder, B., Ed.; EPFL: Lausanne, 2010. <https://doi.org/10.5075/epfl-thesis-4784>.
- (59) Chadwick, H.; Hundt, P. M.; van Reijzen, M. E.; Yoder, B. L.; Beck, R. D. Quantum State Specific Reactant Preparation in a Molecular Beam by Rapid Adiabatic Passage. *J. Chem. Phys.* **2014**, *140* (3), 034321. <https://doi.org/10.1063/1.4861054>.
- (60) Bronnikov, D. K.; Kalinin, D. V.; Rusanov, V. D.; Filimonov, YU. G.; Selivanov, YU. G.; Hilico, J. C. Spectroscopy and Non-Equilibrium Distribution of Vibrationally Excited Methane in a Supersonic Jet. *J. Quant. Spectrosc. Radiat. Transf.* **1998**, *60* (6), 1053–1068. [https://doi.org/10.1016/S0022-4073\(97\)00210-0](https://doi.org/10.1016/S0022-4073(97)00210-0).

-
- (61) Wang, G.-C.; Tao, S.-X.; Bu, X.-H. A Systematic Theoretical Study of Water Dissociation on Clean and Oxygen-Preadsorbed Transition Metals. *J. Catal.* **2006**, *244* (1), 10–16. <https://doi.org/10.1016/j.jcat.2006.07.034>.
- (62) Ratnasamy, C.; Wagner, J. P. Water Gas Shift Catalysis. *Catal. Rev.* **2009**, *51* (3), 325–440. <https://doi.org/10.1080/01614940903048661>.
- (63) Matsumoto, T.; Bennett, R. A.; Stone, P.; Yamada, T.; Domen, K.; Bowker, M. Scanning Tunneling Microscopy Studies of Oxygen Adsorption on Cu(111). *Surf. Sci.* **2001**, *471* (1), 225–245. [https://doi.org/10.1016/S0039-6028\(00\)00918-3](https://doi.org/10.1016/S0039-6028(00)00918-3).
- (64) Pérez León, C.; Sürgers, C.; v. Löhneysen, H. Formation of Copper Oxide Surface Structures via Pulse Injection of Air onto Cu(111) Surfaces. *Phys. Rev. B* **2012**, *85* (3), 035434. <https://doi.org/10.1103/PhysRevB.85.035434>.
- (65) Mudiyansele, K.; Senanayake, S. D.; Ramirez, P. J.; Kundu, S.; Baber, A.; Yang, F.; Agnoli, S.; Axnanda, S.; Liu, Z.; Hrbek, J.; Evans, J.; Rodriguez, J. A.; Stacchiola, D. Intermediates Arising from the Water–Gas Shift Reaction over Cu Surfaces: From UHV to Near Atmospheric Pressures. *Top. Catal.* **2015**, *58* (4–6), 271–280. <https://doi.org/10.1007/s11244-015-0368-y>.
- (66) Jenniskens, P.; Banham, S. F.; Blake, D. F.; McCoustra, M. R. S. Liquid Water in the Domain of Cubic Crystalline Ice Ic. *J. Chem. Phys.* **1997**, *107* (4), 1232–1241. <https://doi.org/10.1063/1.474468>.
- (67) Asay, D. B.; Kim, S. H. Evolution of the Adsorbed Water Layer Structure on Silicon Oxide at Room Temperature. *J. Phys. Chem. B* **2005**, *109* (35), 16760–16763. <https://doi.org/10.1021/jp053042o>.
- (68) Wang, W.; Wang, G. Theoretical Study of Direct versus Oxygen-Assisted Water Dissociation on the Cu(110) Surface. *Appl. Surf. Sci.* **2015**, *351*, 846–852. <https://doi.org/10.1016/j.apsusc.2015.06.019>.
- (69) Liu, Q.; Li, J.; Tong, X.; Zhou, G. Enhancing Dissociative Adsorption of Water on Cu(111) via Chemisorbed Oxygen. *J. Phys. Chem. C* **2017**, *121* (22), 12117–12126. <https://doi.org/10.1021/acs.jpcc.6b12897>.
- (70) Kumagai, T.; Kaizu, M.; Okuyama, H.; Hatta, S.; Aruga, T.; Hamada, I.; Morikawa, Y. Tunneling Dynamics of a Hydroxyl Group Adsorbed on Cu(110). *Phys. Rev. B* **2009**, *79* (3), 035423. <https://doi.org/10.1103/PhysRevB.79.035423>.
- (71) Woodruff, D. P.; Hayden, B. E.; Prince, K.; Bradshaw, A. M. Dipole Coupling and Chemical Shifts in IRAS of CO Adsorbed on Cu(110). *Surf. Sci.* **1982**, *123* (2), 397–412. [https://doi.org/10.1016/0039-6028\(82\)90336-3](https://doi.org/10.1016/0039-6028(82)90336-3).

-
- (72) Mudiyansele, K.; Yang, Y.; Hoffmann, F. M.; Furlong, O. J.; Hrbek, J.; White, M. G.; Liu, P.; Stacchiola, D. J. Adsorption of Hydrogen on the Surface and Sub-Surface of Cu(111). *J. Chem. Phys.* **2013**, *139* (4), 044712. <https://doi.org/10.1063/1.4816515>.
- (73) Grellner, F.; Klingenberg, B.; Borgmann, D.; Wedler, G. Electron Spectroscopic Study of the Interaction of Oxygen with Co(1120) and of Coadsorption with Water. *J. Electron Spectrosc. Relat. Phenom.* **1995**, *71* (2), 107–115. [https://doi.org/10.1016/0368-2048\(94\)02261-5](https://doi.org/10.1016/0368-2048(94)02261-5).
- (74) Bange, K.; Grider, D. E.; Madey, T. E.; Sass, J. K. The Surface Chemistry of H₂O on Clean and Oxygen-Covered Cu(110). *Surf. Sci.* **1984**, *137* (1), 38–64. [https://doi.org/10.1016/0039-6028\(84\)90675-7](https://doi.org/10.1016/0039-6028(84)90675-7).
- (75) Juurlink, L. B. F.; Killelea, D. R.; Utz, A. L. State-Resolved Probes of Methane Dissociation Dynamics. *Prog. Surf. Sci.* **2009**, *84* (3), 69–134. <https://doi.org/10.1016/j.progsurf.2009.01.001>.
- (76) Maity, A.; Maithani, S.; Pal, A.; Pradhan, M. High-resolution Spectroscopic Probing of Ortho and Para Nuclear-Spin Isomers of Heavy Water in the Gas Phase. *Chem. Phys.* **2021**, *541*, 111041. <https://doi.org/10.1016/j.chemphys.2020.111041>.
- (77) Shirin, S. V.; Zobov, N. F.; Polyansky, O. L. Theoretical Line List of D₂¹⁶O up to 16,000cm⁻¹ with an Accuracy Close to Experimental. *J. Quant. Spectrosc. Radiat. Transf.* **2008**, *109* (4), 549–558. <https://doi.org/10.1016/j.jqsrt.2007.07.010>.
- (78) Chorkendorff, I.; Niemantsverdriet, J. W. Chapter 9-Oil Refining and Petrochemistry. In *Concepts of Modern Catalysis and Kinetics*; John Wiley & Sons, Ltd, 2003; pp 349–376. <https://doi.org/10.1002/3527602658.ch9>.
- (79) Yang, Q. Y.; Maynard, K. J.; Johnson, A. D.; Ceyer, S. T. The Structure and Chemistry of CH₃ and CH Radicals Adsorbed on Ni(111). *J. Chem. Phys.* **1995**, *102* (19), 7734–7749. <https://doi.org/10.1063/1.469026>.
- (80) Deng, R.; Herceg, E.; Trenary, M. Characterization of Methylidyne on Pt(111) with Infrared Spectroscopy. *Surf. Sci.* **2004**, *573*, 310–319. <https://doi.org/10.1016/j.susc.2004.10.002>.
- (81) Vejayan, H.; Gutiérrez González, A.; Torio, M.; Busnengo, H. F.; Beck, R. D. Methylidyne Adsorption on Pt(111) Probed by Reflection Absorption Infrared Spectroscopy (RAIRS). *J. Phys. Chem. C* **2022**, *126* (49), 20886–20891. <https://doi.org/10.1021/acs.jpcc.2c07235>
- (82) Zhang, D.; Jansen, C.; Berg, O. T.; Bakker, J. M.; Meyer, J.; Kleyn, A. W.; Juurlink, L. B. F. RAIRS Characterization of CO and O Coadsorption on Cu(111). *J. Phys. Chem. C* **2022**, *126* (31), 13114–13121. <https://doi.org/10.1021/acs.jpcc.2c02541>.
- (83) Laury, M. L.; Carlson, M. J.; Wilson, A. K. Vibrational Frequency Scale Factors for Density Functional Theory and the Polarization Consistent Basis Sets. *J. Comput. Chem.* **2012**, *33* (30), 2380–2387. <https://doi.org/10.1002/jcc.23073>.

-
- (84) Torio, M. E.; Busnengo, H. F. Site-Specific Product Selectivity of Stepped Pt Surfaces for Methane Dehydrogenation. *J. Phys. Chem. C* **2020**, *124* (36), 19649–19654. <https://doi.org/10.1021/acs.jpcc.0c05916>.
- (85) Watson, D. T. P.; Ge, Q.; King, D. A. Facile H–D Exchange in Adsorbed Methylidyne on Pt{110}–(1×2) and Deuteration to Gaseous Methane. *J. Chem. Phys.* **2001**, *115* (24), 11306–11316. <https://doi.org/10.1063/1.1410387>.
- (86) Quan, J.; Muttaqien, F.; Kondo, T.; Kozarashi, T.; Mogi, T.; Imabayashi, T.; Hamamoto, Y.; Inagaki, K.; Hamada, I.; Morikawa, Y.; Nakamura, J. Vibration-Driven Reaction of CO₂ on Cu Surfaces via Eley–Rideal-Type Mechanism. *Nat. Chem.* **2019**, *11* (8), 722–729. <https://doi.org/10.1038/s41557-019-0282-1>.

List of Figures

- Fig. 1.1: Schematic of the PES for the reaction between $A + BC$ to form $AB + C$, where r_{BC} and r_{AB} represent the interatomic distance between BC reactant and AB product, respectively. In the left plots, the transition state is closer to the entrance channel, in contrary to the plots on the right where the transition state is closer to the exit channel. The effect of adding either translational or vibrational energy can be observed from the red line. Reproduced with permission from ¹⁷15*
- Fig. 1.2: The reaction pathway of $CH(ads)$ species on the surface with co-adsorbed hydrogen atoms or $CO(ads)$ on a $Co(0001)$ surface. Reproduced with permission from ²⁶18*
- Fig. 2.1: 3D model from SolidWorks of the ultra-high vacuum set-up used in this thesis. Reproduced from Li Chen's dissertation ⁴⁰23*
- Fig. 2.2: A schematic diagram showing the path of the molecular beam (blue) and the position of the different surface probing apparatus in the machine. P1- refers to the first chamber where the supersonic expansion of the molecular beam takes place. P2- refers to the second chamber where the chopper and the separation valve reside. P3- refers to the third chamber, the smallest chamber in the machine which has a pyroelectric detector that can be translated in and out of the molecular beam path. P4- refers to the ultra-high vacuum chamber where the gas/surface reaction takes place. Diagram taken from Ana Gutiérrez-González's thesis ⁴²25*
- Fig. 2.3: Supersonic jet expansion in the nozzle. Reproduced with permission from ⁴³26*
- Fig. 2.4: 3D SolidWorks overview of the source and the cooling water flow direction in the copper tubes.....29*
- Fig. 2.5: Schematic diagram showing the paths that the molecular beam could travel in, either through the bypass or through the water 'bubbler'. Photograph showing a 'bubbler' made of glass placed in polystyrene cups during the freeze-pump-thaw cycle.30*
- Fig. 2.6: Seed ratio of D_2O in He as a function of liquid water temperature for He pressure of 1 bar. The D_2O vapour pressure values are taken from the work of Matsunaga et al. ⁴⁶31*
- Fig. 2.7: A $Cu(111)$ surface held in between two tungsten wires, used for surface heating and cooling.....32*

Fig. 2.8: Auger spectra showing measurements before and after cleaning the Cu(111) surface- top and Pt(211) surface- bottom. The bottom figure was reproduced from ⁴²	33
Fig. 2.9: Calibration of the QMS signal to the partial pressure of the H ₂ O in the UHV chamber.	35
Fig. 2.10: QMS signal measured for, A – The Cu(111) surface at T _s = 300 K without any liquid nitrogen cooling. At T _s = 180 K with the sample mount B- half-filled and C- fully filled with liquid nitrogen.	36
Fig. 2.11: Auger spectra showing the O and Cu peaks used for determining oxygen coverage on the surface.	38
Fig. 2.12: O:Cu peak ratio following Auger measurements performed at the same position on the surface, after the Cu(111) surface was exposed to 200 L of O ₂ at T _s = 300 K.....	40
Fig. 2.13: King and Wells trace at m/z 20 to measure the flux of D ₂ O impinging on a cold Cu(111) surface covered with a layer of ice, T _s = 90 K.	42
Fig. 2.14: The heating structure of the hydrogen atom beam source. Taken from the manual of HABS.....	43
Fig. 2.15: The gas/surface apparatus highlighting the path of the IR light travelling from the source and arriving on the surface at a grazing angle followed by its reflection into a detector.....	44
Fig. 2.16: (A)- The incident p-polarised electric field on the surface has a positive net electric field upon reflection meanwhile in (B)- incoming s-polarised electric field vector cancels out at the surface. (C)- A plot showing intensity of RAIRS signal with changing incident angle of the p- and s-polarised light. (D)- The different RAIRS peak intensity observed for the same molecule when it (i) lies flat or (ii) tilted on the surface. Reproduced with permission from ⁵⁷	45
Fig. 2.17: Image dipoles formed in the metal surface based on the different orientations of the surface adsorbates.....	46
Fig. 2.18: A schematic diagram of the Aculight Argos 2400 showing the idler (λ_i), pump (λ_p), and signal (λ_s) wavelengths.	47
Fig. 2.19: Doppler broadened profile resulting from laser excitation and the Lamb dip formed(inset) as a consequence of laser exciting the same set of molecules twice....	50
Fig. 2.20: Fluence curves measured for ν_3 , R-branch transitions - R ₀₀ (0), R ₀₂ (2) and R ₁₁ (1) for 2% D ₂ O in He mixture at T _n = 400 K (E _{kin} = 34 kJ/mol).	54

- Fig. 3.1: RAIR spectra showing absorption in the O-H stretch region corresponding to ice, OH on ice (3701 cm^{-1}) and OH from dissociated water molecules (3638 cm^{-1})58
- Fig. 3.2: TPD measurements performed with 2 K/s temperature ramp rate, shows ice desorption (black trace- peak desorption at $T_s = 177\text{ K}$) and recombinative desorption of water (red trace- highest desorption rate in the range $T_s = 200\text{-}320\text{ K}$) from a Cu(111) surface.....60
- Fig. 3.3: TPD traces of the stable and metastable species of D_2O (0.04 ML -blue and 2 ML - black) formed on a clean Cu(111) surface at $T_s = 135\text{ K}$. Temperature ramp rate used was 1 K/s61
- Fig. 3.4: Left- (i) RAIRS spectra for $\text{H}_2^{16}\text{O(g)}$ exposure (37 ML) on a clean Cu(111) surface at $T_s = 180\text{ K}$ with $E_{kin} = 0.28\text{ eV}$ (ii) $\text{H}_2^{16}\text{O(g)}$ dissociation on a $^{18}\text{O(ads)}$ covered Cu(111) surface resulting in a $^{16}\text{OH(ads)}$ RAIRS peak at 3637 cm^{-1} (iii) $\text{H}_2^{18}\text{O(g)}$ dissociation on a $^{16}\text{O(ads)}$ covered Cu(111) surface resulting in a $^{18}\text{OH(ads)}$ RAIRS peak at 3626 cm^{-1} . Right- The uptake for the experiment in the left with $^{16}\text{OH(ads)}$ peak after (a) 3.6 ML and (b) 7.2 ML of H_2^{16}O exposure on a surface with 0.07 ML of $^{18}\text{O(ads)}$63
- Fig. 3.5: Schematic diagram showing H transfer from the water molecule to the O atom on the surface forming two OH(ads) on the surface where one hydroxyl lies flat and other sits upright. Oxygen atom (red), copper atom(orange) and hydrogen atom(blue).64
- Fig. 3.6: Uptake of $^{18}\text{OH(ads)}$ following water collision on the Cu(111) surface covered with 0.04 ML of $^{16}\text{O(ads)}$. On the right, the first few RAIR spectra from the measurements on the left are shown following $\text{H}_2^{18}\text{O(g)}$ collision on the surface, (a) 0.01 ML , (b) 0.02 ML , (c) 0.03 ML and (d) 0.04 ML65
- Fig. 3.7: (i) RAIR spectrum measured after 2% H_2^{16}O in He deposition on a surface covered with 0.02 ML of $^{18}\text{O(ads)}$. Following surface annealing to (ii) 220 K , (iii) 250 K and (iv) 300 K , for 2 minutes at each temperature. Dashed red line at 3627 cm^{-1} refers to where the ^{18}OH stretch should be observed.66
- Fig. 3.8: $^{16}\text{OH(ads)}$ RAIRS peak at 3634 cm^{-1} following hydrogenation of $^{16}\text{O(ads)}$ with H atoms.67
- Fig. 3.9: RAIRS absorption signal peak height for $^{16}\text{OD(ads)}$ measured at 2689 cm^{-1} with increasing exposure of $\text{D}_2^{16}\text{O(g)}$ on the Cu(111) surface with varying pre-adsorbed $^{18}\text{O(ads)}$ coverage. The inset compares the initial $^{18}\text{O(ads)}$ coverage on the surface with $^{16}\text{OD(ads)}$ coverage following $\text{D}_2^{16}\text{O(g)}$ dissociation.69

- Fig. 3.10: Left - RAIR spectra measured with MCT detector following (a) 250 L and (b) 1588 L of H(atoms) exposure using HABS. Right - TPD traces showing desorption of H₂ from the Cu(111) surface when the surface was heated with a 2 K/s heating ramp. The surface was initially exposed to (a) 160 L, (b) 1588 L and (c) 1941 L of H atoms..... 72
- Fig. 3.11: The uptake of the ¹⁶OH(ads)- 3639 cm⁻¹ absorption signal measured after surface exposure to hydrogen atoms from HABS. The surface was initially dosed with 0.07 ML of ¹⁶O(ads) oxygen and then reacted to water molecules until the ¹⁸OH(ads)- 3627 cm⁻¹ RAIRS peak saturated. The H(atoms) dose was as following, (a) 0.2 L, (b) 0.4 L, (c) 0.4 L, (d) 0.4 L, (e) 0.8 L and (f) 17.6 L..... 74
- Fig. 3.12: Top panel- The ¹⁶OD coverage on the surface with increasing deposition of D₂¹⁶O on 0.07 ML ¹⁶O(ads) pre-dosed Cu(111) surface. Bottom panel- QMS trace for the m/z 20 where the blue arrows show the time when the flag was removed from the MB path while the black arrows show the time when the flag was placed in the MB path. Inset shows a QMS spike observed at around time=53 minutes when the flag blocked the MB from the surface. 76
- Figure 3.13: QMS trace for m/z 20 (H₂¹⁸O), m/z 17 (fragment of H₂¹⁶O) and m/z 2 (H₂) during the exposure of H atoms from the HABS. The labels (a-f) match with the RAIR spectra in Fig. 3.11..... 78
- Fig. 3.14: RAIR spectra showing the uptake of two OH(ads) peaks on a partially oxygen covered Cu(111) surface- 0.07 ML of ¹⁸O(ads). Both the spectra on the left and right are from the same experiment where the spectra were taken (a) after 0.07 ML ¹⁸O(ads) surface coverage, (b)-(f) following background water molecules exposure and (g)-(j) following H₂¹⁶O leak into UHV chamber. (b) 2·10⁻³ L, (c) 5·10⁻³ L, (d) 1·10⁻² L, (e) 1.5·10⁻² L, (f) 1.6·10⁻² L, (g) 0.13 L, (h) 0.28 L and (i) 0.92 L..... 79
- Fig. 3.15: QMS trace showing m/z 20 (blue) and m/z 22 (red) during the ¹⁸O covered surface exposure to a MB of D₂¹⁶O in He was leaked into the UHV chamber..... 81
- Fig. 4.1: Auger electron spectra measured from the Cu(111) surface. The green spectrum shows a clean Cu(111) surface after sputtering and annealing. The red spectrum was taken following surface exposure to 300 L of O₂ at T_s = 300 K. 86
- Fig. 4.2: O₂ deposition on a clean Cu(111) surface performed at two different surface temperatures followed by Auger signal measurements at 520 eV for O and 920 eV for Cu. 87

- Fig. 4.3: RAIRS uptake curve of the O-D stretch at 2689 cm^{-1} used for the calibration of RAIRS absorption to the OD(ads) coverage on the surface. Inset shows a RAIRS peak corresponding to the O-D stretch on a Cu(111) surface at $T_s = 180\text{ K}$ after D_2O deposition with $E_{kin} = 0.82\text{ eV}$88
- Fig. 4.5: OD uptake following D_2O dissociation with different E_{kin} on a clean Cu(111) surface at $T_s = 180\text{ K}$. Black – $E_{kin} = 0.86\text{ eV}$ and blue – $E_{kin} = 0.82\text{ eV}$90
- Fig. 4.6: Top- Uptake of OD(ads), measured with RAIRS, on the surface when 2% D_2O in He was incident on the surface at $T_s = 180\text{ K}$, with varying E_{kin} of incident D_2O molecules. Bottom- Sticking coefficients obtained from the OD uptake plotted as a function of translational energy of impinging water molecules in a logarithmic scale. The red line shows the S-shape curve fitting line for the sticking probabilities.93
- Fig. 4.7: Right- Symmetric and antisymmetric spin wavefunctions, Ψ_{spin} resulting from the combinations of the wavefunctions of the deuterium atoms while left- symmetry of rovibronic wavefunctions, Ψ_{rvib} . I refers to the total nuclear spin and m_I refers to the magnetic nuclear spin. Reproduced with permission from ⁷⁶.95
- Fig. 4.8: Fluence curves measured for three lowest rotational transitions of ortho D_2O molecules.97
- Fig. 4.9: Calculated fraction of ortho D_2O molecules as a function of rotational temperature for 3 lowest rotational energy levels, normalised to the maximum value.98
- Fig. 4.10: Top, left- OD(ads) coverage as a function of D_2O dose on Cu(111) at $T_s = 180\text{ K}$ with laser on and off. Top, right- OD(ads) coverage for laser-on with increasing D_2O dose at various E_{kin} . Bottom-State-resolved dissociation probability for dissociative adsorption of D_2O on Cu(111) at $T_s = 180\text{ K}$ as a function of translational energy. The red lines are the S-curve fittings.101
- Fig. 4.11: Sticking probabilities predicted for different initial vibrational states of H_2O on Cu(111)- (v_1, v_2, v_3). The top figure is without Boltzmann weighting whereas the bottom figure includes Boltzmann weighting.103
- Fig. 5.1: RAIRS spectra from Trenary et al. showing formation of methylidyne (CH) from carbon atoms hydrogenation on a Pt(111) surface initially dosed with carbon atoms using ethylene (C_2H_4). The CH(ads) RAIRS peak shifted continuously from 2974 cm^{-1} to 2956 cm^{-1} with increasing surface temperature from $T_s = 200\text{ K}$ to $T_s = 500\text{ K}$. Reproduced with permission ⁸⁰.106

- Fig. 5.2: RAIR spectra showing methyl formation on the steps and terraces of a Pt(211) surface recorded during surface exposure to a molecular beam of 3% CH₄ in He at T_s = 120 K with E_{kin} = 65 kJ/mol of incident energy. Reproduced from ⁴².....107
- Fig. 5.3: (a) RAIR spectrum following dissociation of CH₄ molecules on a Pt(211) surface at T_s = 150 K with E_{kin} = 65 kJ/mol of incident energy. (b) After annealing the surface at T_s = 230 K for 2 minutes and then cooling to T_s = 150 K prior to RAIRS measurement. Similar procedure was used for (c) to (f) but at different annealing T_s - (c) T_s = 250 K, (d) T_s = 310 K, (e) T_s = 330 K and (f) T_s = 350 K. When all the H atoms on the surface were removed after heating the surface to T_s = 350 K, the surface was exposed to (g) 0.5 L, (h) 1.0 L, (i) 1.8 L, (j) 2.3 L of D₂ at T_s = 150 K. (k) Annealing surface once again to T_s = 350 K and (l) 0.5 L of D₂ deposition at T_s = 150 K.....109
- Fig. 5.4: TPD traces of D₂ desorption from the Pt(211). The surface was exposed to varying doses of D₂ followed by surface heating from T_s = 150 K to T_s = 400 K with a 2 K/s heating ramp which caused desorption of deuterium molecules from the steps and terraces of Pt(211).110
- Fig. 5.5: A schematic showing the side view of a Pt(211) surface where the three adsorption sites are visible. Reproduced with permission from ⁸¹.....111
- Fig. 5.6: RAIR spectra showing the dehydrogenation of CD₃(ads) on steps - 2133 cm⁻¹ and terraces - 2098 cm⁻¹ into CD(ads) and the three discrete CH(ads) peaks shifting with increasing surface temperature. (a) After exposure of 2% CD₄ in He at T_s = 150 K and E_{kin} = 72 kJ/mol, there was CH₃ on the steps and terraces of the Pt(211) surface. (b) Surface was briefly annealed to T_s = 230 K for 2 minutes and cooled down to T_s = 150 K before recording RAIRS. This step was repeated but the surface was heated to different surface temperatures - (c) 250 K, (d) 310 K, (e) 330 K and (f) 350 K.....112
- Fig. 5.7: RAIRS spectra showing the uptake of CH(ads) with time, where time increases from bottom to top. Every RAIRS spectrum was taken following an additional of 0.4 L of methane exposure at T_s = 380 K with E_{kin} = 65 kJ/mol incident energy - (a) 0.4 L, (b) 0.8 L, (c) 1.2 L, (d) 1.6 L, (e) 2.0 L, (f) 2.4 L, (g) 2.8 L and (h) 3.2 L.113
- Fig. 5.8: Schematic diagram showing the adsorption of CH(ads) on the sst sites and H(ads) on the ss sites of a Pt(211) surface. Reproduced with permission from ⁸¹.114
- Fig. 5.9: RAIR spectra showing C-H stretch and C-D stretch regions during exposure to D₂ on a Pt(211) surface covered with CH(ads). (a) A RAIR spectrum taken after 3% CH₄ in He

with $E_{kin} = 64$ kJ/mol deposition on a Pt(211) surface at $T_s = 300$ K. (b) After heating surface to $T_s = 350$ K which removed surface hydrogen atoms. Then the surface was exposed to varying doses of D_2 – (c) 0.5 L, (d) 1.0 L, (e) 1.8 L and (f) 2.3 L at $T_s = 150$ K. (g) Surface was again annealed at $T_s = 350$ K and (h) exposed to 0.5 L of D_2 at $T_s = 150$ K.116

Fig. 5.10: Left panel- (a) RAIR spectrum of methane deposition with $E_{kin} = 41$ kJ/mol at $T_s = 120$ K resulting in the formation of methyl on steps of Pt(211) observed at 2904 cm^{-1} followed by surface heating to (b) $T_s = 250$ K, (c) 300 K and (d) 350 K. Right panel- (a) RAIRS spectrum after dissociating CH_4 with the 65 kJ/mol incident energy on a Pt(211) at $T_s = 120$ K – the step sites of the Pt(211) surface was previously passivated with deuterium atoms. After heating the surface to (b) $T_s = 250$ K, (c) $T_s = 300$ K and (d) $T_s = 350$ K.117

Fig. 5.11: RAIR spectra recorded during deposition of methane molecules on the Pt(211) with translational energy of 41 kJ/mol – left panel and 64 kJ/mol- right panel. Each spectrum was recorded following different methane molecules exposure – (a) 0 L, (b) 0.5 L, (c) 1.5 L, (d) 2.5 L, (e) 3.5 L, (f) 4.5 L, (g) 5.5 L, (h) 6.5 L and (i) 9.5 L.....120

Fig. 6.1: (a) RAIR spectra showing the reduction of OD(ads) peak intensity and the appearance of a novel peak at 3637 cm^{-1} . (b) The coverage of OD and OH on the surface during surface exposure to a MB of 2% D_2O in He with $E_{kin} = 1.1$ eV and the evolution of these species after the MB was stopped. (c) Total coverage of the adsorbates (OH + OD) plotted from (b).....124

Fig. 6.2: On the left, the IR spectra for O-H stretches are presented and on the right, RAIR spectra for O-D stretches are shown. Both set of IR spectra demonstrate the uptake for surface hydroxyls when a surface with 0.07 ML of $^{18}O(ads)$ was exposed to $H_2^{16}O(g)$ from the UHV background (black spectra) followed by surface exposure to $D_2^{16}O(g)$ (purple spectra). The amount of water exposure for the different spectra are as following, (a) 0.09 L, (b) 0.11 L and (c) 0.46 L.....125

Fig.6.3: Top- Reactivity of vibrationally excited water molecules (ν_1, ν_2, ν_3) on a Cu(111) where the black curve represents the molecules in the ground state. Bottom- Same as the top graph but dissociation probability is in the logarithmic scale. Reproduced from ³⁵..127

Fig. 6.4: The probability of dissociative chemisorption of HOD molecules in various low-lying vibrational states. The reaction can occur through two channels, top- $\text{HOD} \rightarrow \text{OH} + \text{D}$ and bottom- $\text{HOD} \rightarrow \text{OD} + \text{H}$. Reproduced from ³⁶.128

List of Tables

<i>Table 1: Average speed and translational energy of the D₂O molecules and CH₄ molecules in the gas mixtures specified, as function of nozzle temperatures.....</i>	<i>28</i>
<i>Table 2: The fraction of D₂O molecules in different vibrational states for various T_n calculated using the formulae 2.8 and 2.9 above.</i>	<i>52</i>
<i>Table 3: RAIRS frequencies corresponding to the OH(ads) isotopologues.</i>	<i>63</i>
<i>Table 4 : Calibrating Auger signal to O coverage on the surface.</i>	<i>86</i>
<i>Table 5: Vibrational population of D₂O molecules at the nozzle temperatures used for laser-off experiments.</i>	<i>92</i>
<i>Table 6: The five lowest rotational level transitions for D₂O molecules.</i>	<i>96</i>
<i>Table 7: The excited fraction of D₂O molecules for J KaKc = 111 at different nozzle temperatures.</i>	<i>99</i>
<i>Table 8: Summary of the information obtained from the S-curve fittings in Fig.4.10.....</i>	<i>102</i>
<i>Table 9: Assignment of RAIRS peaks observed in Fig. 5.3.....</i>	<i>109</i>

Curriculum Vitae

Harmina Vejayan

Avenue Victor Ruffy 4, 1012 Lausanne

harminavejayan@gmail.com

Nationality: Malaysian



Education

2018-2022

Ph.D. in Physical Chemistry

École Polytechnique Fédérale de Lausanne, Switzerland

Supervisor: Prof Rainer Beck

Thesis title: Gas/Surface reactions probed by reflection
absorption infrared spectroscopy

2013-2018

Integrated Masters, MChem(Hons) Materials Chemistry

University of St Andrews, Scotland

2016-2017

Industrial Placement

SINTEF at Trondheim, Norway

Other experiences

2022

Finalist of 'My thesis in 180 seconds' competition

Title of presentation - *Water splitting on Copper*

2018-2021

Teaching assistant for Quantum Chemistry and Spectroscopy

École Polytechnique Fédérale de Lausanne, Switzerland

Publications

1) Zhou, X.; Vejayan, H.; Beck, R.D.; Hua Guo, Jiang, B. Infrared Activities of Adsorbed Species on Metal Surfaces: The Puzzle of Adsorbed Methyl (CH_3) *J. Phys. Chem. Lett.* **2021** 12 (45), 11164-11169, DOI: 10.1021/acs.jpcllett.1c03342.

2) Sung, Y.; Vejayan, H.; Baddeley, C.J.; Richardson, N.V.; Grillo, F.; Schaub, R. Surface Confined Hydrogenation of Graphene Nanoribbons. *ACS Nano* **2022** 16 (7), 10281-10291, DOI: 10.1021/acsnano.1c11372.

3) Vejayan, H.; Gutiérrez-González, A.; Torio, M.E.; Busnengo, H.F.; Beck, R.D.; Methylidyne adsorption on Pt(211) probed by Reflection Absorption Infrared Spectroscopy (RAIRS) *J. Phys. Chem.* **2022** 126 (49), 20886-20891, DOI: 10.1021/acs.jpcc.2c07235.